






Craters of habit: Patterns of deformation in the western Galápagos

 Eoin Reddin^{*α},  Susanna K. Ebmeier^{†α},  Marco Bagnardi^β,  Andrew F. Bell^γ, and  Pedro Espín Bedón^α

^α School of Earth and Environment, University of Leeds, Leeds, UK, LS29JT.

^β U.S. Geological Survey, Volcano Science Center, Vancouver, WA, USA.

^γ School of GeoSciences, University of Edinburgh, James Hutton Road, Edinburgh EH9 3FE, UK.

ABSTRACT

The western Galápagos islands of Fernandina and Isabela comprise six active volcanoes that have deformed since first observed by satellite radar in the early 1990s. We analyse new (2015–2022) displacement time series at Alcedo, Cerro Azul, Darwin, Fernandina, Sierra Negra, and Wolf volcanoes in the context of deformation and unrest since 1992. Previous discussions of volcano deformation have focused on eruptions, major intrusive episodes, and the structure of sub-volcanic systems. We discuss the full geodetic record of deformation and show that the style of eruptions, characteristics of unrest and deformation are distinctive at each volcano. These characteristic differences in deformation and unrest styles between the volcanoes have persisted for at least three decades, since the first satellite radar measurements. These consistent differences in shallow magma storage and eruptive dynamics reflect the influence of “top-down” factors and evolutionary stage, providing a basis to understand volcanic unrest here, and to inform monitoring strategies.

NON-TECHNICAL SUMMARY

The western Galápagos are home to six active volcanoes, and is one of the most volcanically active locations on the planet. The high levels of activity, and close proximity to one another make them a prime target to study a multitude of volcanic processes using remotely sensed data. We monitor ground deformation at each of these volcanoes (Alcedo, Cerro Azul, Darwin, Fernandina, Sierra Negra, and Wolf) using satellite radar data from 2015–2022, and make new observations of unrest at each. We contextualise these observations using the complete geodetic record (extending back to 1990), as well as with various seismic, geophysical, and petrological studies. We find characteristic differences in behaviour, that have persisted for at least three decades, and probably longer. Based on these observations, we describe magma storage conditions at each volcano, and suggest a classification basis to inform monitoring strategies.

KEYWORDS: Galápagos; Fernandina; Wolf; InSAR; Ground Deformation; Sub-volcanic structure.

1 INTRODUCTION

Both the levels of activity and the magnitude of volcanic deformation in the western Galápagos are exceptional. From 1917–2023, Fernandina has averaged an eruption every five years [Vasconez et al. 2018], while Sierra Negra experiences metre-scale deformation [Geist et al. 2008; Bell et al. 2021b], and erupts every 11–12 years [Vasconez et al. 2018]. Of the seven major volcanoes, six have experienced significant unrest since the 1990s: Alcedo, Cerro Azul, Darwin, Fernandina, Sierra Negra, and Wolf [e.g. Amelung et al. 2000; Baker 2012; Vasconez et al. 2018; Bell et al. 2021b], while Ecuador volcano has no documented eruptions since 1150 CE [Venzke 2023]. The inaccessibility of the western Galápagos means that much of our knowledge of the volcanoes comes from satellite radar measurement of displacements.

A fundamental control on Galápagos volcanism is the proximity to the centre of the upwelling plume, as implicated by differences in eruption rate (e.g. Fernandina [Kurz et al. 2014]) and the thermal state of magmatic reservoirs [Harpp and Geist 2018]. Correlations in deformation between volcanoes during unrest and eruption are indicative of deep connectivity, for example through pore-pressure diffusion [Reddin et al. 2023],

while some eruptions have been attributed to deep-sourced “flushing” events, where primitive basalts ascend from depth during eruptions [Stock et al. 2020]. Major trends in magma flux and the clustering of eruptions in the Galápagos are thus attributable to variable melt supplies from the mantle plume.

However, such “bottom-up” processes are not sufficient to account for the differences in characteristic eruption and unrest between the six western Galápagos volcanoes. Here, “bottom-up” refers to processes in the volcanic sub-surface, such as changes in magma supply, migration, and storage, while “top-down” refers to near-surface, topographically modulated processes, such as trapdoor and ring faults, and their corresponding impact on deformation patterns. Past geodetic measurements [Bagnardi and Amelung 2012] and petrological studies suggest some notable differences in magma storage between volcanoes [Harpp and Geist 2018].

The various characteristic deformation trends include sustained periods of uplift on the order of both metres (Fernandina, Sierra Negra) and centimetres (Wolf), interrupted by major eruptions. At Sierra Negra, the intra-caldera fault is located in the southwestern portion of the caldera, and facilitates “trapdoor faulting,” where the caldera floor hinges upwards like a trapdoor during inter-eruptive inflation [Amelung et al. 2000; Jónsson et al. 2005]. Eruptions here in 2005 and 2018 were accompanied by slip along this fault [Jónsson 2009;

*✉ E.P.Reddin@leeds.ac.uk

†✉ S.K.Ebmeier@leeds.ac.uk

Bell et al. 2021b], while it also acts as a conduit for magmatic fluids to the shallow surface fumarole field [Aiuppa et al. 2022]. Similar magmatic–tectonic interactions at Alcedo modify displacement patterns during periods of uplift [Galletto et al. 2019]. Displacements at Fernandina are associated with frequent eruptions and intrusions (e.g. 2006 and 2007 [Bagnardi and Amelung 2012]). Intrusions or eruptions occur at Cerro Azul about once a decade on its southeastern flank, while Darwin and Alcedo show lower magnitude subsidence between short-lived episodes of uplift.

Here, we consider three decades of volcano deformation measurements made at the western Galápagos volcanoes with satellite radar, and discuss the implications of persistent displacement styles on our understanding of magmatic processes. We first review trends in unrest and eruptions over the period for which geodetic data are available (1992–2022). For each volcano, we then describe previous interpretations of deformation as detected by Interferometric Synthetic Aperture Radar (InSAR) and ground-based surveys, followed by the implications of new displacement time series constructed from Sentinel-1 imagery, spanning 2015–2022. Finally, we provide an updated picture of sub-volcanic magmatic zones from geodetic observations and modelling for each volcano, and discuss the relationships between shallow magmatic systems, topography and petrological classifications of Galápagos volcanism.

1.1 Background of the western Galápagos

The Galápagos islands straddle the equator in the east Pacific (Figure 1). There are 13 major islands here, the westernmost of which (Isabela and Fernandina) are the most volcanically active (Figure 1). They are located approximately 250 km south of the Galápagos Spreading Centre [Harpp and Geist 2018], which is east–west striking, and offset by the Galápagos transform fault. The islands lie on the Nazca plate, and have formed as they move eastwards over the Galápagos mantle plume. Despite the near-constant volcanism on the islands, monitoring instrumentation is sparse. Instituto Geofísico de la Escuela Politécnica Nacional (IGEPN) maintain six permanent seismic stations, two on Sierra Negra, one on Cerro Azul, one to the southeast of Alcedo, and two on Fernandina Island (Figure 1). There are permanent GPS stations on Sierra Negra (Figure 1), while campaign GPS and gravity surveys have been carried out at Fernandina and Sierra Negra in the early 2000s [Geist et al. 2006a]. These ground-based systems have prioritised monitoring Fernandina and Sierra Negra volcanoes (Figure 1), the former of which is the most frequently erupting Galápagos volcano, while the latter is the most actively deforming and most voluminous [Naumann and Geist 2000]. By comparison, Wolf, which erupted in 2015 and 2022, has no permanent monitoring stations (Figure 1). The nearest station to detect elevated seismicity during the 2022 Wolf eruption was FER1, on Fernandina island (Figure 1) [IGEPN 2022a]. The sparse coverage of monitoring stations means that pre-eruptive unrest may be challenging to identify (e.g. Wolf, 2022), and limits the potential of studying volcanic behaviour during periods of effusive quiescence (e.g. Darwin, 2020) from ground-based measurements. InSAR measurements, which

require no ground-based equipment, have transformed our knowledge of magma storage and movement in the Galápagos.

1.2 Satellite radar measurements

InSAR is a geodetic technique that measures changes in line-of-sight (LOS) displacement from the instrument (usually a satellite) to the Earth’s surface. It allows for the measurement of these changes on centimetre to millimetre scales, with a spatial resolution on the order of several metres. It observes across areas of tens to hundreds of kilometres, and can take measurements with repeat times of days to weeks. It is a powerful tool in Earth system science for the study of the earthquake cycle (e.g. pre-, syn- and post-earthquake), and processes that drive volcanic deformation (e.g. mass movement, hydrothermal activity, magma migration, and eruption). It is particularly useful in the western Galápagos due to the number of volcanoes across a relatively small area, and good year-round coherence (a measure of correlation, the change in radar backscatter characteristics between acquisitions) from bare rock. Despite the generally good year-round coherence in the Galápagos, newly erupted products, and forested areas such as the southern flank of Sierra Negra, are generally incoherent. InSAR is best used to measure cumulative change between acquisition dates rather than continuously, as the satellite return period (e.g. 6–12 days for Sentinel-1) is far too infrequent to monitor changes occurring during an eruption that are better captured by continuous monitoring techniques. Satellite-based InSAR missions have been used to measure displacement at western Galápagos volcanoes since 1992 (Figure 4), with multiple platforms used: Amelung et al. [2000] used ERS-1 and ERS-2 to study Isabela and Fernandina from 1992–1998, while Hooper et al. [2007] used the platforms to study Alcedo from 1992–2001. Baker [2012] used the ERS missions, as well as Radarsat-1, Envisat, and ALOS-1 missions to study Galápagos volcanoes from 1992–2011. The 1995 eruption of Fernandina was studied by Bagnardi et al. [2013] using JERS-1, and by Jónsson et al. [1999] using ERS. Pepe et al. [2017] studied 2012–2013 unrest at Fernandina using COSMO-SkyMed, while Galletto et al. [2023] studied the 2017 and 2018 eruptions of Fernandina using COSMO-SkyMed and Sentinel-1. Xu et al. [2016] used Sentinel-1A and ALOS-2 to study the 2015 eruption of Wolf, while Shreve and Delgado [2023] used Sentinel-1, ALOS-2, and COSMO-SkyMed to study the 2018 eruption of Sierra Negra.

1.3 Characteristics of Western Galápagos volcanic activity.

Despite diverse styles of eruption and unrest, there are some common features in western Galápagos volcanism, like the influence of topographic loading on magma ascent, stacked magmatic reservoirs, very active caldera faulting, and periodic increases in magma flux into the shallow crust (“resurgence” at quiescent systems or “flushing” during eruptions). These volcanoes all share a unique “overtaken-soup-plate” morphology [Naumann and Geist 2000].

The lack of high-magnitude regional stress fields associated with rifting or arc settings mean that the impact of local processes, such as topography, unloading from caldera col-

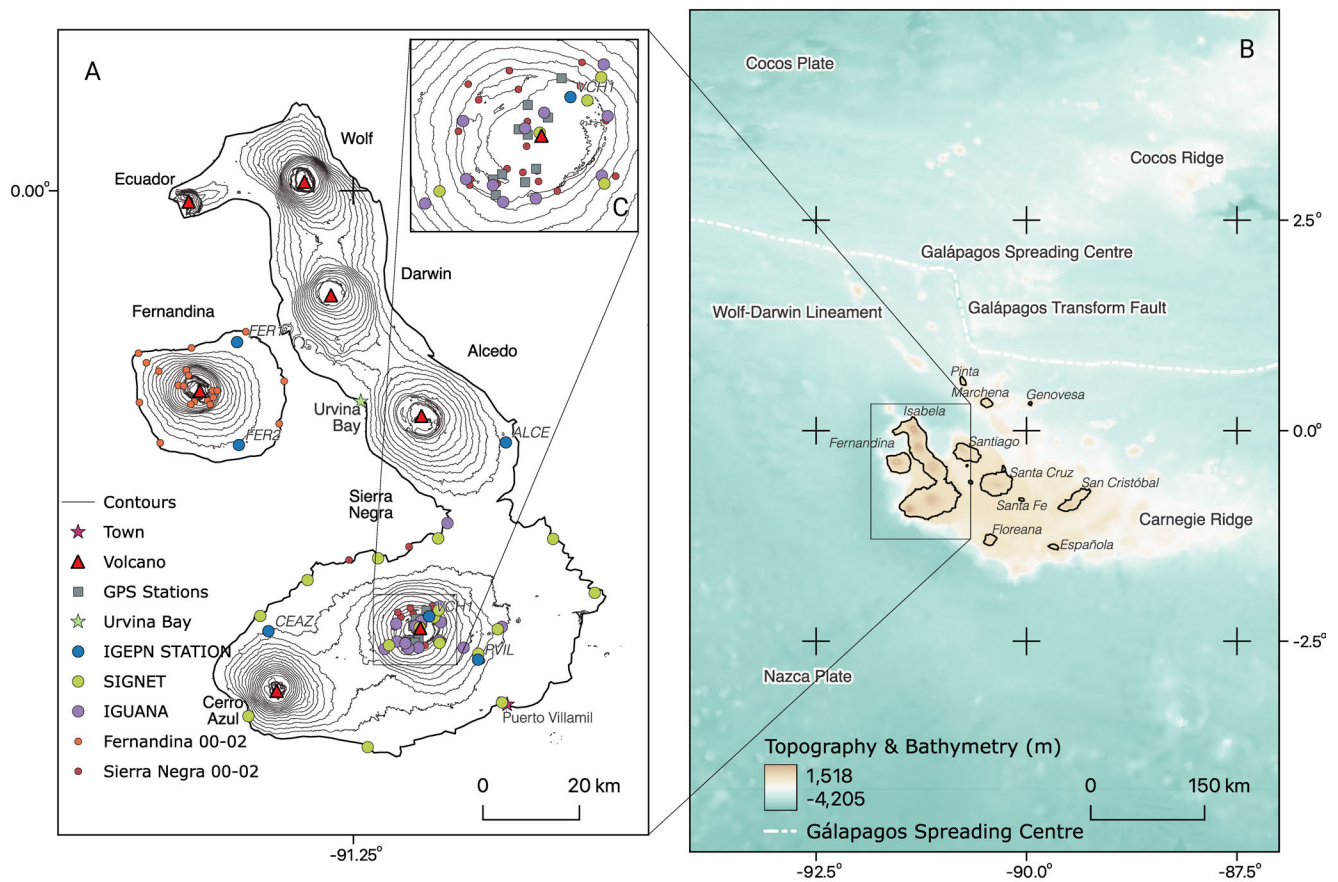


Figure 1: Regional view of the Galápagos. [A] The western Galápagos islands of Isabela and Fernandina, showing the volcanoes considered in this study (red triangles). The geographic locations of both continuous and campaign ground-based monitoring that are discussed here are annotated, as is the population centre of Puerto Villamil and Urvina Bay—the location of a major unrest episode in 1954. [B] A broader view of the regional tectonic setting. Sub-aerial islands are labelled, as are major tectonic plates and faults [e.g. Harpp and Geist 2018]. The colorscale indicates bathymetric and topographic elevation, as discussed in Section 3.3. [C] Distribution of geophysical monitoring equipment within the caldera at Sierra Negra.

lapse, and the effect of recent intrusions, are clearer than in other volcanic settings. Eruptions since 1992 (with the exception of the phreatic explosion of Alcedo in 1993 [Green 1994]) have been fissure eruptions, either radial or circumferential (Figure 2). The stress field exerted by the volcanic edifice and previous eruptions exerts a primary control on where fissures develop, and their geometry during eruptions [Chadwick and Dieterich 1995; Bagnardi et al. 2013; Chestler and Grosfils 2013; Corbi et al. 2015; Davis et al. 2021]. Fernandina alternates between radial and circumferential fissures, while all of the recent unrest at Cerro Azul has occurred on the southeastern flank. Similarly, each confirmed eruption at Wolf since 1948 has occurred on the southeastern flank, alternating from circumferential, to radial. This top-down topographic control on eruptive behaviour is also evident at Sierra Negra; a combination of buoyant and topographic forces caused a lateral intrusion there to bend during the 2018 eruption [Davis et al. 2021]. At three volcanoes, there is geodetic and petrological evidence for vertically “stacked” reservoirs (Fernandina, Wolf, and Sierra Negra (Figure 5)). The deeper of these reservoirs acts as a source for shallow and lateral intrusions at Fernandina (at approximately 5 km depth) [Bagnardi and Amelung

2012], Sierra Negra (at approximately 7.5 km depth) [Davidge et al. 2017], while a reservoir at 6 km depth acted as a source for the 2017 off-caldera unrest at Cerro Azul [Guo et al. 2019] (Figure 5).

Displacements and eruptions at Sierra Negra and Alcedo are controlled by the interaction of top-down and bottom-up processes: a magmatic source and an intra-caldera fault. At Alcedo, this fault exerted a structural control on asymmetric displacement patterns during the volcano’s resurgence [Bagnardi 2014; Galetto et al. 2019]. Similarly, slip along the intra-caldera trapdoor fault at Sierra Negra preceded both the 2005 and 2018 eruptions [Yun et al. 2006; Geist et al. 2008; Jónsson 2009; Bell et al. 2021b].

Magma periodically fluxes into the shallow reservoir at quiescent volcanoes. Galetto et al. [2019] describe this as a resurgence at Alcedo volcano. Though this flux manifests as non-eruptive unrest at Alcedo (and Darwin: Section 4.2), similar changes in magma supply (flushing) are the driving force behind eruptions at Fernandina and Wolf [Stock et al. 2020]. Additionally, there is evidence that this magma flux from the Galápagos plume is irregular with time [Reddin et al. 2023].

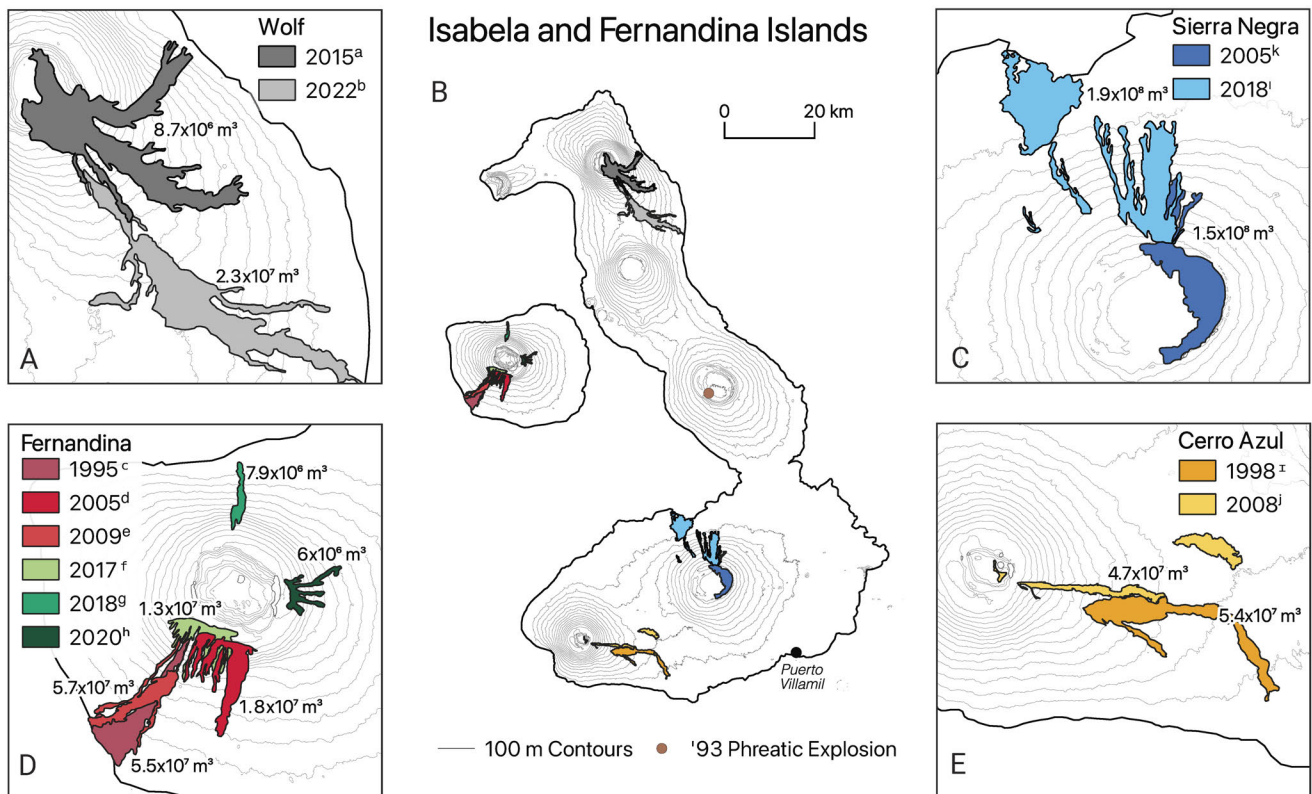


Figure 2: Extent of erupted lavas in the western Galápagos since 1992. This eruption record is representative of the 300 year historical record. [A] Extents and volumes of lavas from the 2015, and 2022 eruptions of Wolf. [B] Overview of island-wide extent of lavas erupted during the InSAR era. [C] Extents and volumes of lavas from the 2005, and 2018 eruptions of Sierra Negra. [D] Extents and volumes of lavas from the 1995, 2005, 2009, 2017, 2018, and 2020 eruptions of Fernandina. [E] Extents and volumes of lavas from the 1998, and 2008 eruptions of Cerro Azul. Darwin and Alcedo did not effusively erupt over this period. However, the location of a 1993 phreatic explosion at Alcedo is included [Green 1994]. In each case, the estimated erupted volume is included if known, as presented in Table A23, and annotated beside the relevant lava flow.

2 PREVIOUS UNREST AND DEFORMATION IN THE WESTERN GALÁPAGOS

Here, we discuss the unrest history and deformation observations at each of Wolf, Darwin, Fernandina, Alcedo, Sierra Negra, and Cerro Azul. We focus on unrest in the InSAR era, since the early 1990s, though we may make reference to earlier eruptions. We include deformation studies here that have used various satellite missions, such as ERS, ENVISAT, and Sentinel-1, and later present our own observations from Sentinel-1 data.

2.1 Wolf

Wolf (1710 m) is the northernmost western Galápagos volcano. It is also the most remote, with no ground-based monitoring instrumentation [Bernard 2022]. Wolf's remote location means that eruptions here are not a threat to human life. However, it is home to the critically endangered pink iguana (*Conolophus marthae*), and the response following both the 2015 and 2022 eruptions aimed to ensure that these iguanas were not threatened [Bernard 2022].

2.1.1 Eruptive history

Wolf was quiescent for much of the late 20th and early 21st centuries (from 1982–2015 [Venzke 2023]). However, it has recently erupted twice in quick succession, in 2015 and 2022 [Stock et al. 2018; Venzke 2023]. The 2015 eruption (25/05/2015–26/07/2015) was initially explosive, with a 15 km ash column, and lava fountaining—the fountaining was sufficiently vigorous to produce reticulite scoria [Bernard et al. 2019; Bernard 2022]. Following this the eruption transitioned to a phase of intra-caldera lava effusion [Bernard et al. 2019; Bernard 2022] (Figure 2). Throughout the eruption, the FER1 station detected 465 earthquakes at Wolf [Bernard et al. 2019].

In comparison, the 2022 eruption was much less explosive during its initiation phase (column was approximately 5.5 km high) [Bernard 2022], though was sustained for a much longer duration. The eruption started on January 6th, and IGEPN did not report an end to the eruption until May 5th, a period of 119 days [IGEPN 2022a]. The eruption intensity peaked during its first five days, with seismic swarms, tremor, and earthquakes (detected at FER1), gas and ash plumes (up to 3.8 km), and thermal activity from lava flows [IGEPN 2022a]. By January 11th there were three radial fissures on the south-eastern flank, with lava covering an area of 7.4 km² [IGEPN

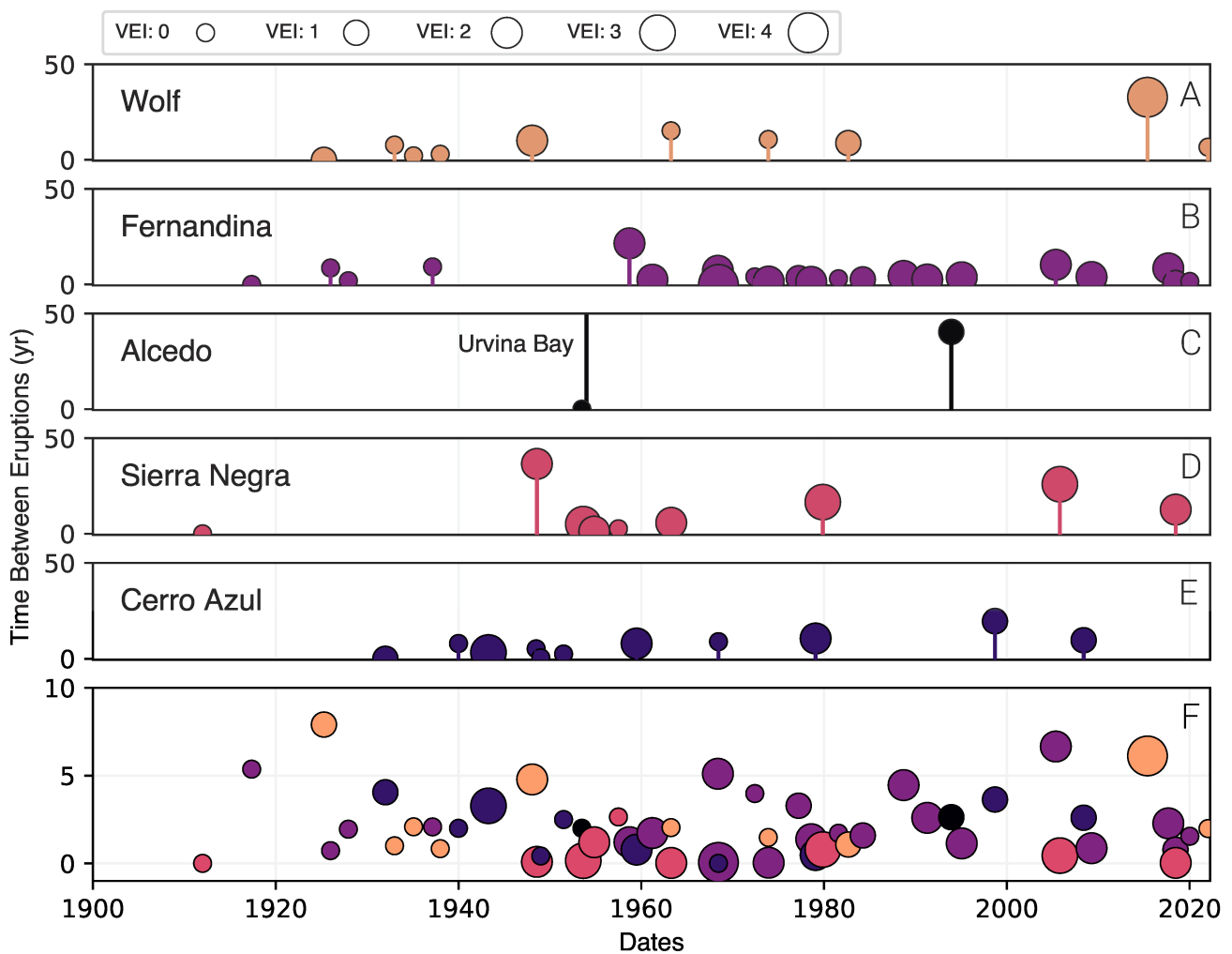


Figure 3: Eruptions at the western Galápagos since the turn of the 20th century. For each volcano, the eruption data are on the x-axis, while the time between the preceding eruption is plotting on the y-axis. The marker size refers to the Volcanic Explosivity index of the given eruptions (as given in the Global Volcanism Program database [Venzke 2023]), while colour delineates between volcanoes. [A]–[E] Eruption date, time between preceding eruption, and VEI for each of Wolf, Fernandina, Alcedo, Sierra Negra, and Cerro Azul. Darwin has not been included as it has not erupted since the early 19th century, while [C] includes the 1954 uplift at Urvina Bay (Section 5.2.3). [F] Eruptions at all volcanoes, with the time between eruptions referring to all eruptions at any western Galápagos volcano. Known non-eruptive unrest (e.g. Urvina Bay 1954, or Cerro Azul, 2017) are not included.

2022b]. By May 5th, at least five fissures had opened, and lava flows covered an area of 30 km², with a maximum distance of 18.5 km, almost reaching the sea to the southeast of the volcano [IGEPN 2022c]. In total, 60,000 tonnes of SO₂ were emitted, though none had been recorded in the 30 days prior to the eruption end [IGEPN 2022c]. There were no intra-caldera lava flows, dissimilar from the 2015, and 1982 eruptions, when the thickest lava flows were located within the caldera (9.5–9.7 m) [Bernard et al. 2019]. These are the first eruptions at Wolf since 1982 [Geist et al. 2005] but suggest that Wolf follows the same alternating eruptive fissure pattern as Fernandina (radial-circumferential-radial for the 1982, 2015, and 2022 eruptions respectively [Bernard et al. 2019; IGEPN 2022a]), indicating that, like Fernandina, stress changes during one eruption may affect the geometry of the succeeding eruption [Bagnardi et al. 2013]. At Wolf, like Cerro Azul, the

most recent eruptions have all taken place on the southeastern flank, though often with an intra-caldera component (as have all confirmed eruptions since 1948 [Siebert et al. 2010]).

2.1.2 Previous observations of displacement at Wolf

Wolf has perhaps the best example of variable magma supply rates to volcanoes from the Galápagos plume. Like Fernandina, there is geodetic evidence of stacked magma reservoirs at 1 km depth, and > 5 km [Xu et al. 2016; Stock et al. 2018], though there is evidence of even deeper reservoirs—clinopyroxenes erupted during the 2015 eruption equilibrated at 9.9±2.2 km, while glomerocrysts and phenocrysts equilibrated at 11.2±2.8 km [Stock et al. 2018]. However, Liu et al. [2019] and Xu et al. [2023] suggested that instead of vertically distributed reservoirs, deformation may be explained by an interplay between the caldera ring fault, and a single

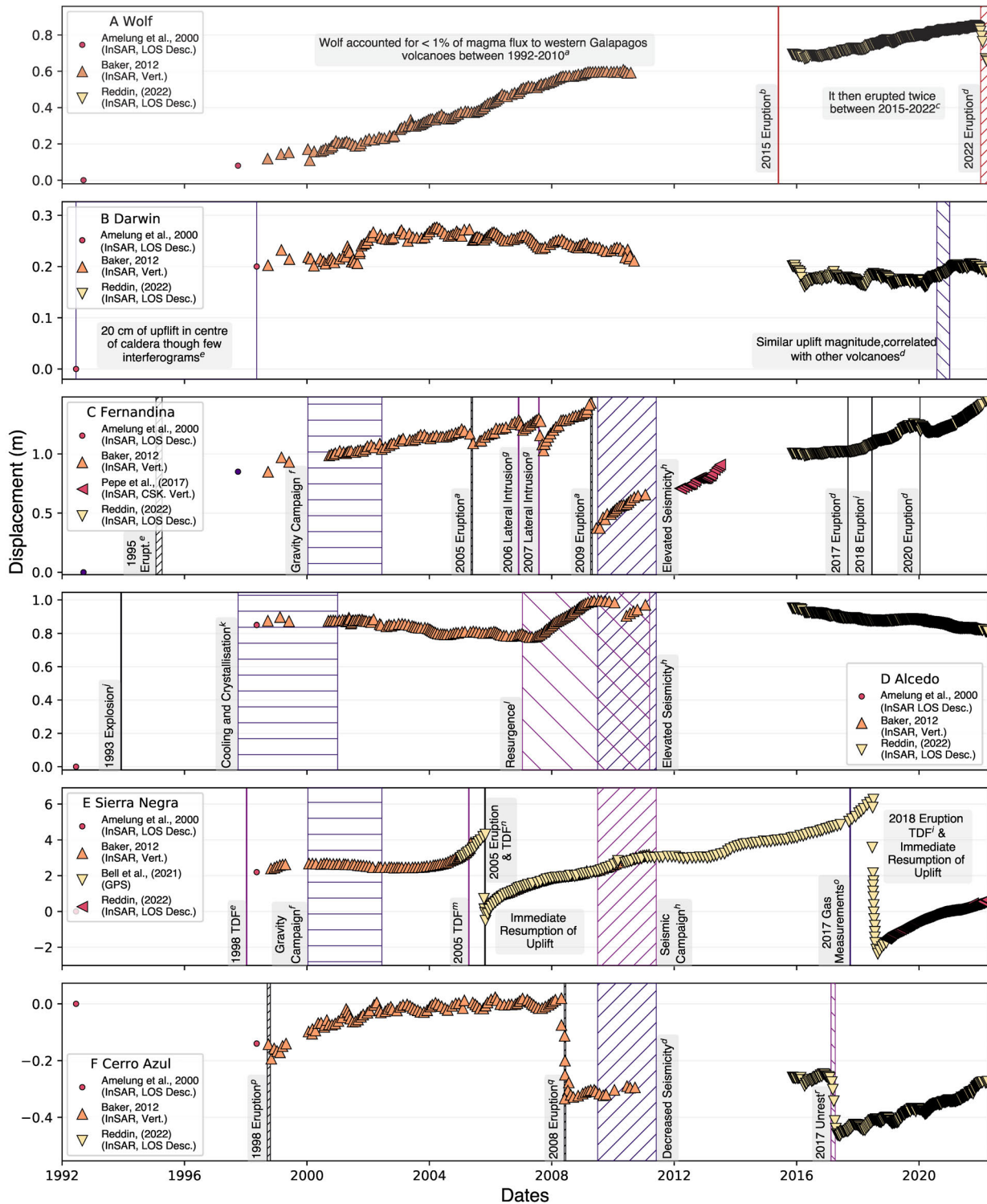


Figure 4: Summary of ground surface displacement at each Galápagos volcano, over 30 years from 1992–2022. Displacement in centimetres is given on the y-axis (either vertical or Line-of-Sight (LOS)), while time is given on the x-axis. Marker colour denotes the study that the displacement data are taken from, while vertical bars illustrate periods where the volcano was the subject of an unrest-focused study. The nature of the unrest, and the appropriate study is labelled beside each vertical bar. [A] Deformation at Wolf, ^aBagnardi [2014], ^bStock et al. [2018], ^cIGEPN, ^dThis Study. [B] Deformation at Darwin, ^eAmelung et al. [2000]. [C] Deformation at Fernandina, ^fGeist et al. [2006a], ^gBagnardi and Amelung [2012], ^hDavidge et al. [2017] ⁱVasconez et al. [2018]. [D] Deformation at Alcedo, ^jGreen [1994], ^kHooper et al. [2007], ^lGaletto et al. [2019], ^dDavidge et al. [2017]. [E] Deformation at Sierra Negra, ^mChadwick et al. [2006], ⁿGeist et al. [2008], ^oAiuppa et al. [2022]. [F] Deformation at Cerro Azul, ^pBaker [2012], ^qGaletto et al. [2020], ^rBagnardi [2017].

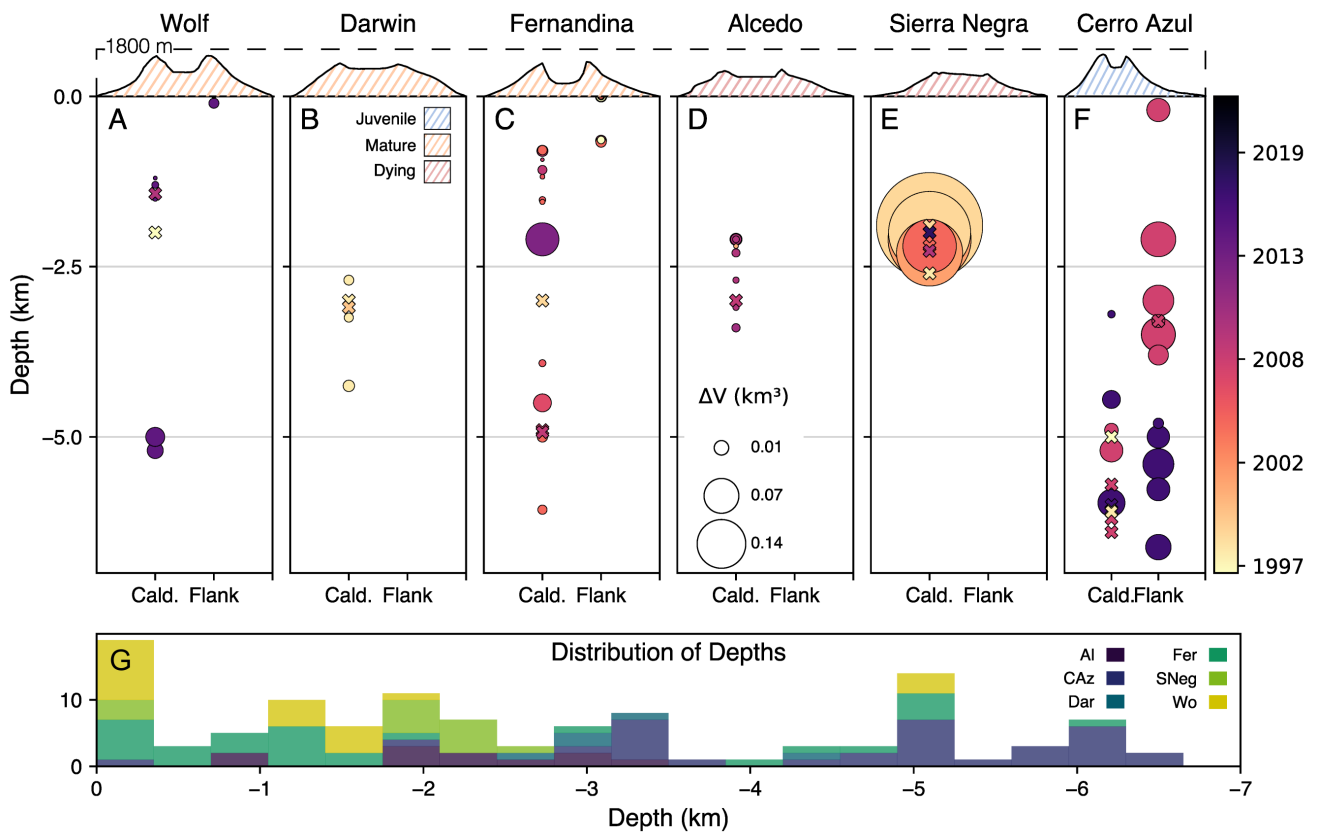


Figure 5: Summary of geodetic source depths in the western Galápagos, derived from InSAR data. In [A]–[F]. Depth, as stated in the corresponding study, is shown on the y-axes and general source location (sub-caldera or flank) topographic cross-sections are shown on the x-axes. Values and corresponding references are provided in Tables A1, A2, A3, A4, A5, and ??. The marker size reflects the relative volume change for each model solution, while colours indicates date that the inferred source was active. Where volume change is not given in the relevant publications, we assume a volume of $1 \times 10^7 \text{ m}^3$, for presentation purposes—these are differentiated by an \times marker. The colour of topographic cross sections reflects system maturity according to Harpp and Geist [2018]. [G] Histogram of the total distribution of depths for all volcanoes.

sub-volcanic reservoir. Bagnardi [2014] made volume flux estimates of magma supply to the six major Galápagos volcanoes, from 1992–2010, where Wolf accounted for approximately 1 % of total magma supply, less than both the recently inactive Darwin (3 %) and Alcedo (11 %). However, there has been a recent uptick in volcanic activity at Wolf, having erupted twice since 2010 (2015, 2022 [Venzke 2023]). Prior to this pair of eruptions, Wolf erupted eight times since 1900, with an average frequency of approximately 11 years between the 1925 and 2022 eruptions—since 2015, Wolf has been the second most active western Galápagos volcano, after Fernandina.

2.2 Darwin

Darwin volcano is located on Isabela Island, halfway between Alcedo and Wolf (Figure 2). It has an elevation of 1330 m, topped by a broad, shallow caldera (Figure 5), similar to both Alcedo and Sierra Negra. It is the least studied of the six major western Galápagos volcanoes, due to its extended extrusive quiescence.

2.2.1 Eruptive history

Like Fernandina and Wolf, Darwin has a narrow range of magmatic Mg# and storage temperatures [Geist et al. 2014; Harpp and Geist 2018], though it has infrequently erupted more evolved magmas, such as andesite [Naumann and Krebs 2003]. The Global Volcanism Program lists three Holocene eruptions at Darwin, including in $0210 \pm 500 \text{ CE}$ and $1150 \pm 300 \text{ CE}$. The most recent eruption took place in 1813, though the source volcano is ambiguous: it was “...more likely Darwin than Wolf, Alcedo” [Venzke 2023]. Evidence of thermal activity is similarly ambiguous, “strong thermal activity” was detected on the eastern flank of the volcano in 1972, via satellite observations [Venzke 2023]. However, a review of this imagery in 1973 suggested that the hotspots occurred on the caldera floor, and could be explained by “normal daytime temperature differences” [Venzke 2023]. Two tuff cones, Tagus and Beagle, are located on the coast, to the west of Darwin, indicating some prehistoric hydromagmatic volcanism [Banfield et al. 1956].

2.2.2 Previous observations of displacement at Darwin

The strongest evidence that Darwin's magmatic system remains active comes from the sparsely vegetated lava that covers it, and radar displacement studies. There was 20 cm of line-of-sight uplift between 1992–1998, attributed to a point source inflating by $5\text{--}8 \times 10^6 \text{ m}^3$ [Amelung et al. 2000; Manconi et al. 2007; Bagnardi 2014]. Following this, the caldera uplifted by five centimetres between 1998–2005, before it began to steadily subside until 2010, by a total of 5 cm (Figure 4) [Baker 2012]. During this period, there was heightened seismicity between Darwin, Fernandina, and Alcedo [Baker 2012]. From 1992–2010, magma influx at Darwin accounted for 3 % of the magma supplied to Galápagos volcanoes [Bagnardi 2014].

2.3 Fernandina

Fernandina volcano, located on the uninhabited Isla Fernandina, is the westernmost, and most active volcano in the Galápagos. It has the largest caldera (by depth and volume [Naumann and Geist 2000]), and in 1968 experienced the second largest global caldera collapse event of the 20th century (after Mount Katmai, 1912), when the volume of the caldera increased by $1\text{--}2 \text{ km}^3$ as the caldera floor fell by approximately 300 m [Simkin and Howard 1970]. Fernandina is the third tallest western Galápagos volcano, standing at 1476 m. It erupts frequently—the entire sub-aerial portion of the island has been resurfaced by lava flows in the last 4,300 years, and the island is hypothesised to lie over the centre of the Galápagos hotspot [Kurz et al. 2014].

2.3.1 Eruptive history

Fernandina has erupted 22 times since the turn of the 20th century. It has erupted, on average, once every 5.5 years since 1900, with VEI typically varying between 0–2. The largest eruption (VEI 4) occurred in June 1968, in a caldera forming event [Venzke 2023]. This eruption occurred in a series of steps, with major seismicity, ground deformation, trapdoor faulting, ashfall, infrasound detections, fumarole emissions, volcanic lightning, as well as the migration of the caldera lake from the northwestern corner to the southeastern [Simkin and Howard 1970; Filson et al. 1973; Rowland and Munro 1992].

Chadwick and Dieterich [1995] and Bagnardi et al. [2013] noted that the back and forth pattern of radial–circumferential fissure eruptions at Fernandina is due to stress field perturbations. That is, an intrusion from the shallow sub-volcanic sill can affect the stress field such that the least compressive stress promotes a succeeding intrusion of the opposite geometry (i.e. a radial eruption will be followed by a circumferential one) [Bagnardi et al. 2013]. They identify that the 2009 eruption of Fernandina occurred radially along the southwestern flank, and correctly predicted that the next eruption, in 2017, would be circumferential, along the southwestern caldera rim [IGEPN 2017d]. This pattern of alternating radial–circumferential eruptions continued through the 2018 and 2020 eruptions, though the locations varied to the north and eastern flanks [Venzke 2023]. Chestler and Grosfils [2013] suggested that reservoir geometry may also affect which orientation the eruptive fissure takes. Radial eruptions tend to

be more voluminous than circumferential ones, possibly due to increased driving force lower on the volcanic edifice [Geist et al. 2006b]. Eruption locations at Fernandina have a preferred NW–SE alignment [Rowland and Munro 1992]; during periods of low magma supply, the location of these eruptions is controlled by the regional stress regime, though eruptions may occur outside of this regime if magma supply increases [Rowland and Munro 1992]. Corbi et al. [2015] showed that stress changes following the 1968 caldera collapse controls the geometry of the shallow reservoir at Fernandina, and suggested that a combination of this, alongside buoyant and regional stresses may also explain the alternating intrusion geometry. The frequent eruptions at Fernandina result in a high degree of resurfacing of Fernandina Island [Kurz et al. 2014].

Fernandina entered a new eruptive phase on 02/03/2023, when lavas effused from a circumferential fissure on the southeastern flank [IGEPN 2024]. Notably, this intrusion geometry did not alternate from 2020, with both eruptions being circumferential.

2.3.2 Previous observations of displacement at Fernandina

Between 1992 and 1999, deformation at Fernandina was concentrated on the southwestern flank of the caldera, the site of the 1995 eruption, totalling almost 1 m of LOS uplift [Amelung et al. 2000]. Since then, displacement here has been non-linear, generally characterised by steady uplift, punctuated by rapid subsidence during episodes of unrest (Figure 4). This subsidence accompanied eruptions in 1995 and 2005 [Bagnardi and Amelung 2012; Baker 2012; Manconi and Casu 2012], 2017, 2018 [Galletto et al. 2023], and 2020. During eruptions there is rapid magma transfer and high magma mobility between sub-volcanic reservoirs [Galletto et al. 2023]. In each case, the resumption of uplift was immediate. The greatest observed amount of subsidence accompanied the 2009 eruption, when the caldera floor dropped by almost 1 m [Bagnardi and Amelung 2012]. More lava ($42.7 \times 10^6 \text{ m}^3$) was effused during this eruption than during the 2005, 2017, 2018 eruptions combined ($14.1 \times 10^6 \text{ m}^3$ DRE, $9.1 \pm 4.9 \times 10^6 \text{ m}^3$, $5.9 \pm 3 \times 10^6 \text{ m}^3$ DRE, respectively) [Vasconez et al. 2018]. Volumetrically, this eruption is comparable to the 1995 eruption ($42 \times 10^6 \text{ m}^3$ DRE) [Vasconez et al. 2018], though there were not enough SAR acquisitions either side of this eruption to characterise any syn-eruptive subsidence. At Fernandina, the majority of inter-eruptive magma accumulation occurs in the deeper sub-volcanic reservoir (at 5 km depth), and rapidly ascends though the shallow reservoir (1 km) during eruptions, evidenced by both geodesy [Bagnardi and Amelung 2012; Galletto et al. 2023], and petrology [Geist et al. 2006b; Stock et al. 2020].

2.4 Alcedo

Alcedo is located on Isabela, directly east of Fernandina Island, between Darwin and Sierra Negra (Figure 2). It peaks at 1130 m above sea level, approximately 4 km above the seafloor [Geist et al. 1994; Venzke 2023]. Like all western Galápagos volcanoes, it is topped by a summit caldera, varying in

width between 7 and 8 km with a maximum depth of 270 m (Figure 5) [Geist et al. 1994]. Its sub-aerial volume is approximately 200 km³, though Geist et al. [1994] suggested the majority of the volcano is underwater. Alcedo, alongside Sierra Negra, has a vigorous hydrothermal system, with three fumarole fields (Geyser, Laura and Chantel, and Rhyolite Hill), all located on the southern side of the volcano, within the caldera [Goff et al. 2000; Mayhew et al. 2007] (Figure 13). The volcano's gentle slopes and low levels of extrusive activity have made Alcedo home to the highest population of Galápagos tortoises on Earth [De Roy 2010].

2.4.1 Eruptive history

Alcedo is the only volcano on Isabela or Fernandina known to have erupted rhyolitic lavas in its geological history (≤ 120 ka) [Geist et al. 1994]. It has erupted in the 20th century, once in 1953, and again as a steam explosion in 1993 [Siebert et al. 2010]. The 1953 eruption occurred on volcano's southeastern flank, while the 1993 event took place on the southern caldera wall [Siebert et al. 2010]. During the 1993 event, seismicity, heightened fumarolic activity, and explosions were recorded, due to explosive phreatic activity from two vents [Green 1994].

2.4.2 Previous observations of displacement at Alcedo

Despite its low levels of extrusive activity, Alcedo has been constantly deforming since 1992, and accounted for approximately 11 % of intrusive magma flux, as detected by InSAR, of the western Galápagos between 1992 and 2010 [Bagnardi 2014]. Amelung et al. [2000] performed an InSAR survey of Isabela and Fernandina from 1992–1999. Alcedo uplifted by > 90 cm over this time, with the majority (approximately 80 cm) occurring between 1992 and 1997. Following this uplift the direction of deformation inverted to subsidence. Using Persistent Scatterer analysis, Hooper et al. [2007] observed a deflation signal of > 30 mm yr⁻¹ between 1997 and 2001, and attribute it to the crystallisation of a pipe-like magma body at 2.2 km depth. There may be a relationship between the uplift at Alcedo observed by Amelung et al. [2000], and its 1993 explosion. However, the sparse temporal spacing of the surrounding acquisitions means that the exact relationship between the timing of the observed uplift and the explosion is unclear. We suggest that magmas intruded during this uplift crystallised, causing the subsequent subsidence observed by Hooper et al. [2007], though contraction throughout the cooling sub-volcanic system may also cause this subsidence. Subsidence continued largely uninterrupted until 2006, with a minor uplift phase in 2004 [Baker 2012; Galetto et al. 2019]. Following this, Alcedo experienced a series of magmatic intrusions, which may represent a component of longer term resurgence [Galetto et al. 2019]. Between 2007–2009, sill inflation caused the caldera floor to uplift by approximately 30 cm, at a rate of approximately 8.9 cm yr⁻¹ [Galetto et al. 2019]. This same area then subsided by 8 cm, until June 2010, while the western caldera rim uplifted by 5 cm [Galetto et al. 2019], due to intra-caldera magma migration. Finally, the eastern portion of the caldera resumed uplift between June 2010 to March 2011 [Galetto et al. 2019]. In each case, the best-fit sill depth is 2–3 km beneath the caldera floor, while the deformation patterns are asymmetrical, suggesting contribution

from the intra-caldera fault [Galetto et al. 2019]. Likewise, Bagnardi [2014] suggested deformation trends at Alcedo are due to a combination of magmatic and volcano-tectonic structures, from a Mogi source at 3 km depth and a SSW–NNE striking reverse fault. The hydrothermal system [Goff et al. 2000] probably also contributes to deformation here. Part of this episode of resurgence, the period from 2009–2011, is notable for producing higher magnitude seismicity ($M_L \leq 3.3$) than Fernandina ($M_L \leq 2.5$) and Sierra Negra ($M_L \leq 1.5$) [Davidge et al. 2017].

2.5 Sierra Negra

Sierra Negra is 1124 m tall, and constitutes the entire southeastern corner of Isla Isabela [Reynolds et al. 1995]. It is the most voluminous, with the greatest sub-aerial extent, of all western Galápagos volcanoes [Reynolds et al. 1995]. The exposed edifice and lava flows (2.03×10^9 m²) constitute approximately 44 % of the entirety of Isla Isabela (4.6×10^9 m²). In contrast to the northern volcanoes, Sierra Negra is the best studied volcano in the western Galápagos, and has been the subject of InSAR, GPS, and gravity surveys (Table A5). This is likely due to: (a) Its ease of access from Puerto Villamil, the primary population centre on Isabela and (b) Its extraordinary deformation behaviour (the caldera uplifted by 6.5 m from 2005–2018 [Bell et al. 2021b]). Sierra Negra has probably maintained this high degree of extrusive activity for millennia—90 % of the volcano has been resurfaced in the past 4,500 years, with an average long-term eruptive rate of 1×10^6 m³ yr⁻¹ [Reynolds et al. 1995]. Inflation of a shallow sill, at 2 km depth (Table A5), is the primary cause of uplift at Sierra Negra, with slip along the trapdoor fault contributing to co-eruptive subsidence. Influx of magma into the sill promotes slip along the trapdoor fault, causing asymmetric deformation across the entire caldera floor [Amelung et al. 2000; Jónsson et al. 2005; Chadwick et al. 2006; Jónsson 2009]. Jónsson et al. [2005] suggested that the trapdoor fault inhibits southbound sill growth, and instead promotes eruptions on the northern flank, from a dike rooted to the sill. This hypothesis is supported by observations, with each of the four eruptions since 1963 having taken place in the northern sector of the volcano [Ven-zke 2023], and there having been five large earthquakes due to fault slip in January 1998, April 2005, October 2005, June 2018, and July 2018 following stress accumulation [Amelung et al. 2000; Jónsson et al. 2005; Chadwick et al. 2006; Geist et al. 2008; Jónsson 2009; Gregg et al. 2018; Bell et al. 2021b]. Sierra Negra, like Alcedo, has an active hydrothermal system, on the western segment of the caldera fault [Reynolds et al. 1995; Goff et al. 2000; Aiuppa et al. 2022]. Fumaroles here produce magma-derived gases that have exsolved from the shallow sill, and been channeled to the surface by the trapdoor fault [Aiuppa et al. 2022]. The trapdoor fault dominates the expression of volcanism at Sierra Negra: it actively promotes fumarolic activity in the west of the caldera [Aiuppa et al. 2022], slip along it can trigger eruptions [Gregg et al. 2018], the location of which is controlled by the accompanying stress field [Gregg et al. 2018], and interplay between the fault and the shallow sill produces asymmetric deformation patterns [Amelung et al. 2000].

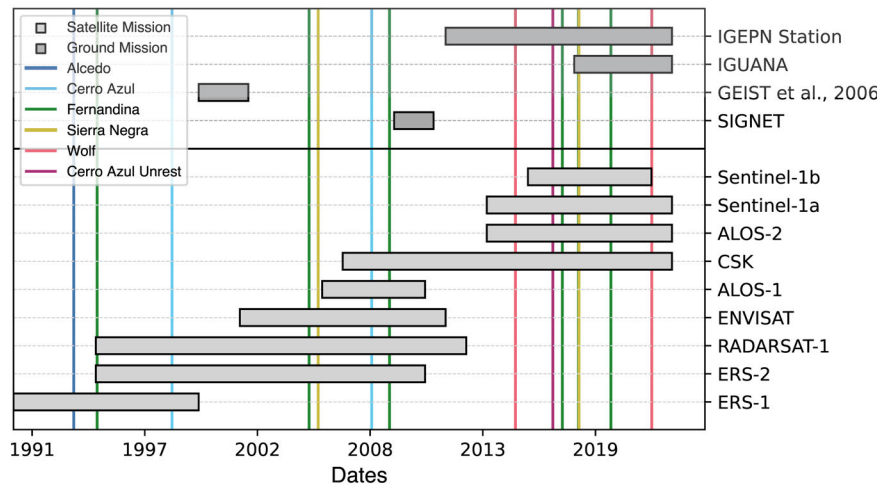


Figure 6: Temporal distribution of geophysical measurements since the the first InSAR studies in the western Galápagos in the 1990s until 2023. Horizontal bars represent the time periods over which satellite missions and ground-based monitoring are active (Locations in Figure 1). Vertical lines represent eruptions, or significant unrest. Each included geophysical platform has been used to study unrest in the western Galápagos.

2.5.1 Eruptive history

Sierra Negra has erupted twice in the 21st century, first in 2005, and again in 2018. Prior to this it last erupted in 1979, one of seven 20th century eruptions. There was an average eruptive frequency of 13 years between 1911 and 2018 [Venzke 2023], though our understanding of the sub-volcanic plumbing system is derived from the 2005 and 2018 eruptions.

The 2005 eruption (October 22nd) initiated explosively, with a 13 km plume, followed by three stages of variable lava fountaining (total erupted volume of 1.5×10^8 m³, from a sill located at 2.1 km depth [Geist et al. 2008], with a source volume loss of 1.2×10^8 m³ [Manconi and Casu 2012]). This eruption has a clear top-down seismic control, with no eruptive precursors in cGPS data [Geist et al. 2008] in the days leading up to the eruption. The magmatic reservoir was in a stable state of stress prior to the eruption, and had not reached a critical overpressure threshold [Gregg et al. 2018]. Instead, the eruption was “catalyzed” by a mag. 5.5 earthquake three hours prior to its onset [Gregg et al. 2018]. This earthquake caused 84 cm of dip-slip displacement on the southwestern portion of the intra-caldera trapdoor fault [Geist et al. 2008], sufficiently modifying the local static stress to trigger an eruption. As at Fernandina (e.g. Bagnardi et al. [2013]), the location of an event that modifies the local stress field has a major control on the dynamics of the succeeding eruption—the mag. 5.5 earthquake relieved stress along the southern portion of the caldera while increasing tensile stress on the northern section of the caldera and magmatic system [Gregg et al. 2018].

Perhaps the most striking features of the 2018 eruption (June 26th–August 23rd) are the similarities with the 2005 eruption [Bell et al. 2021a; b; Gregg et al. 2022]. Lavas again effused from a rupture on the northern flank of the caldera, following a mag. 5.4 slip on the southwestern section of the trapdoor fault [Bell et al. 2021b]. Neither cGPS, nor tilt data, indicated imminent unrest in the hours before eruption [Bell

et al. 2021b], though shear wave velocities indicate a pulse of shallow magma intrusion in the preceding 17 days [Ruiz et al. 2022]. The earthquake was followed by a seismic swarm on the northwestern trapdoor fault section, eastward migrating seismicity, and pre- and co-eruptive tremor [Bell et al. 2021b; Li et al. 2022]. The eruption lasted three months, and was comprised of three phases [Shreve and Delgado 2023]. The caldera floor subsided by > 6 m during the initial eruptive phase [Shreve and Delgado 2023], as lava effused from both summit, and distal fissures (Figure 2), covering an area of 17 km² [Vasconez et al. 2018]. On July 7th, a M_w 5.0 earthquake coincided with subsidence of the southwestern section of the caldera by up to 71 cm [Bell et al. 2021b; Sandanbata et al. 2021]. Following this, the caldera, and lateral sill subsided by 2.5–3 m, and 0.25 m, respectively [Shreve and Delgado 2023]. Lava extrusion during this period was concentrated on the distal fissure, covering an area of 13 km² [Vasconez et al. 2018].

2.5.2 Previous observations of displacement at Sierra Negra

Amelung et al. [2000] observed up to 2.4 m of uplift in the caldera, between 1992 and 1998. Following this, the caldera floor subsided between 2000 and 2002, at a rate of approximately 9 cm yr⁻¹ as observed by GPS data [Geist et al. 2006a], and InSAR data [Baker 2012]. This continued until April 2003, at which point the centre of the caldera uplifted by 2.2 metres preceding its 2005 eruption [Geist et al. 2008]; the cumulative uplift from 1992–2005 was approximately 5 m [Geist et al. 2008]. The high-magnitude inter-eruptive uplift at Sierra Negra is matched by similar co-eruptive subsidence—the caldera floor subsided by 5 m in 2005, and the entire volcano contracted horizontally by six metres [Geist et al. 2008]. Uplift immediately resumed after the 2005 eruption, and was sustained for 13 years (with > 4 sub-phases of deformation) [Geist et al. 2008; Bell et al. 2021b]. In total, the caldera inflated by > 6.5 m as magma accumulated at two kilometres depth [Bell

et al. 2021b]. This depth is consistent with the source of the 2005 eruption [Geist et al. 2008], and agrees with that suggested by gas composition analysis, as well as magma equilibration depths [Bell et al. 2021b; Aiuppa et al. 2022]. The sills that fed the distal fissure are spectacularly observed in the InSAR displacement maps of the eruption (e.g. Bell et al. [2021b] and Davis et al. [2021]). It initiated in the northwestern section of the caldera before separating into two lobes, the larger of which migrated to the west, before deflecting northeast, and surfacing. Davis et al. [2021] showed that this curvature is caused by the interaction between the topographic stress gradient, and that of the sill buoyancy. Co-eruptive subsidence in 2018 exceeded the pre-eruptive uplift by 2 m (8.5 m total) [Bell et al. 2021b], with Shreve and Delgado [2023] suggesting that caldera formation at Sierra Negra may be caused by the accumulation of metre-scale subsidence during regular eruptions.

2.6 Cerro Azul

Cerro Azul is the southernmost volcano on Isabela, located to the west of Sierra Negra (Figure 1). It peaks at 1640 m elevation, with a volume of 172 km³ [Naumann and Geist 2000], and has the smallest caldera of all western Galápagos volcanoes (3.1 km³). The caldera is the third deepest, at 450 m, but has the smallest area by far (9.5 km², less than half Fernandina (20.1 km²)) [Naumann and Geist 2000] (Figure 5). A lake periodically occupies the caldera floor, and may have contributed to the 1943 hydrovolcanic eruption, causing the only known fatality from a Galápagos eruption [Siebert et al. 2010].

2.6.1 Eruptive history

Cerro Azul is one of the more active volcanoes in the western Galápagos, having erupted 11 times in the past 100 years—only Fernandina erupts more frequently [Venzke 2023]. It erupts, on average, once every 6.6 years [Naumann and Geist 2000] from its caldera, summit, and flanks [Naumann and Geist 2000]. It has erupted twice since 1992, once in 1998, and again in 2008. During the 1998 eruption, two vents opened within the caldera accompanied by another on the southeastern flank [Naumann and Geist 2000; Teasdale et al. 2005]. The eruption lasted 36 days, with eruption plumes, and lava flows along the eastern flank of the caldera—the longest of which was 16 km [Mouginis-Mark et al. 2000]. The erupted magma (DRE $5.4 \pm 2.4 \times 10^7$ m³, with mean effusion rate of 17 m³ s⁻¹ [Rowland et al. 2003]) mixed with residual magma from the 1979 eruption during the first 18 days, before changing compositionally as this remnant magma depleted [Teasdale et al. 2005]. Like in 1998, the 2008 eruption also issued from effusive fissures on the southeastern flank of Cerro Azul [Baker 2012; Galetto et al. 2020], initiating on May 29th, and lasting for 19 days [Venzke 2023]. Lava erupted from fissures in the upper part of the cone until June 1st, before erupting from radial fissures along the base of the eastern flank on June 3rd (e.g. Figure 2).

2.6.2 Previous observations of displacement at Cerro Azul

The 1998 eruption marks the first significant displacement observation at Cerro Azul [Baker 2012; Galetto et al. 2020]. This

eruption was accompanied by 15 cm of subsidence, from a source between 5 and 6.1 km depth, with a radius of 0.2 km [Amelung et al. 2000; Baker 2012; Bagnardi 2014]. The inter-eruptive period between this and the 2008 eruption was characterised by steady uplift, totalling > 20 cm. During the 2008 eruption, the caldera summit subsided by 30 cm [Galetto et al. 2020]. Again, this subsidence was modelled using sources from 5–6.4 km beneath the caldera [Baker 2012; Galetto et al. 2020] (Table A2). It is likely that this is the primary magma reservoir depth at Cerro Azul, though Naumann et al. [2002] found evidence of tholeiitic magma storage at a range of depths from 3–15 km. However, during this eruption, a dike rooted to the sub-caldera source was also modelled, acting as a conduit between the magma reservoir and the eruptive fissures [Baker 2012; Galetto et al. 2020] (Table A2). Galetto et al. [2020] likened this lateral dike to those at Fernandina, where sills derived from a sub-caldera source bend upwards as they propagate, due to the stress field exerted by the volcano.

Uplift resumed following the 2008 eruption [Baker 2012]. Cerro Azul then underwent a major unrest episode in March 2017, with an uptick in seismicity consistent with an ascending magma body, leading to eruption warnings [IGEPN 2017a; b]. Ultimately, no eruption occurred [IGEPN 2017c], though there was peak subsidence of 32.9 cm in the caldera, and uplift of 41.8 cm on the southeastern flank [Guo et al. 2019]. Like in 1998, and 2008, this deformation was modelled using a geodetic source approximately 5 km beneath the caldera, from which a sill propagated causing surface uplift [Guo et al. 2019] (Table A2).

3 METHODS

3.1 InSAR data and time series

The Sentinel-1 imagery used in this study was processed using the LiCSAR automatic InSAR processor [Lazecký et al. 2020]. In this workflow, interferograms are geocoded with a pixel spacing of approximately 100 m, with minimum temporal baseline of 6–12 days, when Sentinel-1A, and Sentinel-1B were in constellation. We performed a quality check of the final interferograms to identify errors (e.g. in the unwrapping process) that may have occurred during the automated workflow. These interferograms were removed, and recreated, and data gaps were backfilled to ensure a connected network. We also corrected for errors introduced by tropospheric phase delay, using the Generic Atmospheric Correction Online Service (GACOS) [Yu et al. 2018]. Here, estimated maps of tropospheric phase delay are constructed, using data from the European Centre for Medium-Range Weather Forecast, and removed from the unwrapped interferogram. Using the GACOS correction on the descending dataset reduced the standard deviation of the unwrapped phase dataset to 2.7 from 3.2 radians, and for the ascending data, it increased to 4.27 radians, from 4.12. We used these corrected data to construct time series of displacement, using the LiCSBAS time series analysis software [Morishita et al. 2020]. This small-baseline inversion software utilises phase loop closure, to identify and remove bad interferograms before performing the time series inversion. The final time series were filtered, spatially and temporally, using a Gaussian Ker-

nel. We used the default filter sizes in LiCSBAS: 2 km spatially, and three times the average interval temporally. In the time series figures here (e.g. Figure 8), displacement is given in the Line-of-Sight direction, in metres, where positive is uplift (i.e. towards the satellite).

3.2 Geodetic source modelling

Deformation source modelling was conducted using the MATLAB-based Geodetic Bayesian Inversion Software (GBIS) [Bagnardi and Hooper 2018]. This software models analytical sources in an elastic half-space using a Bayesian approach to estimate the posterior probability density functions of model parameters, sampled using a Markov chain Monte Carlo method [Bagnardi and Hooper 2018]. To compare observed and modelled displacements, we present the maximum a posteriori solution (e.g. Figure 13), while data uncertainties were characterised using an experimental semi-variogram, calculated over a non-deforming area, away from the volcanic edifice. To perform the modelling for each volcano, we first cropped the cumulative displacement maps from our time series inversion to the area surrounding the volcano. We selected the time windows for modelling cumulative displacement to isolate different episodes of deformation (e.g. spanning the uplift at Darwin (Figure 8)). In each case, displacement was downsampled using a quadtree algorithm, and the inversion ran for 1×10^6 iterations. When performing joint inversions using both descending and ascending data, the acquisitions for each track are typically offset by one day, and do not overlap exactly in time. Therefore, for modelling purposes we assume that the displacement between the acquisitions is negligible. For each volcano, the variety of volcanic processes informed our modelling strategy. At Darwin, we only considered positive volume change, in sill or Mogi models. At Wolf, we compared analytical source geometries to calculate the maximum inter-eruptive volume change. At Fernandina, we tried to simplify the modelling by using the smallest post-eruptive intervals of cumulative displacement, to minimise the number of active modelled sources. We searched for spatial parameters (x location, y location, and depth), as well as volume change when considering Mogi sources, and geometric parameters (length, width, depth, strike, dip) when considering sills and dikes. Unless stated, we did not impose strict limits on these parameters, searching across the entire volcanic edifice, with lower depth limits of 10 km. We informed our choice of geodetic source model by previously calculated source parameters (e.g. Bagnardi and Amelung [2012]) to assess how sources have changed through time. For example, joint Mogi and sill models have previously been proposed at Fernandina [Bagnardi and Amelung 2012], and Mogi sources used at Darwin [Amelung et al. 2000]. We generally preferred dislocation sources to point sources, as we consider them to better represent magmatic intrusions, but do use Mogi sources to better fit some data. In instances where we consider multiple potential deformation sources (Figure 7), we estimated the goodness-of-fit by calculating the reduced χ^2 statistic [Li et al. 2021] as it allows comparison between models with different numbers of parameters, where a lower value represents

a better fit. χ^2 is given by:

$$\chi^2 = \sum_i \frac{1}{v} \frac{(O_i - C_i)^2}{\sigma_i^2}, \quad (1)$$

where O_i is the observed data, C_i is the model output, v is the degrees of freedom, and σ_i^2 is data variance. In each case we present the data, model, and residual, each projected into the satellite line-of-sight.

3.3 Volcanic areas and extents

We map surface features, such as lava flows, to visualise the extent of eruptions, and to estimate erupted volumes for the 2008 and 2020 eruptions of Cerro Azul and Fernandina, respectively. We present offshore rift zones and lava fields to provide context for the 2020 Fernandina eruption. This mapping was conducted in QGIS. Maps of volcanic features that had been identified in previous studies were imported into QGIS, and georeferenced using the Georeferencer, in the Raster toolbox. The extents of these features were then manually extracted from the georeferenced maps, and converted to polygon vector files, from which variables such as area were calculated (using the EPSG:3857 Coordinate Reference System). This process was carried out for lava fields, bathymetric data, and previously modelled intrusions, using existing maps from published studies (cited in their corresponding sections), or from optical satellite imagery. Maps including bathymethyric data were created using data from the GEBCO Compilation Group (2022) (GEBCO_2022 Grid; doi:10.5285/e0f0bb80-ab44-2739-e053-6c86abc0289c).

4 NEW OBSERVATIONS OF DEFORMATION IN THE WESTERN GALÁPAGOS

4.1 Inter-eruptive flux at Wolf

Wolf had been steadily uplifting since its 2015 eruption, between May and July 2015 (Figure 4). There are some Sentinel-1 acquisitions around the eruption [Xu et al. 2016] though regular acquisitions did not begin until 14/11/2015. These acquisitions were exclusively in the descending direction until 06/01/2017, when the ascending track became available. In total, data are available in the descending direction for 96 % of the inter-eruptive period. Using these data, we estimate the intrusive flux into Wolf for cumulative displacement from 14/11/2015 until 24/12/2021, just prior to the 2022 eruption. The results of the models for best fitting sill, sill–sill combination, and dike, are presented in Table 1, and Tables A19–A21, with corresponding data, model, and residuals in Figure 7. We also perform joint inversions from 2017–2022, after ascending data began to be acquired (Figures A7 and A8), and Table A22. Between 2015–2022, the sill–sill, and dike models fit the data better than single sill, with reduced χ^2 values of 0.13, 0.13, and 0.28, respectively—though the extreme aspect ratio of the deeper sill in Table 1 suggests that the dike may be the most realistic model. However, Liu et al. [2019] and Xu et al. [2023] suggested that a single source combined with ring faulting may explain deformation patterns at Wolf. If this were the case, our models may overestimate the geodetic source volume change.

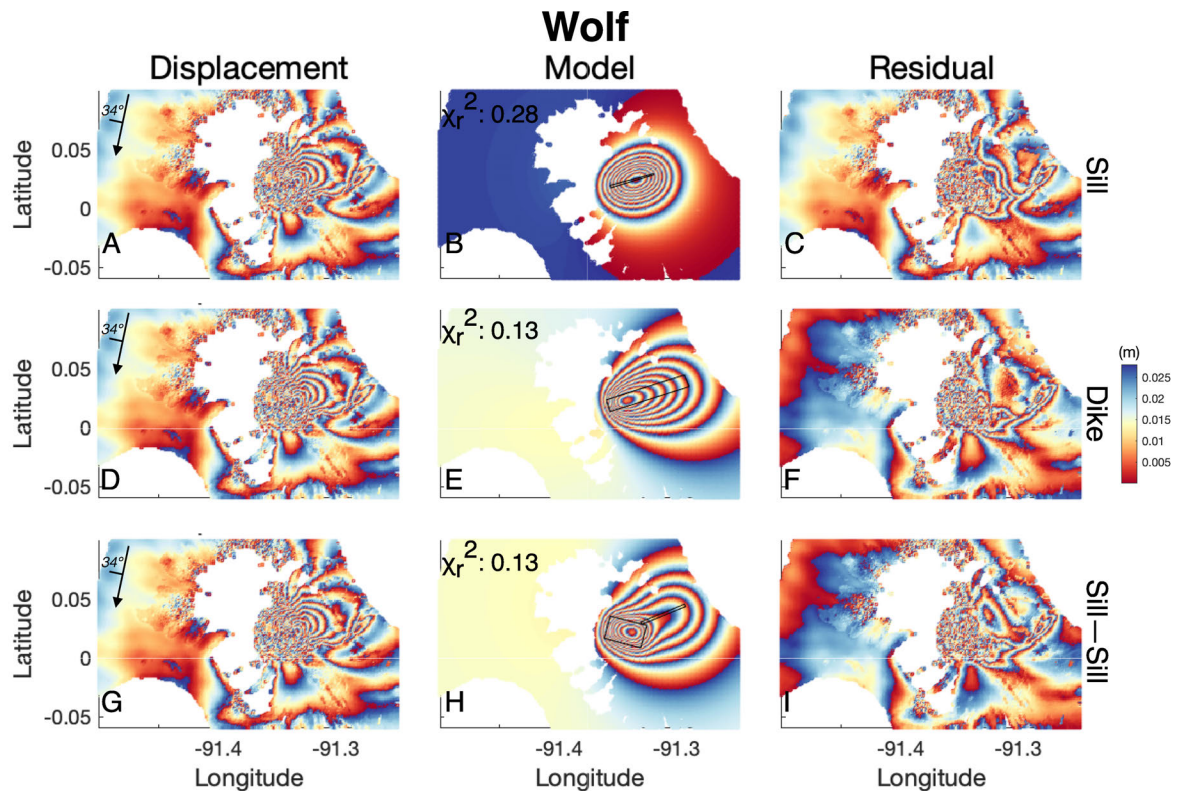


Figure 7: Best-fit geometries for source inflation at Wolf from 14/11/2015–24/12/2021, just prior to its 2022 eruption. Each fringe corresponds to 2.8 cm of LOS displacement, in the descending track direction. [A]–[I] Observed, modelled, and residual displacements, for the best fitting sill, dike, and sill–sill geometries. Inset arrow shows satellite heading and incidence angle. Modelled geometry is outlined in black. Unwrapped data can be seen in [Figure A6](#).

Table 1: Volumes for best fitting sources at Wolf. In the Expanded ΔV column, the modelled volume (over a period equal to 96 % of inter-eruptive time) has been expanded to estimate the total volume flux over the total eruptive period, assuming a constant intrusion rate. The fraction columns represent the percentage of erupted lava that intruded during the entire inter-eruptive period.

Source	Length (m)	Width (m)	Opening (m)	Depth (m)	Observed ΔV (m^3)	Expanded ΔV (m^3)	Fraction of erupted lava (%)	DRE fraction (%)
Sill	170	4171	8.8	2600	6.1×10^6	6.4×10^6	27	36
Dike	1454	7748	0.94	1482	1.1×10^7	1.1×10^7	47	62
Sill–Sill	3508	2189	0.43	1545	1.1×10^7	1.1×10^7	47	63
	250	4432	8.3	5295				

These estimates show that, depending on geometry, the inter-eruptive intrusive flux only accounts for between a quarter to a half of the lava that was erupted during Wolf’s 2022 eruption. There are several potential explanations for this: (a) There was a change in magma dynamics during the pre-eruptive and eruptive periods. (b) Vesiculation and bubble nucleation resulted in the amount of magma being underestimated as compressibility is not considered in these models. For lavas at Fernandina and Sierra Negra, [Vasconez et al. \[2018\]](#) find that DRE volumes are approximately 25 % smaller than those of the erupted magmas. When comparing magma influx to a DRE of 25 % less than the erupted lavas, we still find that between one and two thirds of the lava is unaccounted for. (c) We assume a constant influx rate from the end of the

2015 eruption to the onset of the 2022 eruption, to account for the period until regular InSAR monitoring began (4 % of the total time). Perhaps the influx rate was much higher during this time, and can account for the missing one–two thirds, though we consider this implausible. (d) The missing lava was intruded during the three months of the eruption, rapidly flushing through the subvolcanic system before erupting, as suggested by [Stock et al. \[2020\]](#).

4.2 Resurgence at Darwin

Using Sentinel-1 InSAR data, we see low magnitude (< 3 cm) uplift and subsidence from 2017–2022, though we measure an episode of uplift of approximately 6 cm LOS at Darwin, from April 2020 until June 2021 ([Figure 8](#)).

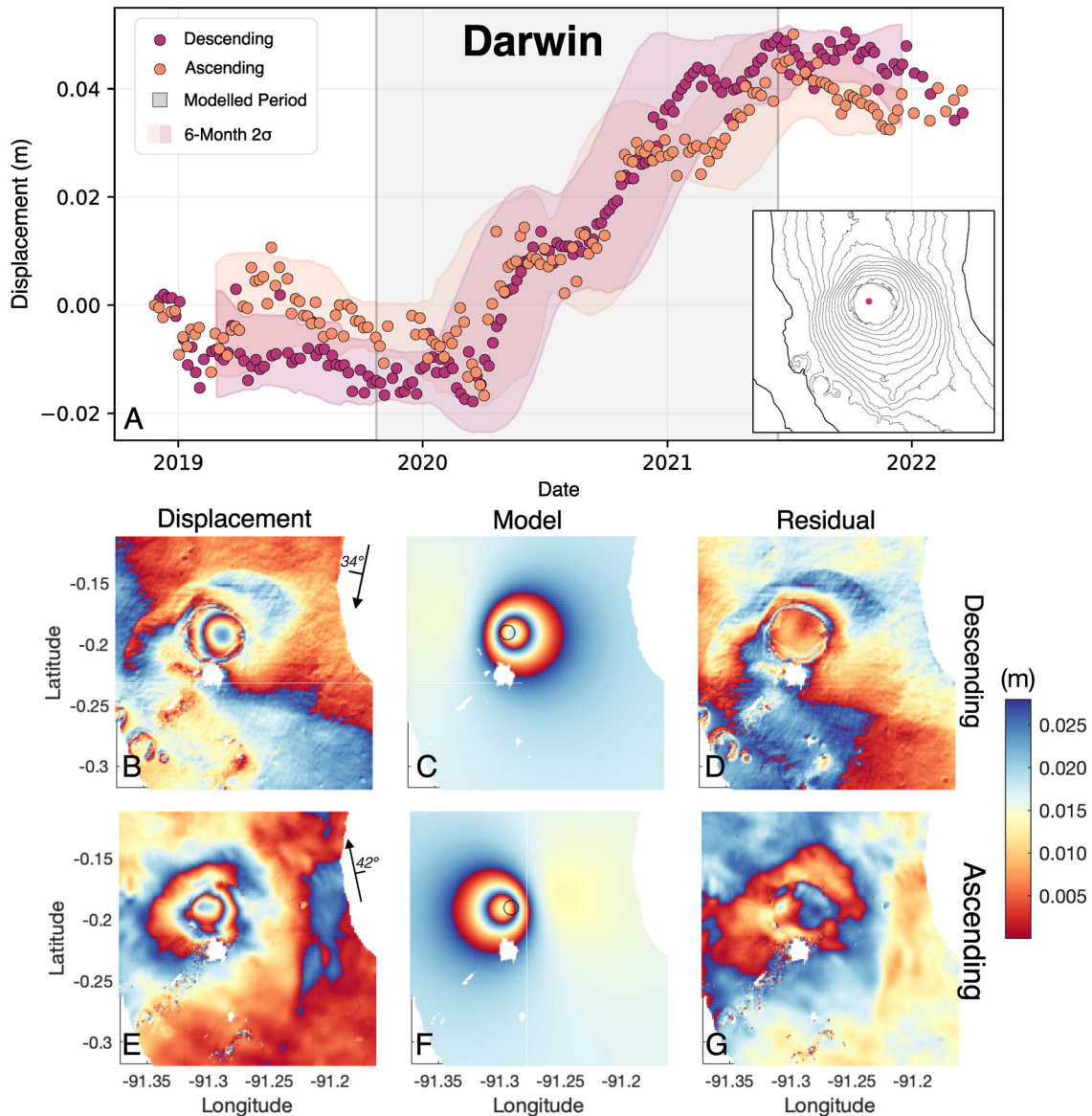


Figure 8: Uplift at Darwin volcano for a point at -0.192° N, and -91.287° E (dot on inset map). [A] Time series of uplift in descending and ascending track directions, accompanied by the second standard deviation across 6-month rolling windows. The grey box indicates the modelled period, from 23/10/2019–15/06/2021. [B]–[D] Observed, modelled, and residual displacements, in the descending track direction. Inset arrow shows satellite heading and incidence angle. [E]–[G] Observed, modelled, and residual displacements, in the ascending track direction. Cumulative displacement across the modelled window is relative to a reference point at $-91.32; -0.2974$. The best-fit Mogi source is located at 2.6 km depth, and inflated by $1.6 \times 10^6 \text{ m}^3$ over the modelled period. Its location is annotated by a black circle.

We modelled the source of this uplift (Section 3), using both ascending and descending track directions. Though we consider sill geometries to be better representations of real magma intrusions than point sources, previous studies have identified Mogi sources at Darwin [Amelung et al. 2000; Manconi et al. 2007]. Therefore we model this deformation using both Mogi (Figure 8) and sill (Figure A5) sources. The best-fit sill geometry is elongate (140 m by 2300 m), located at 3.3 km depth, and opened by 4.9 m. The Mogi source is located at 2.6 km, and inflated by $1.8 \times 10^6 \text{ m}^3$ over the modelled period. The reduced

χ^2 statistic, using descending and ascending data, shows that the Mogi source (3.45 and 0.6) is a slightly better fit, compared to the sill (3.55 and 0.79). Additionally, the highly elongate geometry is unusual for sill intrusions. The complete modelling results are presented in Tables A9 and A10. Both models show similar intrusive volumes (Mogi: $1.8 \times 10^6 \text{ m}^3$, $1.6 \times 10^6 \text{ m}^3$), though the Mogi source (2.6 km) is 700 m shallower than the sill, and falls just outside the previous range of estimates (2.7–4.25 km) presented in Table A3. The 2020 episode of uplift at Darwin was similar to the uplift observed there between 1992

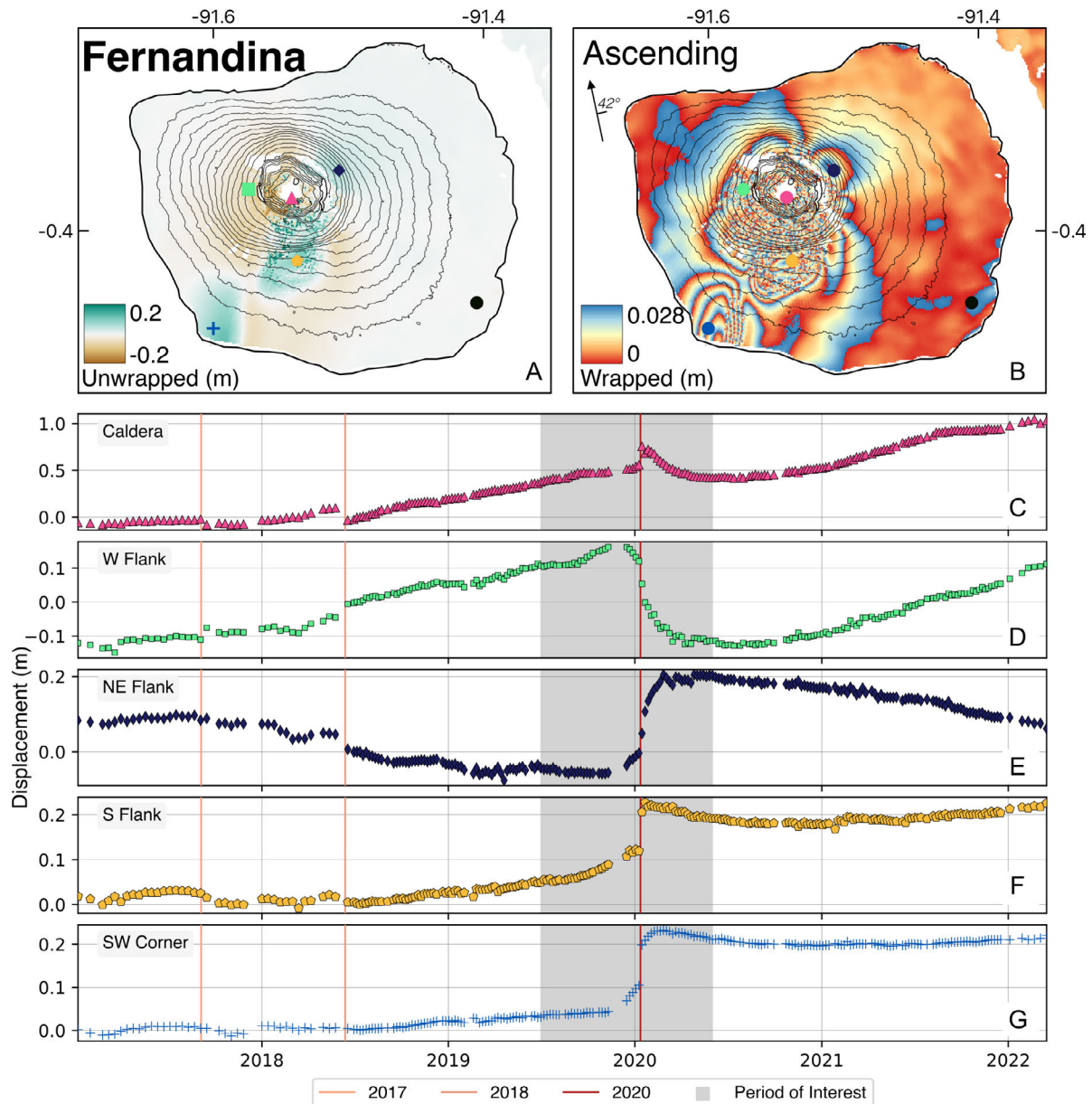


Figure 9: Eruptive displacement for the 2020 eruption at Fernandina, in the ascending Track direction, relative to reference point on the east of the island (black dot). Inset arrow shows satellite heading and incidence angle. [A] Unwrapped displacement (m) at Fernandina Island, from 09/01/2020–15/01/2020, spanning the eruption. [B] Wrapped displacement (m) at Fernandina Island, from 09/01/2020–15/01/2020, spanning the eruption. [C]–[G] Time series of displacement from 2017–2022 for a point in Fernandina’s caldera, western flank, northeastern flank, southern flank, and on the southwestern edge of the island, relative to a point on the southeast of the island.

and 1997 [Amelung et al. 2000] and indicates that, despite its eruptive quiescence, magma periodically intrudes into Darwin’s sub-volcanic system.

4.3 The 2020 Eruption at Fernandina

Deformation of Fernandina in the Sentinel-1 era has continued as steady inter-eruptive uplift, varying from 10 cm yr^{-1} between 14/11/2015–01/07/2018, to 35 cm yr^{-1} between 01/07/2018–04/01/2020. During the 2017 and 2018 eruptions, syn-eruptive deformation was short-lived (Figure 4). Galetto et al. [2023] observed up to 38 cm of co-eruptive subsidence

and uplift in 2017 and $< 20 \text{ cm}$ of co-eruptive subsidence in 2018, while the caldera floor uplifted by $< 14 \text{ cm}$ in the inter-eruptive period. However, the 2020 eruption is strikingly different—though the sub-aerial component of the eruption lasted only a day [Venzke 2023], various locations around Fernandina island continued to deform for a three month period from 05/01/2020–14/03/2020 (Figures 9 and 10). This was accompanied by uplift to the west, and south of the caldera (Section 4.3). In November 2021, IGEPN noted heightened fumarolic activity in the caldera, as well as seismic tremor, and suggested that they may evolve into an eruption in the

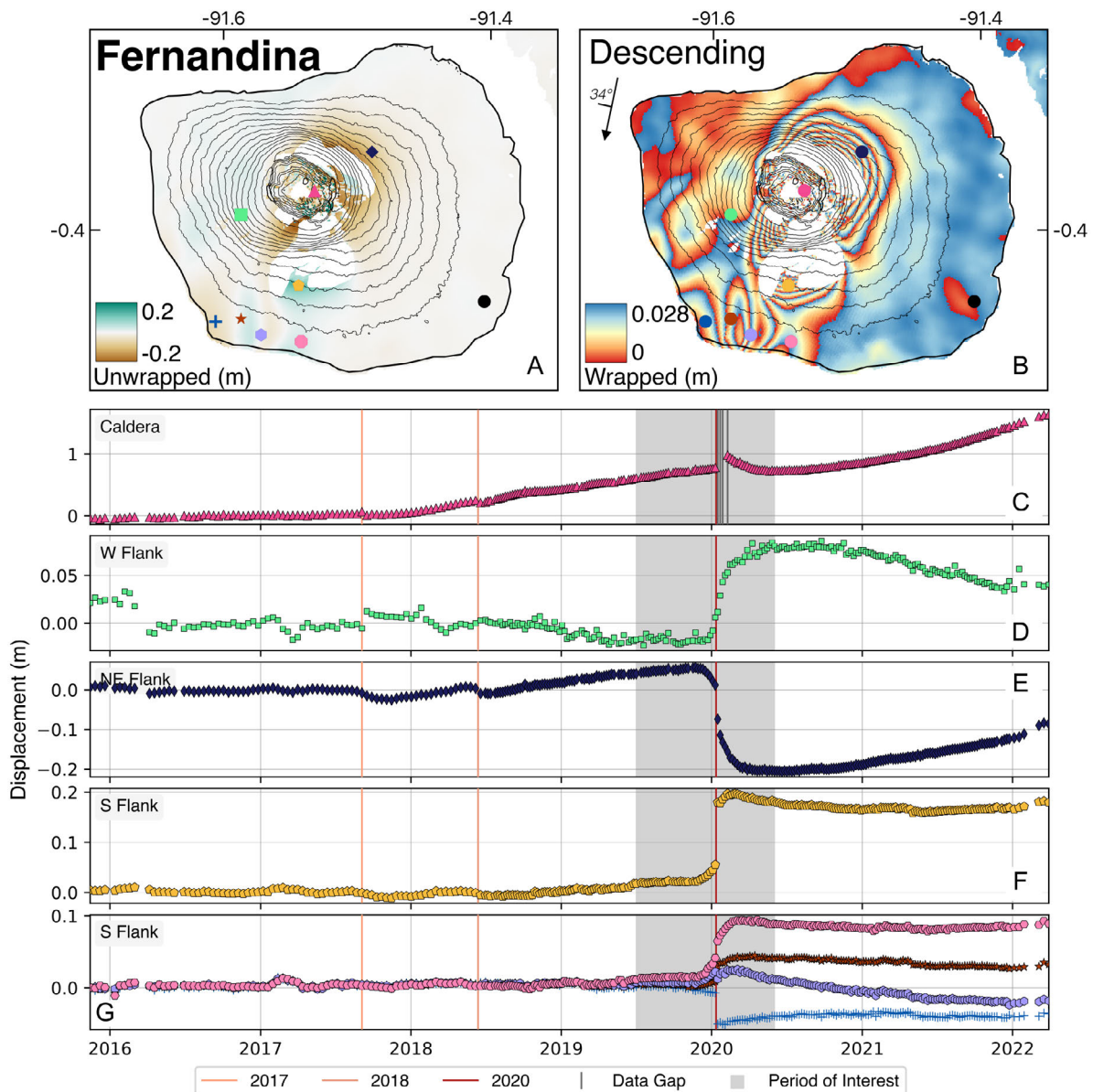


Figure 10: Eruptive displacement for the 2020 eruption at Fernandina, in the descending Track direction, relative to reference point on the east of the island (black dot). Inset arrow shows satellite heading and incidence angle. [A] Unwrapped displacement (m) at Fernandina Island, from 10/01/2020–16/01/2020, spanning the eruption. [B] Wrapped displacement (m) at Fernandina Island, from 10/01/2020–16/01/2020, spanning the eruption. [C]–[G] Time series of displacement from 2015–2022 for a point in Fernandina’s caldera, western flank, northeastern flank, southern flank, and several points on the southwestern edge of the island, relative to a point on the southeast of the island.

medium to long term [IGEPN 2021a]. Ultimately, this did not lead to an eruption, though this unrest was accompanied by accelerated uplift, beginning in October [IGEPN 2021b].

Fernandina erupted on January 12th, 2020. The subaerial component of this eruption was minor—small lava flows effused from an eastern circumferential fissure and it did not exceed VEI 0 (the first VEI 0 eruption at Fernandina in almost 40 years (1981)) [Venzke 2023]. The USGS Seismic Catalogue shows a magnitude 4.6 earthquake occurred on the southern flank of the volcano approximately half an hour prior to the eruption (Figure 12). Sentinel-1 interferograms spanning the eruption show that deformation was widespread; complex in-

terferometric fringes span the entire island, with at least five distinct deforming areas (Figure 9).

Time series data reveal further sub-volcanic complexity. The caldera and southern flanks began inflating immediately following the June 2018 eruption of Fernandina, while the northeastern and western flanks show differing displacement patterns in different LOS directions (Figures 10 and 9), until December 2019. At this point, almost all time series points show an uptick in displacement, until January 12th. During the eruption, all time series points show significant ground deformation, though the most notable change occurred in the southwestern sector of the island. The southwestern flank up-

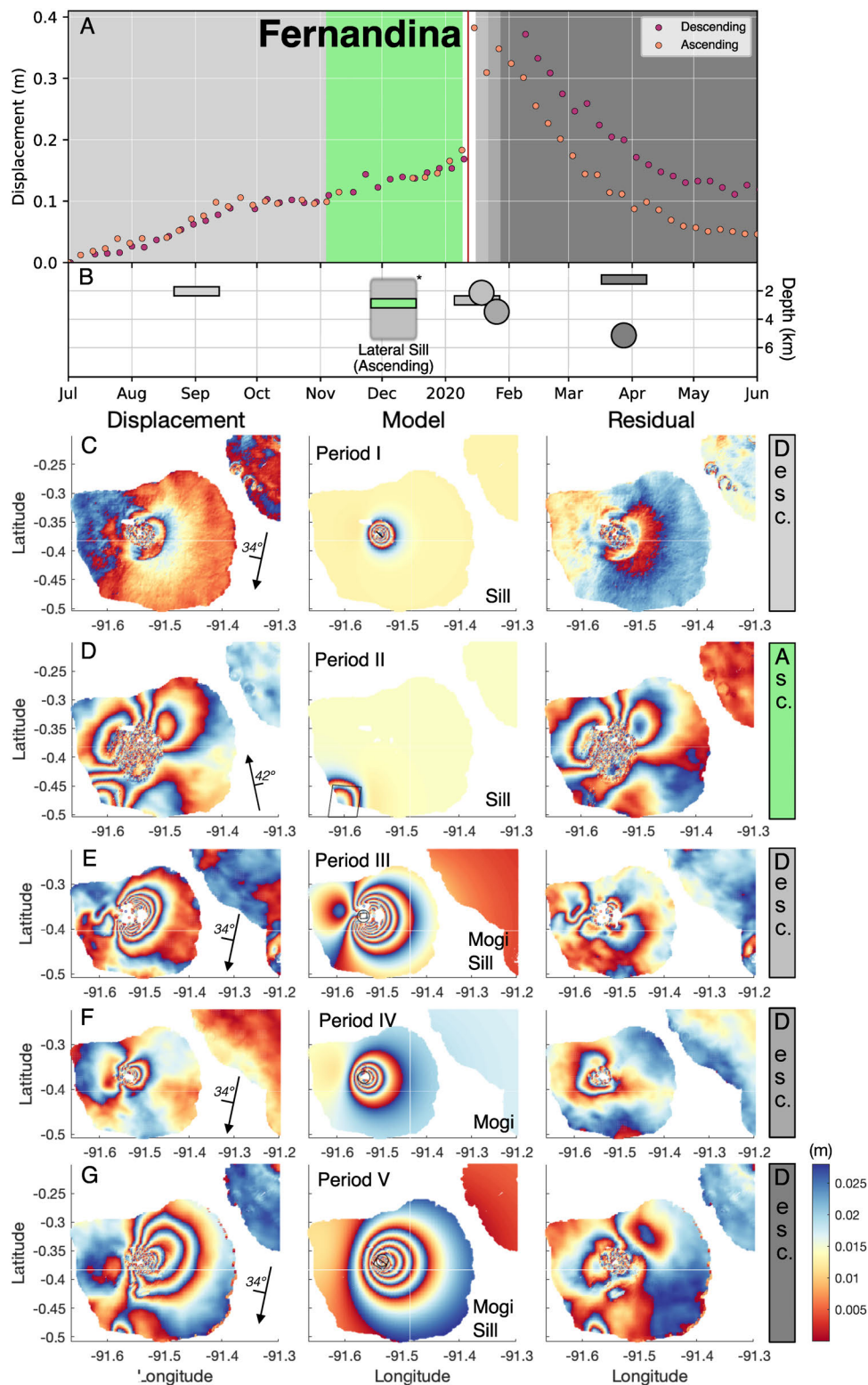


Figure 11: Results of geodetic source modelling for the 2020 eruption of Fernandina. Full results in Tables A11– A17. Inset arrow shows satellite heading and incidence angle. [A] Time Series of displacement in the caldera (e.g. Figure 9C), in both track directions, colour indicates each modelled period. [B] Indicative schematic of the sources active during each period. * denotes sources that were active during the pre-eruptive period, but that are not modelled here. [C] Data, model, and residual for cumulative displacement at Fernandina for a joint inversion, presented using descending data. Black outline illustrates geometry of the modelled source, for Mogi sources, only the x and y co-ordinates are plotted. [D] Pre-eruptive uplift on the southwestern coast, modelled using only ascending data. [E]–[G] Data, model, and residual for cumulative displacement at Fernandina for a joint inversion, presented using descending data. Inset letters refer to track direction.

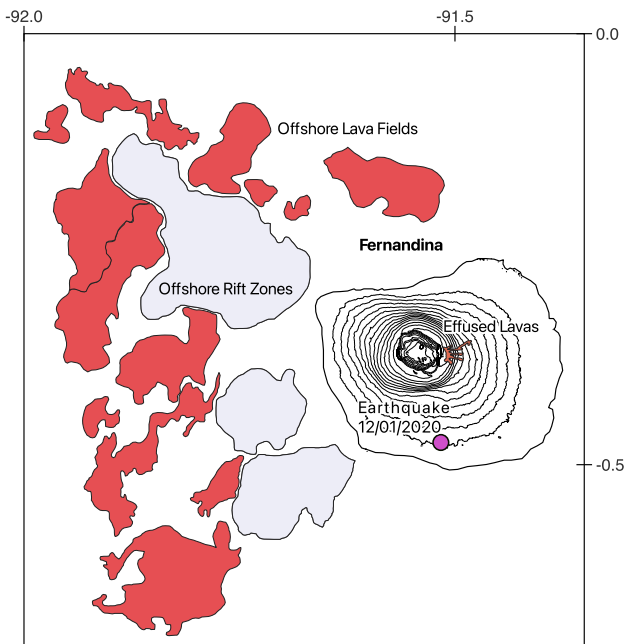


Figure 12: Volcanic context of the 2020 eruption of Fernandina. A magnitude 4.6 earthquake occurred on the southern flank of the volcano on the day of the eruption [U.S. Geological Survey Earthquake Catalogue 2023]. Lavas effused from a circumferential fissure on the eastern caldera rim, covering an area of approximately 3 km^3 . Extensive rift zones (in grey), and lava fields (in red), are located off the west coast of Fernandina Island.

lifted by 0.1–0.15 m between satellite acquisitions surrounding the eruption, while the southwestern coast uplifted by 0.1 m in ascending, and shows complex uplift-subsidence patterns in descending (Figures 9 and 10). In both cases, the fringes of deformation end abruptly at the coast of Fernandina Island, indicating an offshore component to the eruptive unrest. Ground displacement continued for months following the eruption: the caldera, southern flank, and parts of the southwest coast gradually subsided, until June 2020 in both track directions, while the western flank and northeastern flanks continued to deform over this period.

Here, we model the primary features of displacement during the co-eruptive period and identify the main geodetic source regions (Section 3). Bagnardi and Amelung [2012] found that deformation at Fernandina can be explained by a shallow sill overlying a deeper Mogi source. Assuming these sources to be temporally consistent, we model each of the following periods using one or both of these sources. We perform joint inversions using descending and ascending cumulative displacement data leading up to the eruption during periods I–V, as labelled in Table 2.

We find that pre-eruptive inflation (Period I, Figure 11C), is due to opening of the shallow sill (2.1 km, 2.5 %, 97.5 % bounds of [2.1, 2.2] km), by 17 m (bounds of [4.2, 20] m) (Figure 11). This deformation can also be modelled by a Mogi source at 1.7 km depth, inflating by $1.8 \times 10^6 \text{ m}^3$ (Figure A9

and Table A12). The Mogi source fits the data slightly better (reduced χ^2 of 0.65 and 9.45 in ascending and descending, compared to 0.86 and 9.94 for the sill), though the sill geometry is consistent with the results of previous studies [Bagnardi and Amelung 2012]. The ascending track shows highly complex deformation patterns in the immediate pre-eruptive period (Period II, Figure 11). We cannot reliably model the multiple pre-eruptive sources using single or joint inversions, and instead model the southwestern coast uplift, in the ascending direction, to get indicative source parameters (Figure 11). This part of Fernandina island deforms before, during, and after the eruption, and is similar to previous lateral intrusions, sourced from the deeper reservoir at Fernandina [Bagnardi and Amelung 2012]. We consider this a notable component of the 2020 eruption as the spatial deformation pattern is interrupted by the coastline, indicating a potential offshore component of the eruption. We find that in Period II, uplift of the southwestern corner can be explained by a sill at 2.6 km depth (with a lower limit of 5 km, the depth of the deeper source [Bagnardi and Amelung 2012]), opening by 0.1 m (bounds of [0.09, 0.12] m). We also do not model displacement spanning the eruption, given the highly complex deformation patterns (Figure 9 and Figure 10). Following this, we see that post-eruptive displacement, in Period III, is due to the inflation ($2.8 \times 10^7 \text{ m}^3$) of a point source at 2.2 km depth, alongside the closing of a sill (–8.5 m, bounds of [–8.5, –4.4] m) at 2.5 km depth (bounds of [2.4, 2.6] km). The point source (3.1 km, bounds of [3.1, 3.2] km) continued to inflate ($6.5 \times 10^6 \text{ m}^3$) in Period IV. Deformation in the post-eruptive period (Period V) can again be explained by stacked reservoirs, a sill at 700 m depth (bounds of [700, 1200] m) (closing by –0.3 m, bounds of [–1.8, –0.3] m), as well as a point source at 5.4 km depth (bounds of [5.2, 6.9] km) (deflating by $-1.8 \times 10^7 \text{ m}^3$, bounds of [–2.6, –1.7] $\times 10^7 \text{ m}^3$) (Figure 11). However, residual deformation in the ascending track shows an extra source on the northeastern flank, that does not appear in descending (Figure A4), suggesting additional complexity, and sources, in the sub-volcanic system. Modelling this residual, in the ascending track, shows a deflating source at 4.4 km depth (bounds of [4.2, 4.5] km) (Figure A2, Table A18). Over the same period, the southwestern corner continued to deflate, this time modelled as a sill at 1.4 km depth (bounds of [1.35, 1.7] km), closing by –0.1 m (bounds of [–1.5, –0.1]). The full data, model, and residual for each of these models can be found in Figures A3 and A4, while the full description of sources can be found in Tables A11 to A17.

In total, we see that magma accumulated in the shallow sill for at least four months prior to eruption. The uptick in deformation in the month prior to the eruption probably corresponds to heightened magma flux to multiple reservoirs, including one on the southwestern flank, at 5 km depth. The majority of deformation immediately following the eruption (Periods III and IV) can be explained by magma accumulation between 3.1 and 2.2 km depth. Both stacked sources continued to deflate in Period V, while the southwestern coast of the island inflated. This protracted deformation indicates that the sub-volcanic system of Fernandina was active for months following the eruption, to a much greater degree than indicated

Table 2: Dates, tracks, labels, and appendix tables for modelling of 2020 eruption of Fernandina

Label	Track	Date	Appendix table
I	Ascending	01/07/2019–10/11/2019	Table A11
I	Descending	02/07/2019–05/11/2019	Table A11
II	Ascending	10/11/2019–09/01/2020	Table A13
III	Ascending	15/01/2020–21/01/2020	Table A14
III	Descending	16/01/2020–22/01/2020	Table A14
IV	Ascending	21/01/2020–27/01/2020	Table A15
IV	Descending	22/01/2020–28/01/2020	Table A15
V	Ascending	27/01/2020–01/06/2020	Table A16
V	Descending	28/01/2020–02/06/2020	Table A16

by the sub-aerial component. This agrees with seismic data, which shows that seismicity did not return to background levels following the eruption, but continued, with a magnitude 4.2 on January 21st [IGEPN 2020]. Some of the observed deformation can be explained by volume changes in the known sources at Fernandina (Figure 11), though there are at least three new active sources (Figure 9). The instantaneous uplift on the volcano's southern sector on the day of the eruption is consistent with the syn-eruptive opening of a lateral sill (i.e. away from the caldera, and underlying magmatic system), as occurred during the 2018 eruption of Sierra Negra [Davis et al. 2021]. The displacement patterns also show that a portion of the southwestern uplift occurred offshore Fernandina, undetectable by satellite-radar. Bathymetric mapping by Geist et al. [2006b] showed that this region of offshore Fernandina consists of multiple rift zones, opening into lava fields (Figure 12). Therefore, we speculate that the 2020 eruption of Fernandina may have contained a submarine component, where magma migrated laterally from the sub-volcanic reservoir (e.g. Bagnardi and Amelung [2012]), before intruding, or erupting on offshore Fernandina.

4.4 The active hydrothermal system at Alcedo

We observe steady subsidence at Alcedo from 2015–2022 (approximately 14 cm in descending), with a brief period of uplift in 2020 (Figure 13A). Using ascending and descending data, we perform a joint geodetic source inversion to model the cumulative caldera subsidence (Section 3), over an approximately 5 year period from 26/12/2016–01/10/2021 in descending, and 06/01/2017–30/09/2021 in ascending (we do not perform a joint inversion from 2015–2017 as ascending data were not routinely acquired until 2017). The best-fit sill (Table A7) is approximately 3300 m long, 4700 m wide, at a depth of approximately 1900 m, striking at 207°, and closing by –0.1 m over the modelled period (The 2.5 % and 97.5 % intervals for length, width, depth, strike, and opening are 1466 to 3770 m, 4010 to 5185 m, 1665 to 3137 m, 199 to 220°, and –0.4 to –0.1 m, respectively). The input data, modelled source, and residual, are shown in Figure 13B–D for the Descending track, and Figure 13E–G for the Ascending track, alongside the corresponding reduced χ^2 statistic to indicate the goodness-of-fit between the observation and model [e.g. Li et al. 2021]. In both Figure 13B and Figure 13E, there are small fringes of deformation within the subsidence field at Alcedo. This feature

is clear in the residuals (Figure 13D and Figure 13G), and is located in the hydrothermal field at Alcedo.

Though the presence of hydrothermal activity has been noted before (at depths of up to 1000 m [Goff et al. 2000]), this is the first time that displacement here has been detected geodetically. As volatile-bearing magmas crystallise, the residual melt becomes relatively enriched in volatiles, eventually saturating and exsolving in a process known as second boiling [e.g. Caricchi et al. 2014]. The volatiles can migrate towards the surface (e.g. along pre-existing faults) where they can interact with meteoric water, and prompt unrest in the hydrothermal zone, and fumaroles [e.g. Fournier 1999]. These observations suggest that during uplift, deformation at Alcedo is controlled by magma-tectonic interactions between the sill and the intracaldera fault [Bagnardi 2014; Galetto et al. 2019], while the fault acts as a conduit for volatiles and the hydrothermal system during periods of subsidence. There may also be more direct interaction between the magmatic and hydrothermal systems—heat supply during magma intrusion can pressurise overlying hydrothermal systems, and cause phreato-magmatic eruptions (e.g. Agung, 2017 [Bemelmans et al. 2023]). This is a viable mechanism for unrest at Alcedo, given that the most recent event (in 1993) was phreatic, and caused new fumarolic vents to open [Green 1994]. As such, displacement at the hydrothermal field at Alcedo may provide information about future eruptions.

4.5 Cooling related displacements at Sierra Negra

We observe almost 3 m of LOS uplift in descending Sentinel-1 data in the four years following the 2018 eruption (Figure 4), with a corresponding intrusive volume of approximately 1×10^8 m³ [Reddin et al. 2023]. The extreme uplift at Sierra Negra is not just confined to the caldera; the coast on the southern flank of the volcano (near Puerto Villamil) uplifted between 0.5 and 2 m in the late 20th century [Reynolds et al. 1995], while there was a lateral intrusion on the southeastern flank in June 2010, at depths of 5–11 km [Davidge et al. 2017].

There is also high-magnitude deformation on the flanks of Sierra Negra, due to contraction of effused lavas and emplaced sills. Amelung et al. [2000] observed 20 cm of subsidence (1992–1998) due to the contraction of lavas effused on the northern flank of the volcano during the 1979 eruption. Similarly, we observe lava flow subsidence immediately following

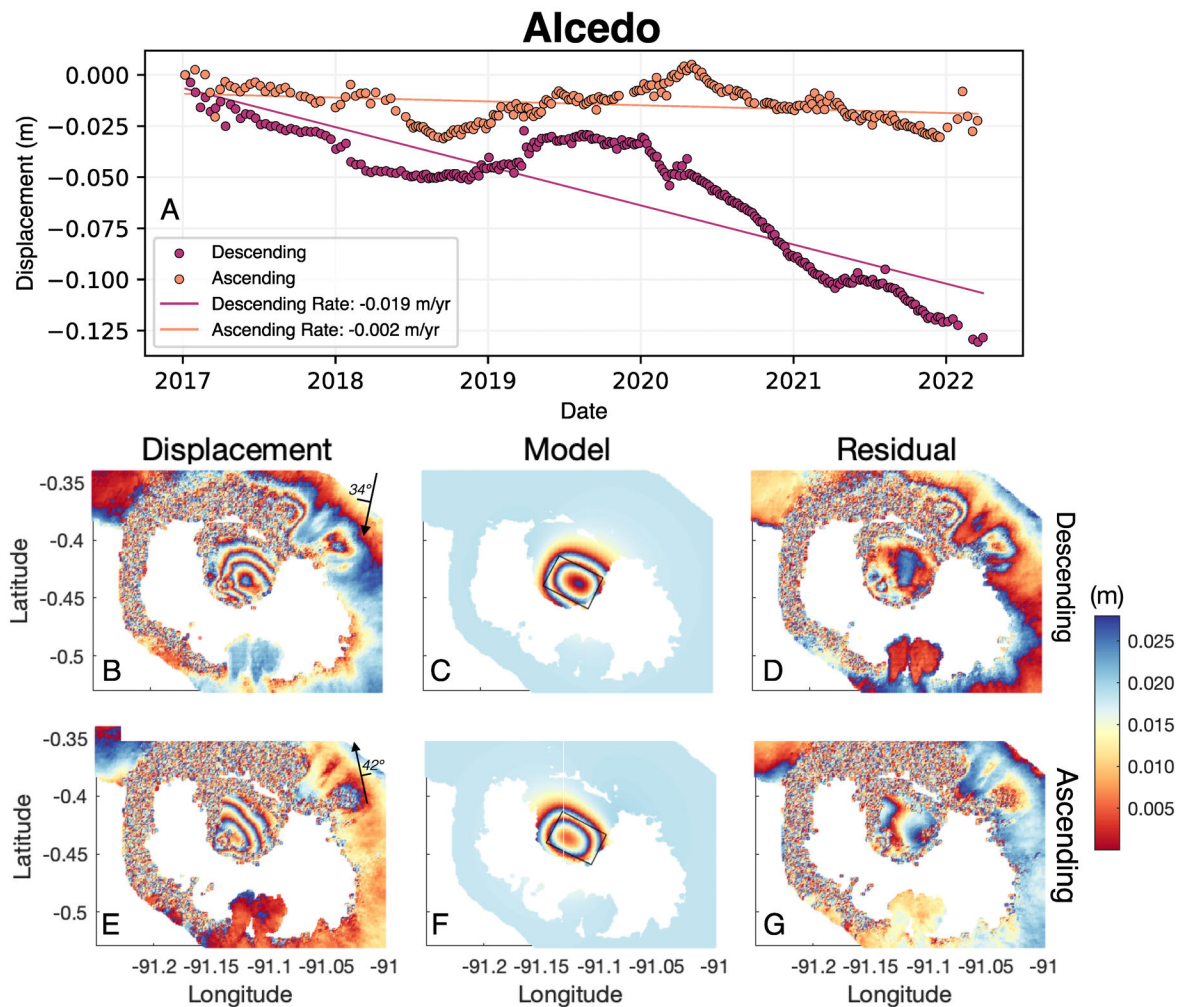


Figure 13: Subsidence at Alcedo from 2017–2022. [A] Time series in both ascending and descending track directions. The point used in the time series is located at -0.438° N, and -91.114° E. This subsidence is relative to a reference area between -0.564 to -0.548° N, and -91.055 to -91.034° E. The difference in magnitude between the descending and ascending tracks is possibly due to horizontal deformation from caldera faulting (e.g. trapdoor faulting at Sierra Negra). [B]–[G] Observed, modelled, and residual displacements, for a contracting sill beneath Alcedo, in descending and ascending track directions, respectively, where each fringe corresponds to 28 mm of LOS displacement. Inset arrow shows satellite heading and incidence angle. Black outline illustrates geometry of the modelled source. Subsidence in the hydrothermal field is clearly visible in panels [B] and [E], and in the residual panels [D] and [G].

their emplacement during the 2018 eruption. We observe that lava flows at the northern, more active fissure had subsided by 20 cm. Lavas emplaced on the upper flank in the 2005 eruption did not appear to subside in the Sentinel-1 era, either because they had cooled fully, or were masked by the uplift of the caldera. The lateral sill [Davis et al. 2021] subsided by 30 cm, exceeding that of the lava flow. This is most likely due to the cooling, crystallisation, and degassing of the intruded magma. Similar to lava flow subsidence, post-intrusive subsidence is observed as a magma cools, vesiculates, and crystallises.

4.6 Long-lived sources at Cerro Azul

Regular radar acquisitions by Sentinel-1 in both track directions began in January 2017, prior to the March unrest

episode. Following this intrusion, caldera-wide uplift resumed at a rate of approximately 5 cm yr^{-1} , and continued until the end of this study (Figure 14), while the uplifted flank (Figure 14) subsided at low rates of between 7 and 12 mm yr^{-1} , possibly due to crystallisation of the intruded magma (Figure A1). Volcanic activity has been concentrated on the eastern flank of Cerro Azul since at least 1979. The 1998 and 2008 eruptions, as well as the 2017 unrest were located on the eastern volcanic flank (Figure 2 and Figure 14). The connection between the sub-caldera source and the eastern flank (the site of fissure eruptions; Figure 14) has probably existed for at least 40 years (given that lavas erupted in 1998 had mixed with residual 1979 magma; Figure 14), and possibly up to 60 years (both the 1979 eruption, and the preceding confirmed eruption in 1959 took place on the eastern flank [Siebert et al. 2010]). This may be due to either a magmatic pathway

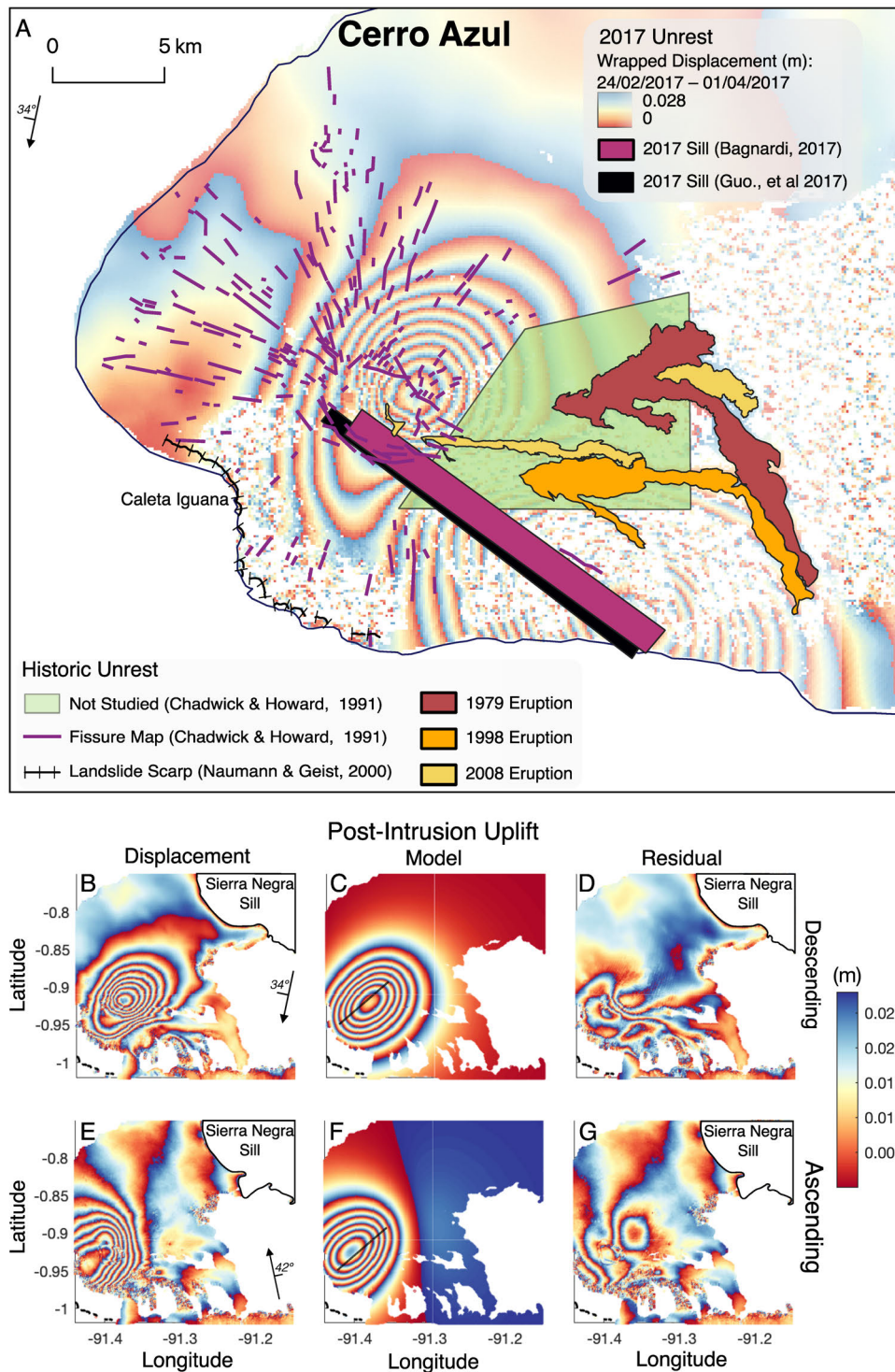


Figure 14: Sources at Cerro Azul. [A] Map of recently active sources, lavas flows, and historical fissures at Cerro Azul. Fissures, as mapped by Chadwick and Howard [1991], are marked in purple, while recent lava flows on the eastern flank are shown in orange. The underlying interferogram spans the 2017 intrusion of Cerro Azul in descending direction, from 24/02/2017–01/04/2017. [B]–[D]. Observed, modelled, and residual displacements, for the best-fit sill for cumulative displacement in the descending track direction from 06/07/2017–24/12/2021. [E]–[G] Observed, modelled, and residual displacements, for the best-fit sill for cumulative displacement in the ascending track direction from 05/07/2017–04/01/2022. The best-fit sill is located at 6300 m depth, 9540 m by 125 m wide, and opened by approximately 24 m. Black outline illustrates geometry of the modelled source. Inset arrow shows satellite heading and incidence angle.

(allowing the mixing of magmas of various ages [Teasdale et al. 2005]), or due to edifice stresses (e.g. Fernandina [Chadwick and Dieterich 1995; Bagnardi et al. 2013]). We perform a joint geodetic source inversion to model the post-unrest cumulative uplift (up to 25 cm) at Cerro Azul, over an approximately five year period from 05/07/2017–04/01/2022 in ascending, and 06/07/2017–24/12/2021 in descending. We start in July 2017 to avoid any syn-unrest displacement. The best-fit sill (Table A8), is approximately 9540 m long, 125 m wide, at a depth of approximately 6300 m, striking at 229°, and opening by 24 m over the modelled period (The 2.5 % and 97.5 % intervals for length, width, depth, strike, and opening are 9350 to 9720 m, 129 to 335 m, 6228 to 6379 m, 228 to 230°, and 9 to 23 m, respectively). The extreme aspect ratio suggests that there may be some trade-off between sill width and opening (e.g. could a wider sill, opening by less, facilitate the same amount of surface displacement?). However, such elongate sills have been observed at Cerro Azul, both during the 2017 unrest (709 m by 7010 m) [Guo et al. 2019], and the 2008 eruption (1019 m by 7569 m) [Galletto et al. 2020]. The input data, modelled source, and residual, are shown in Figure 14B–G. In both track directions, there are features on the displacement field on the upper southwestern flank of Cerro Azul (Figure 14B and Figure 14E), that remain in the residual (Figure 14D and Figure 14G). This feature is also observed in cumulative displacement data spanning the 2008 eruption [Galletto et al. 2020], located on the steepest flanks of Cerro Azul ($< 30^\circ$), an area susceptible to mass wasting [Naumann and Geist 2000]. There is extensive landsliding at the base of the southwestern flank, at Caleta Iguana, where the volcano meets the Galápagos platform [Naumann and Geist 2000] (Figure 14). We therefore attribute this deformation feature to the influence of extreme topography, and mass wasting (e.g. as described at Arenal, Costa Rica [Ebmeier et al. 2014]).

5 DISCUSSION

Here, we use our new post-2015 observations as well as historical deformation measurements to summarise the insights that InSAR provides into sub-volcanic structures at Alcedo, Cerro Azul, Darwin, Fernandina, Sierra Negra, and Wolf. We focus on the evidence for either change or continuation of geodetic sources over the past 30 years and discuss the persistence of characteristics in deformation and eruption at different volcanoes in the context of the magma flux into the western Galápagos and connectivity at the level of melt supply.

At five of these volcanoes, we model the source parameters at various times between 2015 and 2021, and compare with historical observations (Figure 16). We find good agreement with previous models at each volcano, showing that these sources have been active for over 30 years. For each volcano, the modelled range of depths either corresponds with the historical example present in Figure 16, or with previously published values (Tables A1–??).

5.1 Rapid magma flux through shallow reservoirs

The flux of melt that supplies the western Galápagos volcanoes varies through time [Reddin et al. 2023], controlled by a combination of bottom up and top-down processes. We com-

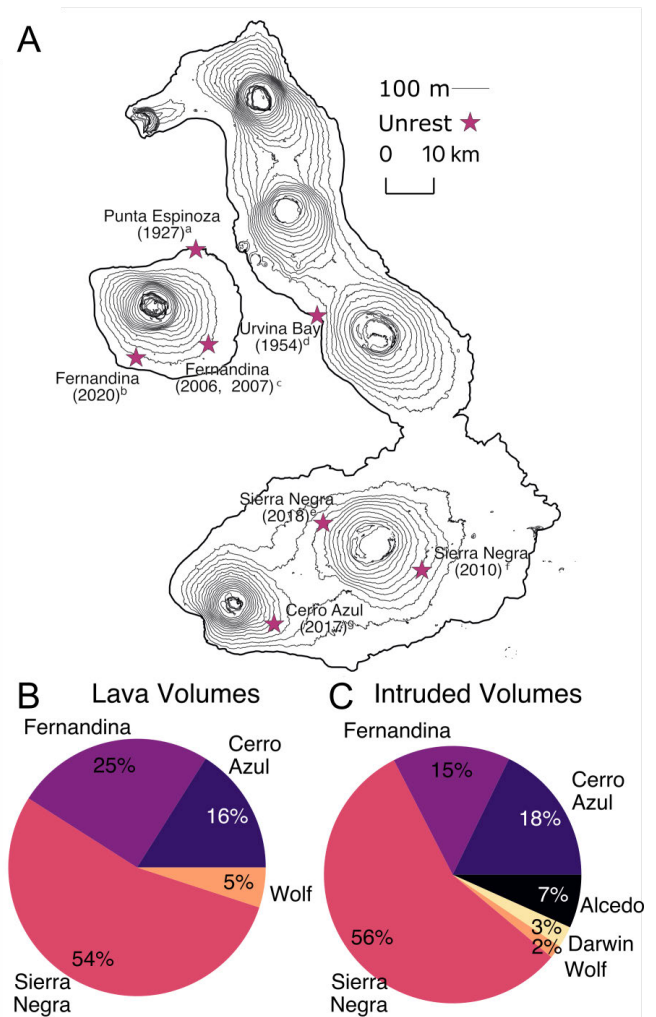


Figure 15: Summary of lateral intrusion and magma flux in the western Galápagos. [A] Map of major lateral intrusions, from the following studies: ^a Cullen et al. [1987], ^b Section 4.3, ^c Bagnardi and Amelung [2012], ^d Nusbaum et al. [1991], ^e Davis et al. [2021], ^f Davidge et al. [2017], ^g Guo et al. [2019]. [B] Pie chart of cumulative effused lava volumes from 1995–2022, as presented in Table A23. [C] Pie chart of cumulative intrusive volumes from 2000–2010 [Bagnardi 2014], and 2017–2022 [Reddin et al. 2023].

pare estimates of intrusive volume change detectable using InSAR, between 2000 and 2010 [Bagnardi 2014] and 2017–2022 [Reddin et al. 2023]. The primary change between these two eras is the decreased melt supply at Alcedo, which accounted for 10 % of total shallow intrusive flux from 2000–2010 (spanning its resurgence), but subsided between 2017 and 2022. Comparing total percentages of intrusive volume fluxes to estimates of extruded lava from 1995–2022 (Figure 2), we see that the proportion of erupted to intruded lavas is consistent, between Sierra Negra (54:56 %), Cerro Azul (16:18 %), and Wolf (5:2 %) (Figure 15). Volcanoes with higher intrusive fluxes also erupted higher volumes of lava, for example, Sierra Negra accounts for more than half of the magma accumulated, and lava erupted, in the western Galápagos (Figure 15). The similar ratios of erupted and intruded volumes also agrees with

the hypothesis that long-term magma storage in the crust is uncommon, but rather magma rapidly cycles through sub-volcanic systems [Geist et al. 2005; Stock et al. 2020].

Stock et al. [2020] demonstrated that during eruptions at both Wolf and Fernandina, primitive basalts flush through the sub-volcanic system at the erupting volcano, overwhelming stored evolved magmas. As a result, these primitive basalts account for the majority of erupted material (> 90 %), at both volcanoes. This is consistent with the geodetic evidence that at Wolf, magma flux into the shallow reservoir is the lowest of any of Wolf, Darwin, Fernandina, Alcedo, Sierra Negra, and Cerro Azul [Bagnardi 2014]. In Section 4.1, we compare these petrological observations to Sentinel-1 data—there is near complete coverage of inter-eruptive inflation at Wolf

from 2015–2022, allowing cumulative intruded magma volumes to be estimated. We find that regardless of source geometry, erupted volumes exceed intruded volumes by almost double. This “missing” intruded volume has been observed at many other volcanoes and attributed variously to data gaps and compressibility of the magma and reservoir [Kilbride et al. 2016]. In the Galápagos, this observation, alongside the absence of a significant pre-eruptive uptick in inflation, adds to evidence for magma flushing consistent with the observations of Stock et al. [2020]. Though there is so far no geodetic evidence of stacked reservoirs at either Darwin or Alcedo, the 1954 uplift at Urvina Bay suggests that a deeper reservoir may be present at at least one of these systems. At Fernandina in 2006 and 2007, and Sierra Negra in 2010, the lateral intrusion was sourced from the deeper magmatic system, (Figure 15) while the 2017 intrusion at Cerro Azul was intruded from a reservoir at 5–6 km below sea level [Bagnardi and Amelung 2012; Davidge et al. 2017; Guo et al. 2019].

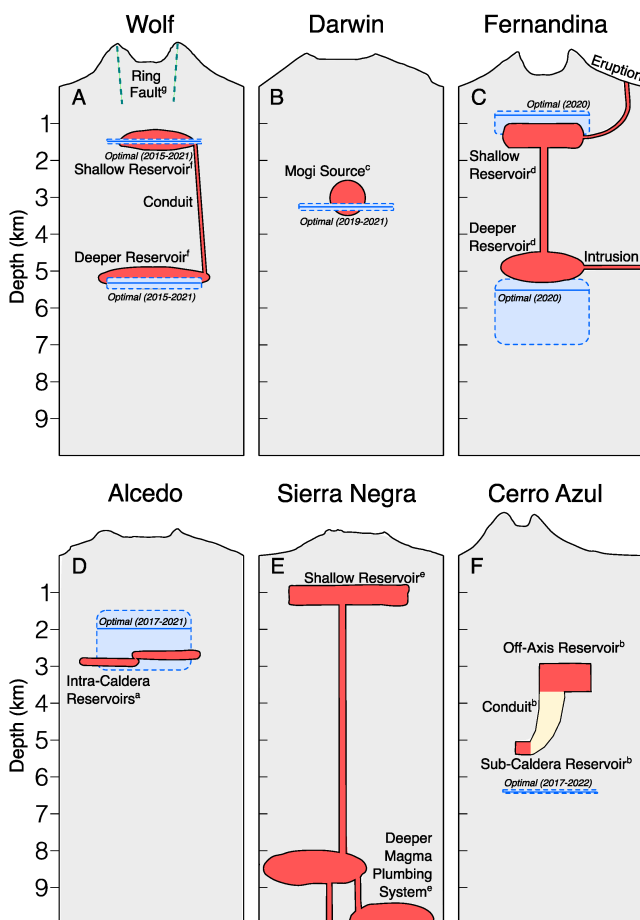


Figure 16: Schematic diagrams illustrating the proposed sub-volcanic structure at each volcano. Panels [A]–[F]. refer to each of Wolf, Darwin, Fernandina, Alcedo, Sierra Negra, and Cerro Azul, respectively. The sub-volcanic structure at Sierra Negra has not been modelled here, and is taken from published studies. The studies from which these schematics are modified from are as follows: ^a Galetto et al. [2019], ^b Galetto et al. [2020], ^c Amelung et al. [2000], ^d Bagnardi and Amelung [2012], ^e Bell et al. [2021b], ^f Xu et al. [2016], ^g Liu et al. [2019]. Results from modelling conducted in this study are presented in blue boxes, with the solid line showing the optimal source depth, and the dotted lines showing the 2.5 % and 97.5 % bounds on depth.

5.1.1 Potential influence of ring faulting

Deformation at western Galápagos volcanoes is controlled by an interplay of top-down structural controls, and bottom-up magmatic activity [Amelung et al. 2000; Galetto et al. 2023]. Every volcano is topped by a summit caldera, and associated structures, while magma is stored at various levels throughout the crust, supplied by the Galápagos plume. Previous studies have indicated stacked magmatic reservoirs at multiple Galápagos volcanoes, both from geodetic [Bagnardi and Amelung 2012] and petrological evidence [Geist et al. 2006b]. Our conceptual model of mature Galápagos volcanoes is of vertically distributed magmatic reservoirs, through which primitive basalts periodically flush. However, we note that source geometries estimated from inversion of surface displacements only capture the fraction of a magmatic zone experiencing volume change and not the full sub-volcanic system. Both Liu et al. [2019] and Xu et al. [2023] showed that deformation patterns at Wolf can be explained by caldera ring faults and a single magmatic reservoir at 4 km [Liu et al. 2019], without invoking stacked reservoirs. While we do not see surface expression of ring fault displacement in our interferograms, there is evidence for major caldera bounding faults at other Galápagos volcanoes [Amelung et al. 2000]. Neglecting slip along these ring faults may lead to overestimation of magmatic volume change by up to 20 % [Liu et al. 2019].

5.2 Classifying western Galápagos volcanoes

The volcanoes of the western Galápagos have previously been classified as “Juvenile,” “Mature,” or “Dying,” based on the range of the magnesium number of erupted lavas (monotonous or diverse), giving an estimate of magma reservoir temperature and sub-volcanic structure (Figure 17) [Geist et al. 2014; Harpp and Geist 2018]. This classification generally reflects the age of the western Galápagos volcanoes, as they move eastwards over the Galápagos plume. The youngest, Cerro Azul, is juvenile, its basalts are simultaneously the most primitive and diverse in the western Galápagos [Harpp and Geist 2018]. The majority of magma storage occurs at around 5 km depth, as the increasing magma supply constructs the sub-volcanic system

[Geist et al. 2014; Harpp and Geist 2018]. Once the magmatic system is established, volcanoes become mature (Fernandina, Darwin, and Wolf), maintaining reservoir temperatures of approximately 1150 °C for thousands of years (Figure 17). Finally, as the older volcanoes are carried away from the plume, magma supply wanes, and cooler more diverse lavas erupt at dying volcanoes (Alcedo and Sierra Negra) (Figure 17). This waning supply means that the system is no longer in a thermal steady-state, and erupts cooler magmas, of less than 1050 °C.

This classification reflect an evolutionary model that western Galápagos volcanoes follow across their lifetime. Fernandina is approximately 32,000 years old [Kurz et al. 2014] and has been the subject of geodetic studies for approximately 30 years, or < 0.1 % of its age. As such, interpreting displacements in the context of their evolutionary classification may be unrepresentative, since the character of activity since geodetic measurements began is ephemeral, compared to the lifespan of the volcano. For example, Sierra Negra is classified as dying from lava Mg#, yet it was supplied the most magma (54 % of the total magma supply) of any Galápagos volcano from 1992–2010, and 2017–2022. Structurally, the shallow caldera at Darwin (Mature) better resembles Alcedo and Sierra Negra (Dying) (Figure 15), than the deep calderas of Fernandina, or Wolf (Mature), which are similar to Cerro Azul (Juvenile) (Figure 5 and Figure 17). While Fernandina and Wolf erupt through a similar mechanism [Stock et al. 2020], Sierra Negra and Alcedo (both Dying) deform very differently, the former with spectacular long-term uplift, and the latter with sustained subsidence as the sub-volcanic sill crystallises. Similarly, Fernandina (Mature) erupted three times between 2010 and 2022 (2017, 2018, 2020), while Darwin (also Mature) last erupted in 1813 [Venzke 2023] (Figure 17). Bearing this in mind, we now consider how deformation patterns at each volcano fits into their evolutionary stage.

5.2.1 Juvenile magmatic system: Cerro Azul

There is no evidence of stacked reservoirs at Cerro Azul; it is more active than Darwin and Alcedo, and is underlain by a magmatic reservoir consistently located at approximately 5–6 km depth (Table A2), as detected during the 2008 eruption [Galletto et al. 2020], 2017 unrest [Guo et al. 2019], and by our modelling from 2017–2021 data (Figure 14). This reservoir acts as a source from which intrusions extend during unrest/eruptions. We propose that there is an established connection from this sill to the east of the volcano—each of the 1998, 2008, and 2017 unrest episodes were located in this part of the volcano. That the 1998 eruption was initially mixed with magma from the 1979 eruption [Teasdale et al. 2005] suggests that this connection has been present since at least 1979. Eruptions have been confined to the eastern flank for at least 60 years since the 1959 event. However, hazards are also present on other flanks, with features in the Sentinel-1 deformation field that may capture mass wasting on the western flank, towards Caleta Iguana. Cerro Azul has a smaller caldera than any other western Galápagos volcano, and while it has a similar shape to Fernandina and Wolf, the differences in its eruptive style, and sub-volcanic architecture distinguish it.

5.2.2 Mature reservoirs: Fernandina and Wolf

Fernandina and Wolf are presently in an extrusively active phase, with eruptions at Fernandina in 2017, 2018, and 2020, and at Wolf in 2015, and 2022. These eruptions alternate between radial and circumferential [Bagnardi et al. 2013], sourced from stacked reservoirs at approximately 1 km and 5 km [e.g. Bagnardi and Amelung 2012; Xu et al. 2016]. Mature magmatic systems in the western Galápagos have developed vertically extensive magmatic zones, with storage at multiple depths through which primitive basalts frequently flush. Fissure and intrusion geometries are strongly influence by local stress fields and potentially faulting within the calderas (Figure 15 and Figure 16).

Fernandina is the most active volcano in the Galápagos, and overlies reservoirs between 1 and 5 km depth. These reservoirs drive the near-constant ground deformation at Fernandina [Jónsson et al. 1999; Amelung et al. 2000; Geist et al. 2006a; Chadwick et al. 2011; Baker 2012; Bagnardi et al. 2013; Bagnardi 2014; Pepe et al. 2017; Chandni and Kumar 2020], and show a high degree of magma mobility during eruptions (2005, 2009, 2017, and 2018 [Bagnardi and Amelung 2012; Galletto et al. 2023]). Bagnardi and Amelung [2012] showed that the shallower of these reservoirs acts as a source for fissure eruptions, while the deeper acts as a source for lateral intrusions. These lateral intrusions have been detected at Fernandina, in December 2006, and August 2007 [Bagnardi and Amelung 2012]; likewise, there are historical anecdotal accounts of these deep sourced lateral intrusions: Punta Espinoza, on the NW flank of Fernandina uplifted in 1927 (Figure 15), during which a fishing boat was stranded as the ground uplifted by “several feet,” and was accompanied by “violent bubbling” of seawater [Cullen et al. 1987]. We also observe lateral magma migration during the 2020 eruption of Fernandina. In terms of erupted volume, this was the smallest eruption to have occurred at Fernandina between 1992 and 2023. However, it was accompanied by major ground deformation, the westward migration of magma, and the opening of a sill off the southwest coast. We speculate that these may have resulted in an offshore eruption into the volcano’s submarine rift zones and lava fields.

Like Fernandina, Wolf overlies reservoirs at approximately 1 km depth [Xu et al. 2016; De Novellis et al. 2017; Stock et al. 2018], and at 5–6 km depth [Xu et al. 2016; Stock et al. 2018] through which magma flushes through during eruptions. Deformation may also be due to a single source, interacting with caldera ring faults. Between its 2015 and 2022 eruptions, Wolf was one of the few volcanoes where the entire inter-eruptive cycle was observed. We find that this inter-eruptive inflation is also best-fit by stacked sills at 1.5 and 5.2 km depths. The style of eruptive fissure (radial vs circumferential) alternates between eruptions, and we suggest that like Fernandina, the preceding eruption alters the static stress field for the next eruption. As at Cerro Azul, all recent unrest at Wolf has been concentrated on its southeastern flank. Wolf, unlike Fernandina, has little geodetic evidence that the deeper reservoir acts as a source for lateral intrusions, though its remote location and lack of ground-based monitoring may mean that such intrusions have not been detected—the presence of offshore rift

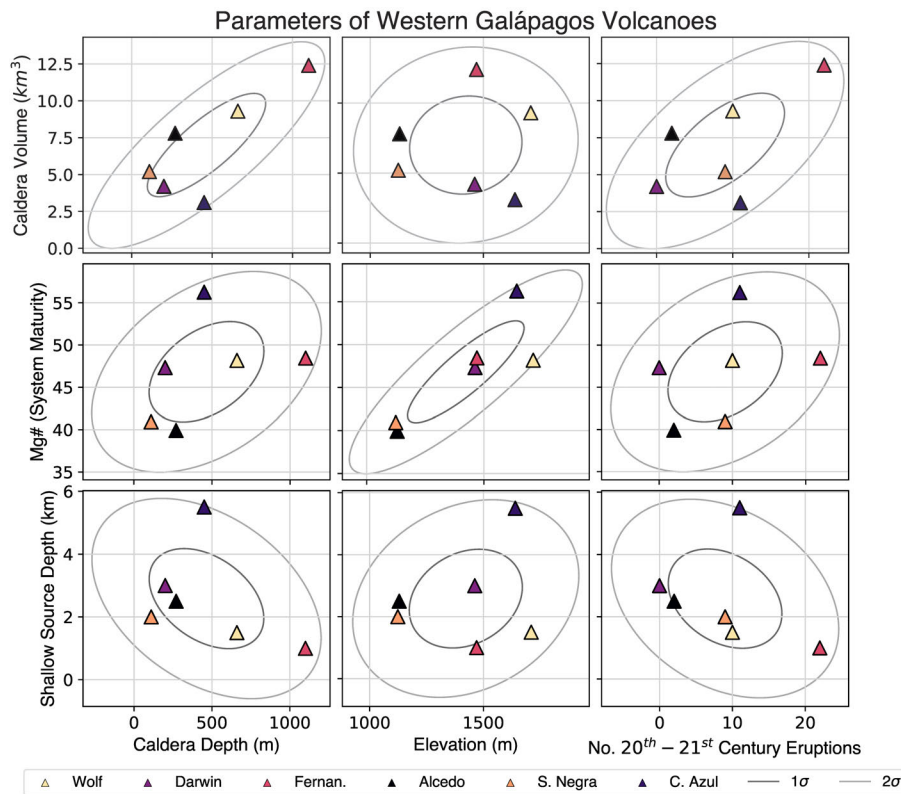


Figure 17: Characteristic parameters of western Galápagos volcanoes. In each plot, a set of key parameters are plotted against one another, from caldera volume, magnesium number, shallow source depth, caldera depth, elevation, and the number of eruptions since the 20th century. The ellipses represent the confidence ellipses for the first and second standard deviations of each dataset.

zones [Geist et al. 2006b] may indicate lateral magma migration from Wolf.

Based on this, we suggest a magmatic zone structure with storage at multiple depths through which primitive basaltic magmas routinely flush, where local stress field may control the eruptive geometry, may be typical characteristics of mature western Galápagos volcanoes.

5.2.3 Dying activity: Alcedo, Darwin, and Sierra Negra

Deformation patterns at Alcedo are complex, but have been consistently attributed to either inflation (2007–2011) or deflation (2017–2022) of a magma body located between 2 and 3 km depth (point, sill, CDM, and pipe-like sources (e.g. Galetto et al. [2019] in Table A1), indicative of an established reservoir at this depth. Modelling deformation at Alcedo has generally required either contributions from an intra-caldera fault [Bagnardi 2014; Galetto et al. 2019] or a pipe-like geometry [Hooper et al. 2007]. Faulting seems to dominate displacements during periods of magmatic influx, and may act as a conduit for magma-derived fluids to reach the surface fumarole field. In Section 4.4, we observe subsidence at this fumarole field, which overprinted the subsidence due to the cooling of a sill from 2017–2022.

Though the Mg# of magmas at Darwin is similar to that of mature volcanoes (Figure 17), the observed characteristics are closer to that of dying volcanoes. Darwin is extrusively quiescent, there is clearly active magma supply to the vol-

cano (e.g. Bagnardi [2014]), and it undergoes periodic uplift (e.g. Amelung et al. [2000], Figure 8). Both this study and the few previous deformation studies at Darwin find a geodetic source at around 3 km depth beneath the volcano, with lower depth estimates of 2.7 km, and higher estimates of 4.25 km (Table A3). Why then, despite active magma supply, does Darwin erupt so infrequently? It is possible that the supplied volumes are either insufficient or irregular enough to cause an eruption. However, it is also possible that due to its current quiescence, historical eruptions have not been identified. There is some historical evidence of lateral intrusions near Darwin: Urvina Bay “catastrophically uplifted” by 6 m in 1954, exposing 1.4 km² of coral reef [Nusbaum et al. 1991] (Figure 15). The magmatic source of this uplift is unclear; Urvina Bay is closer to Alcedo than Darwin, but uplift there revealed Darwin-derived basalts, though McBirney et al. [1985] hint that it may be related to a 1954 lava flow at Alcedo.

Therefore, despite its mature geochemistry, unrest behaviour at Darwin is more in line with that at dying volcanoes. Both Alcedo and Darwin maintain shallow magma reservoirs between 2 and 3 km depth (Figure 16). Significant unrest is uncommon at either volcano, though both periodically experience episodes of resurgence (Figure 8, Galetto et al. [2019]). Eruptions are also rare—Darwin last erupted in 1813 [Venzke 2023], and Alcedo’s last eruption was in 1953—the 1993 event was a phreatic explosion, rather than an effusive eruption typical of western Galápagos volcanoes [Green 1994].

Sierra Negra, like Darwin, is another example of a western Galápagos volcano that behaves distinctly from those in its evolutionary dying classification. While the magmatic system beneath Sierra Negra has reached a state of maturity and fits in this respect into the “Dying” classification, current and recent historical activity suggests that it receives the highest melt flux in the Galápagos. Like Fernandina and Wolf, Sierra Negra has a stacked magmatic system between 2 and 8 km depth [Tepp et al. 2014; Bell et al. 2021b]. Extreme uplift at Sierra Negra is driven by magma accumulation in the shallow reservoir, at rates of between $1.06 \times 10^7 \text{ m}^3 \text{ yr}^{-1}$ [Bagnardi 2014] and $1.3 \times 10^7 \text{ m}^3 \text{ yr}^{-1}$ [Aiuppa et al. 2022]. Interaction between this reservoir and the trapdoor fault characterise volcanism here, causing asymmetric deformation patterns, controlling eruption location, and facilitating the vigorous hydrothermal system. The cooling and crystallisation of lateral intrusions (Figure 15), and lava flow contraction drive subsidence at the sites of recent eruption. It has experienced sustained long-term uplift—like Wolf—as well as sustained subsidence (between 2000 and 2004) like Alcedo. The shape of Sierra Negra volcano is similar to Alcedo and Darwin (Figure 17), though it is likewise distinct from these volcanoes due to its extreme uplift.

6 CONCLUSIONS

Volcanic activity and magma storage locations at the western Galápagos islands of Fernandina and Isabela have been remarkably consistent for at least three decades. We show this by synthesising published literature and historical InSAR observations, and comparing with new Sentinel-1 imagery from 2015–2022. We demonstrate that Alcedo has two discrete zones of subsidence, one magmatic and one hydrothermal; Cerro Azul has had eruptions and unrest concentrated on the eastern flank of the volcano for at least 30 years; Darwin has resurged, like Alcedo, but shows no evidence of hydrothermal emissions or subsidence; Fernandina rapidly inflates and deflates more than any other volcano, and may have had a submarine eruption in 2020; Sierra Negra uplifts by extreme magnitudes for sustained periods, and there is evidence of volcanic deformation on its flanks as well as its caldera; Wolf uplifts by low magnitudes for sustained periods, and magma rapidly flushes through there during eruption. In the western Galápagos, deformation relates to sub-volcanic magmatic zone maturity but is modified by the influence of caldera faulting and especially by highly variable melt supply rates to produce characteristic deformation behaviours at each volcanic that have persisted over decades.

AUTHOR CONTRIBUTIONS

E.R. synthesised and compiled the information about each volcano. He also constructed new time series of deformation, and performed the analysis of new data presented at each volcano. S.K.E. contributed to the writing of the paper, and steered the direction of the analysis. P.E.B., M.B., and A.F.B. provided expert guidance throughout.

ACKNOWLEDGEMENTS

We would like to thank Dr Milan Lazecky for his assistance when filling missing data in the LiCSAR system, as well as Santiago Aguaiza for sharing knowledge on lava flow volumes. We also thank reviewers of the manuscript, and Dr Tyler Paladino for excellent feedback. E.Red. was supported by a European Space Agency Living Planet Fellowship originally awarded to S.K.E.; S.K.E. was supported by a NERC Independent Research Fellowship (NE/R015546/1); A.B. was supported by a NSFGE0-NEC grant on Sierra Negra NE/W007274/1 and the FRIGATE NERC urgency project NE/X016986/1. Any use of trade, firm, or product names is for descriptive purposes only and does not imply endorsement by the U.S. Government.

DATA AVAILABILITY

The European Space Agency has copyrighted Sentinel-1 InSAR data, which are freely accessible through both the Alaska Satellite Facility (<https://asf.alaska.edu/>) and the Copernicus Open Access Hub (<https://scihub.copernicus.eu/>). The Synthetic Aperture Radar data used in this study were processed using the LiCSAR interferometric processor and are freely distributed on the COMET-LiCS Sentinel-1 InSAR portal (<https://comet.nerc.ac.uk/COMET-LiCS-portal/>). The GACOS atmospheric correction data can be found at (<http://www.gacos.net>), while the LiCSBAS time series used to construct deformation time series can be accessed through Morishita et al. [2020]. Both the LiCSBAS output .h5 files, and time series used throughout this study are available at <https://doi.org/10.5281/zenodo.10849601>.

COPYRIGHT NOTICE

© The Author(s) 2024. This article is distributed under the terms of the **Creative Commons Attribution 4.0 International License**, which permits unrestricted use, distribution, and reproduction in any medium, provided you give appropriate credit to the original author(s) and the source, provide a link to the Creative Commons license, and indicate if changes were made.

REFERENCES

- Aiuppa, A., P. Allard, B. Bernard, F. M. Lo Forte, R. Moretti, and S. Hidalgo (2022). “Gas Leakage From Shallow Ponding Magma and Trapdoor Faulting at Sierra Negra Volcano (Isabela Island, Galápagos)”. *Geochemistry, Geophysics, Geosystems* 23(2). DOI: [10.1029/2021GC010288](https://doi.org/10.1029/2021GC010288).
- Amelung, F., S. Jónsson, H. Zebker, and P. Segall (2000). “Widespread uplift and ‘trapdoor’ faulting on Galápagos volcanoes observed with radar interferometry”. *Nature* 407(6807), pages 993–996. DOI: [10.1038/35039604](https://doi.org/10.1038/35039604).
- Bagnardi, M. (2014). “Dynamics of Magma Supply, Storage and Migration at Basaltic Volcanoes: Geophysical Studies of the Galápagos and Hawaiian Volcanoes”. PhD thesis. Coral Gables, Florida: University of Miami.

- (2017). *Intrusive Activity at Cerro Azul Volcano, Galápagos Islands (Ecuador)*. Technical report 01. University of Leeds: COMET.
- Bagnardi, M. and F. Amelung (2012). “Space-geodetic evidence for multiple magma reservoirs and subvolcanic lateral intrusions at Fernandina Volcano, Galápagos Islands”. *Journal of Geophysical Research: Solid Earth* 117(B10). DOI: [10.1029/2012JB009465](https://doi.org/10.1029/2012JB009465).
- Bagnardi, M., F. Amelung, and M. P. Poland (2013). “A new model for the growth of basaltic shields based on deformation of Fernandina volcano, Galápagos Islands”. *Earth and Planetary Science Letters* 377–378, pages 358–366. DOI: [10.1016/j.epsl.2013.07.016](https://doi.org/10.1016/j.epsl.2013.07.016).
- Bagnardi, M. and A. Hooper (2018). “Inversion of Surface Deformation Data for Rapid Estimates of Source Parameters and Uncertainties: A Bayesian Approach”. *Geochemistry, Geophysics, Geosystems* 19(7), pages 2194–2211. DOI: [10.1029/2018GC007585](https://doi.org/10.1029/2018GC007585).
- Baker, M. S. (2012). “Investigating the Dynamics of Basaltic Volcano Magmatic Systems with Space Geodesy”. PhD thesis. Coral Gables, Florida: University of Miami.
- Banfield, A. F., C. H. Behre, and D. S. Clair (1956). “Geology of Isabela (Albemarle) Island, Archipelago de Colon (Galapagos)”. *Geological Society of America Bulletin* 67(2), pages 215–234.
- Bell, A. F., S. Hernandez, J. McCloskey, M. Ruiz, P. C. LaFemina, C. J. Bean, and M. Möllhoff (2021a). “Dynamic earthquake triggering response tracks evolving unrest at Sierra Negra volcano, Galápagos Islands”. *Science Advances* 7(39), eabh0894. DOI: [10.1126/sciadv.abh0894](https://doi.org/10.1126/sciadv.abh0894).
- Bell, A. F., P. C. La Femina, M. Ruiz, F. Amelung, M. Bagnardi, C. J. Bean, B. Bernard, C. Ebinger, M. Gleeson, J. Grannell, S. Hernandez, M. Higgins, C. Liorzou, P. Lundgren, N. J. Meier, M. Möllhoff, S.-J. Oliva, A. G. Ruiz, and M. J. Stock (2021b). “Caldera resurgence during the 2018 eruption of Sierra Negra volcano, Galápagos Islands”. *Nature Communications* 12(1), page 1397. DOI: [10.1038/s41467-021-21596-4](https://doi.org/10.1038/s41467-021-21596-4).
- Bemelmans, M. J. W., J. Biggs, M. Poland, J. Wookey, S. K. Ebmeier, A. K. Diefenbach, and D. Syahbana (2023). “High-Resolution InSAR Reveals Localized Pre-Eruptive Deformation Inside the Crater of Agung Volcano, Indonesia”. *Journal of Geophysical Research: Solid Earth* 128(5), e2022JB025669. DOI: [10.1029/2022JB025669](https://doi.org/10.1029/2022JB025669).
- Bernard, B. (2022). “Volcanic event management in the Galápagos Islands, Ecuador”. 5, page 17.
- Bernard, B., M. J. Stock, D. Coppola, S. Hidalgo, M. Bagnardi, S. Gibson, S. Hernandez, P. Ramón, and M. Gleeson (2019). “Chronology and phenomenology of the 1982 and 2015 Wolf volcano eruptions, Galápagos Archipelago”. *Journal of Volcanology and Geothermal Research* 374, pages 26–38. DOI: [10.1016/j.jvolgeores.2019.02.013](https://doi.org/10.1016/j.jvolgeores.2019.02.013).
- Caricchi, L., J. Biggs, C. Annen, and S. Ebmeier (2014). “The influence of cooling, crystallisation and re-melting on the interpretation of geodetic signals in volcanic systems”. *Earth and Planetary Science Letters* 388, pages 166–174. DOI: [10.1016/j.epsl.2013.12.002](https://doi.org/10.1016/j.epsl.2013.12.002).
- Chadwick, W. and J. Dieterich (1995). “Mechanical modeling of circumferential and radial dike intrusion on Galapagos volcanoes”. *Journal of Volcanology and Geothermal Research* 66(1–4), pages 37–52. DOI: [10.1016/0377-0273\(94\)00060-T](https://doi.org/10.1016/0377-0273(94)00060-T).
- Chadwick, W. W. and K. A. Howard (1991). “The pattern of circumferential and radial eruptive fissures on the volcanoes of Fernandina and Isabela islands, Galapagos”. *Bulletin of Volcanology* 53(4), pages 259–275. DOI: [10.1007/BF00414523](https://doi.org/10.1007/BF00414523).
- Chadwick, W. W., D. J. Geist, S. Jónsson, M. Poland, D. J. Johnson, and C. M. Meertens (2006). “A volcano bursting at the seams: Inflation, faulting, and eruption at Sierra Negra volcano, Galápagos”. *Geology* 34(12), page 1025. DOI: [10.1130/G22826A.1](https://doi.org/10.1130/G22826A.1).
- Chadwick, W. W., S. Jónsson, D. J. Geist, M. Poland, D. J. Johnson, S. Batt, K. S. Harpp, and A. Ruiz (2011). “The May 2005 eruption of Fernandina volcano, Galápagos: The first circumferential dike intrusion observed by GPS and InSAR”. *Bulletin of Volcanology* 73(6), pages 679–697. DOI: [10.1007/s00445-010-0433-0](https://doi.org/10.1007/s00445-010-0433-0).
- Chandni, C. K. and S. Kumar (2020). “DInSAR based Analysis of January 2020 Eruption of Fernandina Volcano, Galapagos”. *2020 IEEE India Geoscience and Remote Sensing Symposium (InGARSS)*. Ahmedabad, India: IEEE, pages 250–253. ISBN: 978-1-72813-114-6. DOI: [10.1109/InGARSS48198.2020.9358954](https://doi.org/10.1109/InGARSS48198.2020.9358954).
- Chestler, S. R. and E. B. Grosfils (2013). “Using numerical modeling to explore the origin of intrusion patterns on Fernandina volcano, Galapagos Islands, Ecuador”. *Geophysical Research Letters* 40(17), pages 4565–4569. DOI: [10.1002/grl.50833](https://doi.org/10.1002/grl.50833).
- Corbi, F., E. Rivalta, V. Pinel, F. Maccaferri, M. Bagnardi, and V. Acocella (2015). “How caldera collapse shapes the shallow emplacement and transfer of magma in active volcanoes”. *Earth and Planetary Science Letters* 431, pages 287–293. DOI: [10.1016/j.epsl.2015.09.028](https://doi.org/10.1016/j.epsl.2015.09.028).
- Cullen, A. B., A. R. McBirney, and R. D. Rogers (1987). “Structural controls on the morphology of Galapagos shields”. *Journal of Volcanology and Geothermal Research* 34(1–2), pages 143–151. DOI: [10.1016/0377-0273\(87\)90099-0](https://doi.org/10.1016/0377-0273(87)90099-0).
- Davidge, L., C. Ebinger, M. Ruiz, G. Tepp, F. Amelung, D. Geist, D. Coté, and J. Anzieta (2017). “Seismicity patterns during a period of inflation at Sierra Negra volcano, Galápagos Ocean Island Chain”. *Earth and Planetary Science Letters* 462, pages 169–179. DOI: [10.1016/j.epsl.2016.12.021](https://doi.org/10.1016/j.epsl.2016.12.021).
- Davis, T., M. Bagnardi, P. Lundgren, and E. Rivalta (2021). “Extreme Curvature of Shallow Magma Pathways Controlled by Competing Stresses: Insights From the 2018 Sierra Negra Eruption”. *Geophysical Research Letters* 48(13). DOI: [10.1029/2021GL093038](https://doi.org/10.1029/2021GL093038).
- De Novellis, V., R. Castaldo, C. De Luca, S. Pepe, I. Zinno, F. Casu, R. Lanari, and G. Solaro (2017). “Source modelling of the 2015 Wolf volcano (Galápagos) eruption inferred from Sentinel 1-A DInSAR deformation maps and pre-eruptive ENVISAT time series”. *Journal of Volcanology and Geothermal Research* 344, pages 246–256. DOI: [10.1016/j.jvolgeores.2017.05.013](https://doi.org/10.1016/j.jvolgeores.2017.05.013).

- De Roy, T. (2010). *Galapagos: Islands Born of Fire*. 10th anniversary edition. Princeton, New Jersey: Princeton University Press. ISBN: 978-0-691-14637-9.
- Ebmeier, S. K., J. Biggs, C. Muller, and G. Avarad (2014). “Thin-skinned mass-wasting responsible for widespread deformation at Arenal volcano”. *Frontiers in Earth Science* 2. DOI: [10.3389/feart.2014.00035](https://doi.org/10.3389/feart.2014.00035).
- Filson, J., T. Simkin, and L.-k. Leu (1973). “Seismicity of a caldera collapse: Galapagos Islands 1968”. *Journal of Geophysical Research* 78(35), pages 8591–8622. DOI: [10.1029/JB078i035p08591](https://doi.org/10.1029/JB078i035p08591).
- Fournier, R. O. (1999). “Hydrothermal processes related to movement of fluid from plastic into brittle rock in the magmatic-epithermal environment”. *Economic Geology* 94(8), pages 1193–1211. DOI: [10.2113/gsecongeo.94.8.1193](https://doi.org/10.2113/gsecongeo.94.8.1193).
- Gaddes, M. E., A. Hooper, and M. Bagnardi (2019). “Using Machine Learning to Automatically Detect Volcanic Unrest in a Time Series of Interferograms”. *Journal of Geophysical Research: Solid Earth* 124(11), pages 12304–12322. DOI: [10.1029/2019JB017519](https://doi.org/10.1029/2019JB017519).
- Galetto, F., M. Bagnardi, V. Acocella, and A. Hooper (2019). “Noneruptive Unrest at the Caldera of Alcedo Volcano (Galápagos Islands) Revealed by InSAR Data and Geodetic Modeling”. *Journal of Geophysical Research: Solid Earth* 124(4), pages 3365–3381. DOI: [10.1029/2018JB017103](https://doi.org/10.1029/2018JB017103).
- Galetto, F., A. Hooper, M. Bagnardi, and V. Acocella (2020). “The 2008 Eruptive Unrest at Cerro Azul Volcano (Galápagos) Revealed by InSAR Data and a Novel Method for Geodetic Modelling”. *Journal of Geophysical Research: Solid Earth* 125(2). DOI: [10.1029/2019JB018521](https://doi.org/10.1029/2019JB018521).
- Galetto, F., D. Reale, E. Sansosti, and V. Acocella (2023). “Implications for Shallow Magma Transfer During the 2017 and 2018 Eruptions at Fernandina (Galápagos) Inferred From InSAR Data”. *Journal of Geophysical Research: Solid Earth* 128(6), e2022JB026174. DOI: [10.1029/2022JB026174](https://doi.org/10.1029/2022JB026174).
- Geist, D., W. Chadwick, and D. Johnson (2006a). “Results from new GPS and gravity monitoring networks at Fernandina and Sierra Negra Volcanoes, Galápagos, 2000–2002”. *Journal of Volcanology and Geothermal Research* 150(1–3), pages 79–97. DOI: [10.1016/j.jvolgeores.2005.07.003](https://doi.org/10.1016/j.jvolgeores.2005.07.003).
- Geist, D., K. A. Howard, A. M. Jellinek, and S. Rayder (1994). “The volcanic history of Volcán Alcedo, Galápagos Archipelago: A case study of rhyolitic oceanic volcanism”. *Bulletin of Volcanology* 56, pages 243–260.
- Geist, D. J., G. Bergantz, and W. W. Chadwick (2014). “Galápagos Magma Chambers”. *Geophysical Monograph Series*. Edited by K. S. Harpp, E. Mittelstaedt, N. d’Ozouville, and D. W. Graham. Hoboken, New Jersey: John Wiley & Sons, Inc, pages 55–69. ISBN: 978-1-118-85253-8. DOI: [10.1002/9781118852538.ch5](https://doi.org/10.1002/9781118852538.ch5).
- Geist, D. J., D. J. Fornari, M. D. Kurz, K. S. Harpp, S. Adam Soule, M. R. Perfit, and A. M. Koleszar (2006b). “Submarine Fernandina: Magmatism at the leading edge of the Galápagos hot spot”. *Geochemistry, Geophysics, Geosystems* 7(12), n/a–n/a. DOI: [10.1029/2006GC001290](https://doi.org/10.1029/2006GC001290).
- Geist, D. J., K. S. Harpp, T. R. Naumann, M. Poland, W. W. Chadwick, M. Hall, and E. Rader (2008). “The 2005 eruption of Sierra Negra volcano, Galápagos, Ecuador”. *Bulletin of Volcanology* 70(6), pages 655–673. DOI: [10.1007/s00445-007-0160-3](https://doi.org/10.1007/s00445-007-0160-3).
- Geist, D. J., T. R. Naumann, J. J. Standish, M. D. Kurz, K. S. Harpp, W. M. White, and D. J. Fornari (2005). “Wolf Volcano, Galápagos Archipelago: Melting and Magmatic Evolution at the Margins of a Mantle Plume”. *Journal of Petrology* 46(11), pages 2197–2224. DOI: [10.1093/petrology/egi052](https://doi.org/10.1093/petrology/egi052).
- Goff, F., G. M. McMurtry, D. Counce, J. A. Simac, A. R. Roldán-Manzo, and D. R. Hilton (2000). “Contrasting hydrothermal activity at Sierra Negra and Alcedo volcanoes, Galapagos Archipelago, Ecuador”. *Bulletin of Volcanology* 62(1), pages 34–52. DOI: [10.1007/s004450050289](https://doi.org/10.1007/s004450050289).
- Green, J. R. (1994). “Recent activity in Alcedo Volcano, Isabela Island”. *Noticias De Galapagos*, page 3.
- Gregg, P. M., H. Le Mével, Y. Zhan, J. Dufek, D. Geist, and W. W. Chadwick (2018). “Stress Triggering of the 2005 Eruption of Sierra Negra Volcano, Galápagos”. *Geophysical Research Letters* 45(24). DOI: [10.1029/2018GL080393](https://doi.org/10.1029/2018GL080393).
- Gregg, P. M., Y. Zhan, F. Amelung, D. Geist, P. Mothes, S. Koric, and Z. Yunjun (2022). “Forecasting mechanical failure and the 26 June 2018 eruption of Sierra Negra Volcano, Galápagos, Ecuador”. *Science Advances* 8(22), eabm4261. DOI: [10.1126/sciadv.abm4261](https://doi.org/10.1126/sciadv.abm4261).
- Guo, Q., C. Xu, Y. Wen, Y. Liu, and G. Xu (2019). “The 2017 Noneruptive Unrest at the Caldera of Cerro Azul Volcano (Galápagos Islands) Revealed by InSAR Observations and Geodetic Modelling”. *Remote Sensing* 11(17), page 1992. DOI: [10.3390/rs11171992](https://doi.org/10.3390/rs11171992).
- Harpp, K. S. and D. J. Geist (2018). “The Evolution of Galápagos Volcanoes: An Alternative Perspective”. *Frontiers in Earth Science* 6, page 50. DOI: [10.3389/feart.2018.00050](https://doi.org/10.3389/feart.2018.00050).
- Hooper, A., P. Segall, and H. Zebker (2007). “Persistent scatterer interferometric synthetic aperture radar for crustal deformation analysis, with application to Volcán Alcedo, Galápagos”. *Journal of Geophysical Research* 112(B7), B07407. DOI: [10.1029/2006JB004763](https://doi.org/10.1029/2006JB004763).
- Instituto Geofísico Escuela Politécnica Nacional (IGEPN) (2017a). *Cerro Azul Special Report No. 1 - 2017*. Special 01. Campus “Ing. José Rubén Orellana”, Facultad de Ingeniería Civil 6to. Piso. Av. Ladrón de Guevara E11-253: Instituto Geofísico Escuela Politécnica Nacional.
- (2017b). *Cerro Azul Special Report No. 2 - 2017*. Special 02. Campus “Ing. José Rubén Orellana”, Facultad de Ingeniería Civil 6to. Piso. Av. Ladrón de Guevara E11-253: Instituto Geofísico Escuela Politécnica Nacional.
- (2017c). *Cerro Azul Special Report No. 3 - 2017*. Special 02. Campus “Ing. José Rubén Orellana”, Facultad de Ingeniería Civil 6to. Piso. Av. Ladrón de Guevara E11-253: Instituto Geofísico Escuela Politécnica Nacional.
- (2017d). *Special Report of Fernandina Volcano No. 2 - 2017*. Special 02. Campus “Ing. José Rubén Orellana”, Facultad de Ingeniería Civil 6to. Piso. Av. Ladrón de Guevara E11-253: Instituto Geofísico Escuela Politécnica Nacional.

- (2020). *Special Volcanic Report - Fernandina - 2020 - No. 3. Special 03.* Campus "Ing. José Rubén Orellana", Facultad de Ingeniería Civil 6to. Piso. Av. Ladrón de Guevara E11-253: Instituto Geofísico Escuela Politécnica Nacional.
- (2021a). *Special Volcanic Report - Fernandina - 2021 - No. 1. Special 01.* Campus "Ing. José Rubén Orellana", Facultad de Ingeniería Civil 6to. Piso. Av. Ladrón de Guevara E11-253: Instituto Geofísico Escuela Politécnica Nacional.
- (2021b). *Special Volcanic Report - Fernandina - 2021 - No. 2. Special 02.* Campus "Ing. José Rubén Orellana", Facultad de Ingeniería Civil 6to. Piso. Av. Ladrón de Guevara E11-253: Instituto Geofísico Escuela Politécnica Nacional.
- (2022a). *Wolf Volcano Special Report No. 1 - 2022. Special 01.* Campus "Ing. José Rubén Orellana", Facultad de Ingeniería Civil 6to. Piso. Av. Ladrón de Guevara E11-253: Instituto Geofísico Escuela Politécnica Nacional.
- (2022b). *Wolf Volcano Special Report No. 2 - 2022. Special 02.* Campus "Ing. José Rubén Orellana", Facultad de Ingeniería Civil 6to. Piso. Av. Ladrón de Guevara E11-253: Instituto Geofísico Escuela Politécnica Nacional.
- (2022c). *Wolf Volcano Special Report No. 3 - 2022. Special 03.* Campus "Ing. José Rubén Orellana", Facultad de Ingeniería Civil 6to. Piso. Av. Ladrón de Guevara E11-253: Instituto Geofísico Escuela Politécnica Nacional.
- (2024). *Special Volcanic Report - Fernandina - 2024 - No. 1. Special 01.* Campus "Ing. José Rubén Orellana", Facultad de Ingeniería Civil 6to. Piso. Av. Ladrón de Guevara E11-253: Instituto Geofísico Escuela Politécnica Nacional.
- Jónsson, S. (2009). "Stress interaction between magma accumulation and trapdoor faulting on Sierra Negra volcano, Galápagos". *Tectonophysics* 471(1-2), pages 36–44. DOI: [10.1016/j.tecto.2008.08.005](https://doi.org/10.1016/j.tecto.2008.08.005).
- Jónsson, S., H. Zebker, and F. Amelung (2005). "On trapdoor faulting at Sierra Negra volcano, Galápagos". *Journal of Volcanology and Geothermal Research* 144(1-4), pages 59–71. DOI: [10.1016/j.jvolgeores.2004.11.029](https://doi.org/10.1016/j.jvolgeores.2004.11.029).
- Jónsson, S., H. Zebker, P. Cervelli, P. Segall, H. Garbeil, P. Mougini-Mark, and S. Rowland (1999). "A shallow-dipping dike fed the 1995 flank eruption at Fernandina Volcano, Galápagos, observed by satellite radar interferometry". *Geophysical Research Letters* 26(8), pages 1077–1080. DOI: [10.1029/1999GL900108](https://doi.org/10.1029/1999GL900108).
- Kilbride, B. M., M. Edmonds, and J. Biggs (2016). "Observing eruptions of gas-rich compressible magmas from space". *Nature Communications* 7(1), page 13744. DOI: [10.1038/ncomms13744](https://doi.org/10.1038/ncomms13744).
- Kurz, M. D., S. K. Rowland, J. Curtice, A. E. Saal, and T. Naumann (2014). "Eruption Rates for Fernandina Volcano: A New Chronology at the Galápagos Hotspot Center", page 14.
- Lazecský, M., K. Spaans, P. J. González, Y. Maghsoudi, Y. Morishita, F. Albino, J. Elliott, N. Greenall, E. Hatton, A. Hooper, D. Juncu, A. McDougall, R. J. Walters, C. S. Watson, J. R. Weiss, and T. J. Wright (2020). "LiCSAR: An Automatic InSAR Tool for Measuring and Monitoring Tectonic and Volcanic Activity". *Remote Sensing* 12(15), page 2430. DOI: [10.3390/rs12152430](https://doi.org/10.3390/rs12152430).
- Li, K. L., C. J. Bean, A. F. Bell, M. Ruiz, S. Hernandez, and J. Grannell (2022). "Seismic tremor reveals slow fracture propagation prior to the 2018 eruption at Sierra Negra volcano, Galápagos". *Earth and Planetary Science Letters* 586, page 117533. DOI: [10.1016/j.epsl.2022.117533](https://doi.org/10.1016/j.epsl.2022.117533).
- Li, S., F. Sigmundsson, V. Drouin, M. M. Parks, B. G. Ófeigsson, K. Jónsdóttir, R. Grapenthin, H. Geirsson, A. Hooper, and S. Hreinsdóttir (2021). "Ground Deformation After a Caldera Collapse: Contributions of Magma Inflow and Viscoelastic Response to the 2015–2018 Deformation Field Around Bárðarbunga, Iceland". *Journal of Geophysical Research: Solid Earth* 126(3). DOI: [10.1029/2020JB020157](https://doi.org/10.1029/2020JB020157).
- Liu, Y.-K., J. Ruch, H. Vasyura-Bathke, and S. Jónsson (2019). "Influence of ring faulting in localizing surface deformation at subsiding calderas". *Earth and Planetary Science Letters* 526, page 115784. DOI: [10.1016/j.epsl.2019.115784](https://doi.org/10.1016/j.epsl.2019.115784).
- Manconi, A., T. R. Walter, and F. Amelung (2007). "Effects of mechanical layering on volcano deformation". *Geophysical Journal International* 170(2), pages 952–958. DOI: [10.1111/j.1365-246X.2007.03449.x](https://doi.org/10.1111/j.1365-246X.2007.03449.x).
- Manconi, A. and F. Casu (2012). "Joint analysis of displacement time series retrieved from SAR phase and amplitude: Impact on the estimation of volcanic source parameters". *Geophysical Research Letters* 39(14), n/a–n/a. DOI: [10.1029/2012GL052202](https://doi.org/10.1029/2012GL052202).
- Mayhew, L. E., D. J. Geist, S. E. Childers, and J. D. Pierson (2007). "Microbial Community Comparisons as a Function of the Physical and Geochemical Conditions of Galápagos Island Fumaroles". *Geomicrobiology Journal* 24(7-8), pages 615–625. DOI: [10.1080/01490450701672133](https://doi.org/10.1080/01490450701672133).
- McBirney, A., A. Cullen, D. Geist, E. Vicenzi, R. Duncan, M. Hall, and M. Estrella (1985). "The Galapagos volcano Alcedo: A unique ocean caldera". *Journal of Volcanology and Geothermal Research* 26(1-2), pages 173–177. DOI: [10.1016/0377-0273\(85\)90052-6](https://doi.org/10.1016/0377-0273(85)90052-6).
- Morishita, Y., M. Lazecsky, T. Wright, J. Weiss, J. Elliott, and A. Hooper (2020). "LiCSBAS: An Open-Source InSAR Time Series Analysis Package Integrated with the LiCSAR Automated Sentinel-1 InSAR Processor". *Remote Sensing* 12(3), page 424. DOI: [10.3390/rs12030424](https://doi.org/10.3390/rs12030424).
- Mougini-Mark, P. J., H. Snell, and R. Ellisor (2000). "GOES satellite and field observations of the 1998 eruption of Volcan Cerro Azul, Galápagos Islands". *Bulletin of Volcanology* 62(3), pages 188–198. DOI: [10.1007/s004450000078](https://doi.org/10.1007/s004450000078).
- Naumann, T. and D. Geist (2000). "Physical volcanology and structural development of Cerro Azul Volcano, Isabela Island, Galapagos: implications for the development of Galapagos-type shield volcanoes". *Bulletin of Volcanology* 61, pages 497–514.
- Naumann, T., D. J. Geist, and M. Kurz (2002). "Petrology and Geochemistry of Volcan Cerro Azul: Petrologic Diversity among the Western Galapagos Volcanoes". *Journal of Petrology* 43(5), pages 859–883. DOI: [10.1093/petrology/43.5.859](https://doi.org/10.1093/petrology/43.5.859).
- Naumann, T. R. and L. K. Krebs (2003). "Petrology and Geochemistry of Volcan Darwin, Isabela Island, Galapagos Archipelago". 2003. Conference Name: AGU Fall Meet-

- ing Abstracts ADS Bibcode: 2003AGUFM.V12D0618N, pages V12D–0618.
- Nusbaum, R. L., M. W. Colgan, D. E. Lawton, and M. D. Glascock (1991). “Mineralogic constraints on the magmatic history of Volcán Darwin flank lava at Urvina Bay, Islá Isabela, Galápagos”. *Journal of volcanology and geothermal research* 47, pages 359–366.
- Pepe, S., R. Castaldo, V. De Novellis, L. D’Auria, C. De Luca, F. Casu, E. Sansosti, and P. Tizzani (2017). “New insights on the 2012–2013 uplift episode at Fernandina Volcano (Galápagos)”. *Geophysical Journal International* 211(2), pages 673–685. DOI: [10.1093/gji/ggx330](https://doi.org/10.1093/gji/ggx330).
- Reddin, E., S. K. Ebmeier, E. Rivalta, M. Bagnardi, S. Baker, A. F. Bell, P. Mothes, and S. Aguaiza (2023). “Magmatic connectivity among six Galápagos volcanoes revealed by satellite geodesy”. *Nature Communications* 14(1), page 6614. DOI: [10.1038/s41467-023-42157-x](https://doi.org/10.1038/s41467-023-42157-x).
- Reynolds, R. W., D. Geist, and M. D. Kurz (1995). “Physical volcanology and structural development of Sierra Negra volcano, Isabela Island, Galápagos archipelago”. *Geological Society of America Bulletin* 107(12), pages 1398–1410. DOI: [10.1130/0016-7606\(1995\)107<1398:PVASDO>2.3.CO;2](https://doi.org/10.1130/0016-7606(1995)107<1398:PVASDO>2.3.CO;2).
- Rouland, S. K. and D. C. Munro (1992). “The caldera of Volcan Fernandina: a remote sensing study of its structure and recent activity”. *Bulletin of Volcanology* 55(1-2), pages 97–109. DOI: [10.1007/BF00301123](https://doi.org/10.1007/BF00301123).
- Rouland, S. K., A. J. L. Harris, M. J. Wooster, F. Amelung, H. Garbeil, L. Wilson, and P. J. Mouginis-Mark (2003). “Volumetric characteristics of lava flows from interferometric radar and multispectral satellite data: the 1995 Fernandina and 1998 Cerro Azul eruptions in the western Galápagos”. *Bulletin of Volcanology* 65(5), pages 311–330. DOI: [10.1007/s00445-002-0262-x](https://doi.org/10.1007/s00445-002-0262-x).
- Ruiz, M. Z., F. Civilini, C. J. Ebinger, S. J. Oliva, M. C. Ruiz, G. Badi, P. C. La Femina, and J. A. Casas (2022). “Precursory Signal Detected for the 2018 Sierra Negra Volcanic Eruption, Galápagos, Using Seismic Ambient Noise”. *Journal of Geophysical Research: Solid Earth* 127(3). DOI: [10.1029/2021JB022990](https://doi.org/10.1029/2021JB022990).
- Sandanbata, O., H. Kanamori, L. Rivera, Z. Zhan, S. Watada, and K. Satake (2021). “Moment Tensors of Ring-Faulting at Active Volcanoes: Insights Into Vertical-CLVD Earthquakes at the Sierra Negra Caldera, Galápagos Islands”. *Journal of Geophysical Research: Solid Earth* 126(6). DOI: [10.1029/2021JB021693](https://doi.org/10.1029/2021JB021693).
- Shreve, T. and F. Delgado (2023). “Trapdoor Fault Activation: A Step Toward Caldera Collapse at Sierra Negra, Galápagos, Ecuador”. *Journal of Geophysical Research: Solid Earth* 128(5), e2023JB026437. DOI: [10.1029/2023JB026437](https://doi.org/10.1029/2023JB026437).
- Siebert, L., T. Simkin, and P. Kimberly (2010). *Volcanoes of the world*. 3rd ed. OCLC: ocn647772311. Washington, D.C. : Berkeley ; University of California Press: Smithsonian Institution. ISBN: 978-0-520-26877-7.
- Simkin, T. and K. A. Howard (1970). “Caldera Collapse in the Galápagos Islands, 1968: The largest known collapse since 1912 followed a flank eruption and explosive volcanism within the caldera.” *Science* 169(3944), pages 429–437. DOI: [10.1126/science.169.3944.429](https://doi.org/10.1126/science.169.3944.429).
- Stock, M. J., M. Bagnardi, D. A. Neave, J. MacLennan, B. Bernard, I. Buisman, M. L. M. Gleeson, and D. Geist (2018). “Integrated Petrological and Geophysical Constraints on Magma System Architecture in the Western Galápagos Archipelago: Insights From Wolf Volcano”. *Geochemistry, Geophysics, Geosystems* 19(12), pages 4722–4743. DOI: [10.1029/2018GC007936](https://doi.org/10.1029/2018GC007936).
- Stock, M. J., D. Geist, D. A. Neave, M. L. M. Gleeson, B. Bernard, K. A. Howard, I. Buisman, and J. MacLennan (2020). “Cryptic evolved melts beneath monotonous basaltic shield volcanoes in the Galápagos Archipelago”. *Nature Communications* 11(1), page 3767. DOI: [10.1038/s41467-020-17590-x](https://doi.org/10.1038/s41467-020-17590-x).
- Teasdale, R., D. Geist, M. Kurz, and K. Harpp (2005). “1998 Eruption at Volcan Cerro Azul, Galapagos Islands: I. Syn-Eruptive Petrogenesis”. *Bulletin of Volcanology* 67(2), pages 170–185. DOI: [10.1007/s00445-004-0371-9](https://doi.org/10.1007/s00445-004-0371-9).
- Tepp, G., C. J. Ebinger, M. Ruiz, and M. Belachew (2014). “Imaging rapidly deforming ocean island volcanoes in the western Galápagos archipelago, Ecuador”. *Journal of Geophysical Research: Solid Earth* 119(1), pages 442–463. DOI: [10.1002/2013JB010227](https://doi.org/10.1002/2013JB010227).
- U.S. Geological Survey Earthquake Catalogue (2023).
- Vasconez, F., P. Ramón, S. Hernandez, S. Hidalgo, B. Bernard, M. Ruiz, A. Alvarado, P. La Femina, and G. Ruiz (2018). “The different characteristics of the recent eruptions of Fernandina and Sierra Negra volcanoes (Galápagos, Ecuador)”. *Volcanica* 1(2), pages 127–133. DOI: [10.30909/vol.01.02.127133](https://doi.org/10.30909/vol.01.02.127133).
- Venzke, E. (2023). *Global Volcanism Program, 2023. Volcanoes of the World (v. 5.1.1)*. [Database]. Smithsonian Institution. DOI: [10.5479/si.gvp.votw5-2023.5.1](https://doi.org/10.5479/si.gvp.votw5-2023.5.1).
- Xu, W., S. Jónsson, J. Ruch, and Y. Aoki (2016). “The 2015 Wolf volcano (Galápagos) eruption studied using Sentinel-1 and ALOS-2 data: The 2015 Wolf Eruption in the Galápagos”. *Geophysical Research Letters* 43(18), pages 9573–9580. DOI: [10.1002/2016GL069820](https://doi.org/10.1002/2016GL069820).
- Xu, W., L. Xie, R. Bürgmann, X. Liu, and J. Wang (2023). “The 2022 Eruption of Wolf Volcano, Galápagos: The Role of Caldera Ring-Faults During Magma Transfer From InSAR Deformation Data”. *Geophysical Research Letters* 50(14), e2023GL103704. DOI: [10.1029/2023GL103704](https://doi.org/10.1029/2023GL103704).
- Yu, C., Z. Li, N. T. Penna, and P. Crippa (2018). “Generic Atmospheric Correction Model for Interferometric Synthetic Aperture Radar Observations”. *Journal of Geophysical Research: Solid Earth* 123(10), pages 9202–9222. DOI: [10.1029/2017JB015305](https://doi.org/10.1029/2017JB015305).
- Yun, S., P. Segall, and H. Zebker (2006). “Constraints on magma chamber geometry at Sierra Negra Volcano, Galápagos Islands, based on InSAR observations”. *Journal of Volcanology and Geothermal Research* 150(1-3), pages 232–243. DOI: [10.1016/j.jvolgeores.2005.07.009](https://doi.org/10.1016/j.jvolgeores.2005.07.009).

APPENDIX A

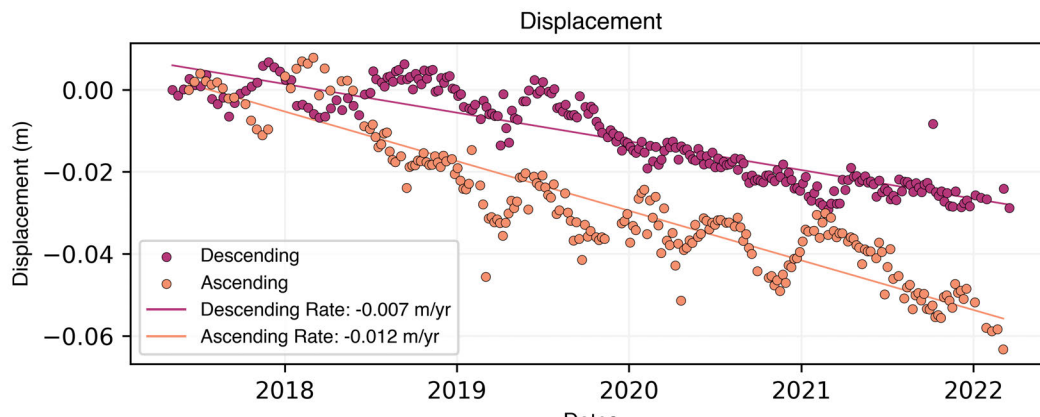


Figure A1: Time series of post-intrusion subsidence on the eastern flank of Cerro Azul following the 2017 uplift. The time series are for a point at -0.913°N , -91.374°E , relative to a reference area between -90.967°E , -90.964°E , and -0.957°N to -0.950°N .

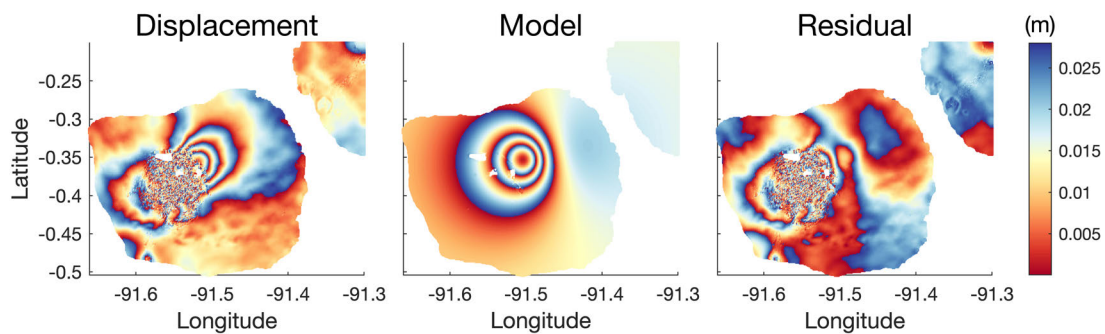


Figure A2: Data, modelling, and residual for geodetic source modelling of the residual post-eruption of Fernandina, in the ascending track direction. The input data are the residual presented in Figure A4D, spanning 27/01/2020–01/06/2020.

Table A1: Details of previous source models of displacement at Alcedo volcano. Complex deformation patterns generally requires either extreme or multiple sources. Lines separate periods when there are multiple sources. Where S is a spherical source, CDM is a Compound Dislocation Model, and RD is a Rectangular Dislocation. Horizontal lines distinguish events.

Reference	Depth (km)	Geometry	Duration	ΔV (m^3)	Location	Instrument
Hooper et al. [2007]	2.2	Pipe	1997–2001	-1.3×10^6	Caldera	ERS-1/2
Bagnardi [2014]	3.0	S + Fault	2007–2009	Radius: 0.2 km	Caldera	ALOS-1
Galletto et al. [2019]	2.1	CDM	2007–2010	8.7×10^6	S. Caldera	Envisat, ALOS-1
	1	Fault	2007–2010	-		Envisat, ALOS-1
	2.1	RD	2007–2010	7×10^6		Envisat, ALOS-1
	1	Fault	2007–2010	-		Envisat, ALOS-1
Galletto et al. [2019]	2.3	CDM	01/10–06/10	-3.9×10^6	S. Caldera	Envisat, ALOS-1
	2.1	CDM	01/10–06/10	2.8×10^6	W. Caldera	Envisat, ALOS-1
	2.7	RD	01/10–06/10	-2.3×10^6	S. Caldera	Envisat, ALOS-1
	3.1	RD	01/10–06/10	2.3×10^6	W. Caldera	Envisat, ALOS-1
Galletto et al. [2019]	3.4	RD	07/10–03/11	4.1×10^6	S. Caldera	Envisat, ALOS-1

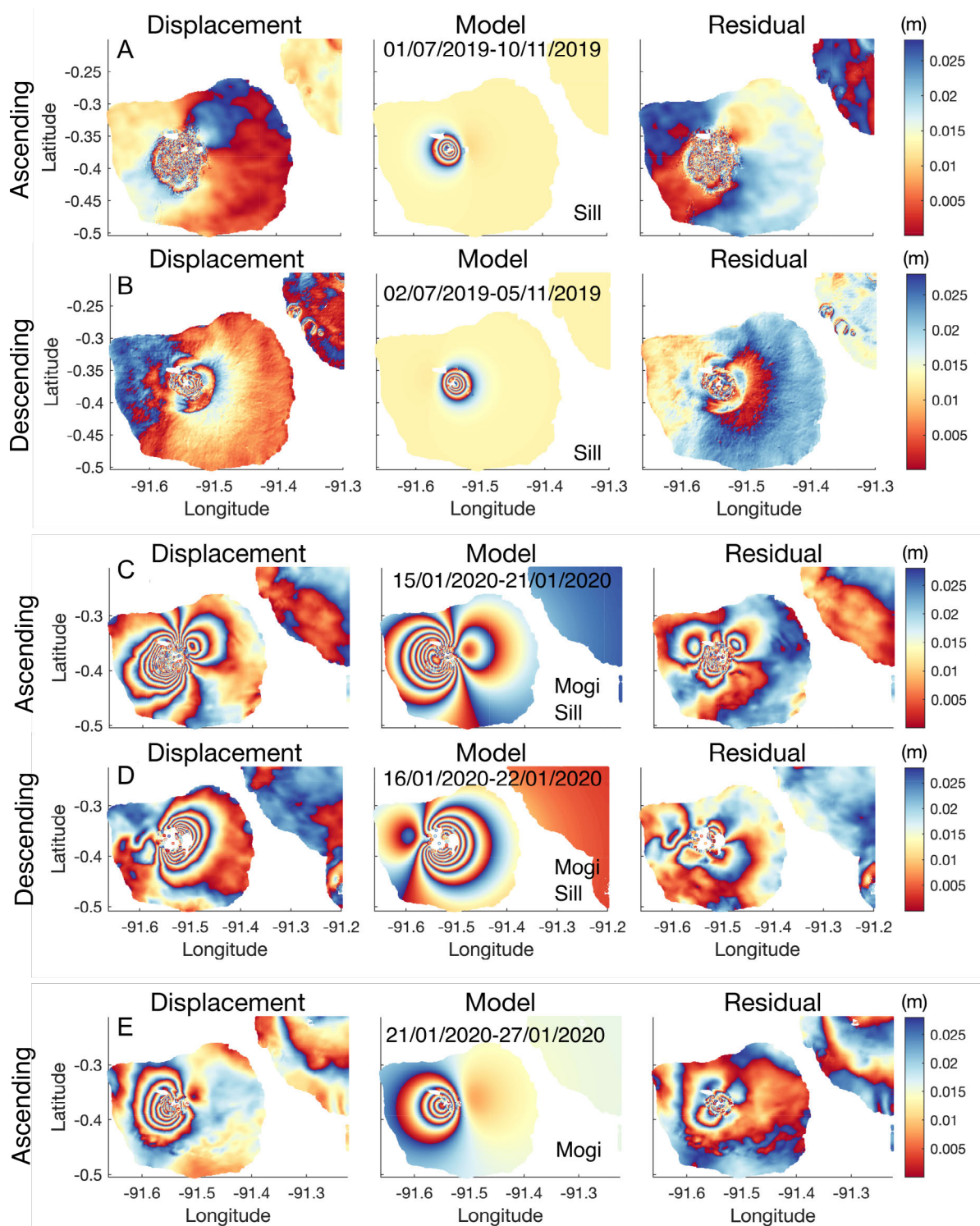


Figure A3: Results of geodetic source modelling for the 2020 eruption of Fernandina. Full results in Tables A11– A17. [A] Data, model, and residual for cumulative displacement at Fernandina from 1/07/2019–10/11/2019, in the ascending track direction. [B] Data, model, and residual for cumulative displacement at Fernandina from 2/07/2019–05/11/2019, in the descending track direction. [C] Data, model, and residual for cumulative displacement at Fernandina from 15/01/2020–21/01/2020, in the ascending track direction. [D] Data, model, and residual for cumulative displacement at Fernandina from 16/01/2020–22/01/2020, in the descending track direction. [E] Data, model, and residual for cumulative displacement at Fernandina from 21/01/2020–27/01/2020, in the ascending track direction.

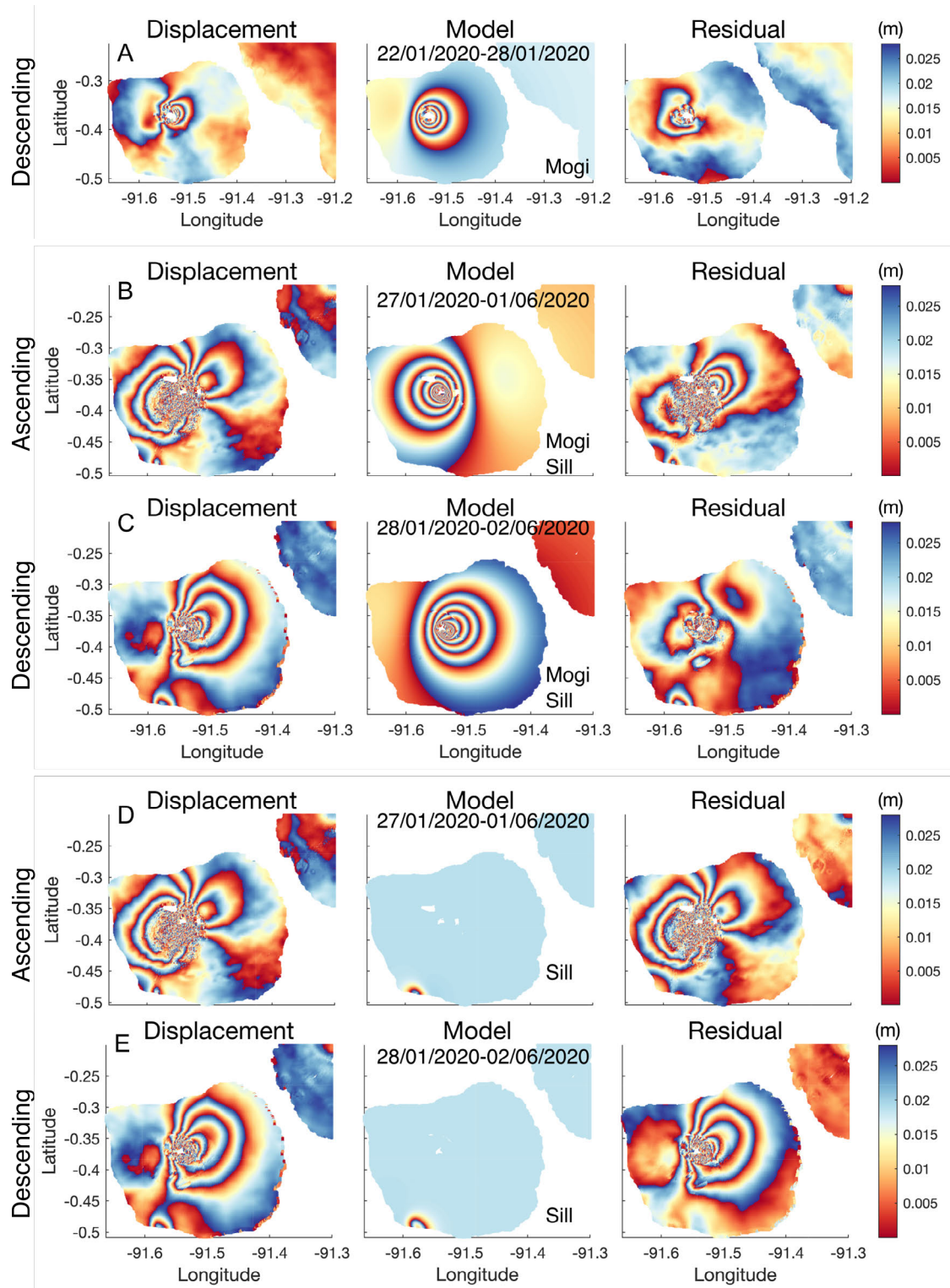


Figure A4: Results of geodetic source modelling for the 2020 eruption of Fernandina. Full results in Tables A11– A17. [A] Data, model, and residual for cumulative displacement at Fernandina from 22/07/2020–28/01/2020, in the descending track direction. [B] Data, model, and residual for cumulative displacement at Fernandina from 27/01/2020–01/06/2020, in the ascending track direction. [C] Data, model, and residual for cumulative displacement at Fernandina from 28/01/2020–02/06/2020, in the descending track direction. [D] Data, model, and residual for cumulative displacement at Fernandina from 27/01/2020–01/06/2020, in the ascending track direction. [E] Data, model, and residual for cumulative displacement at Fernandina from 28/01/2020–02/06/2020, in the descending track direction.

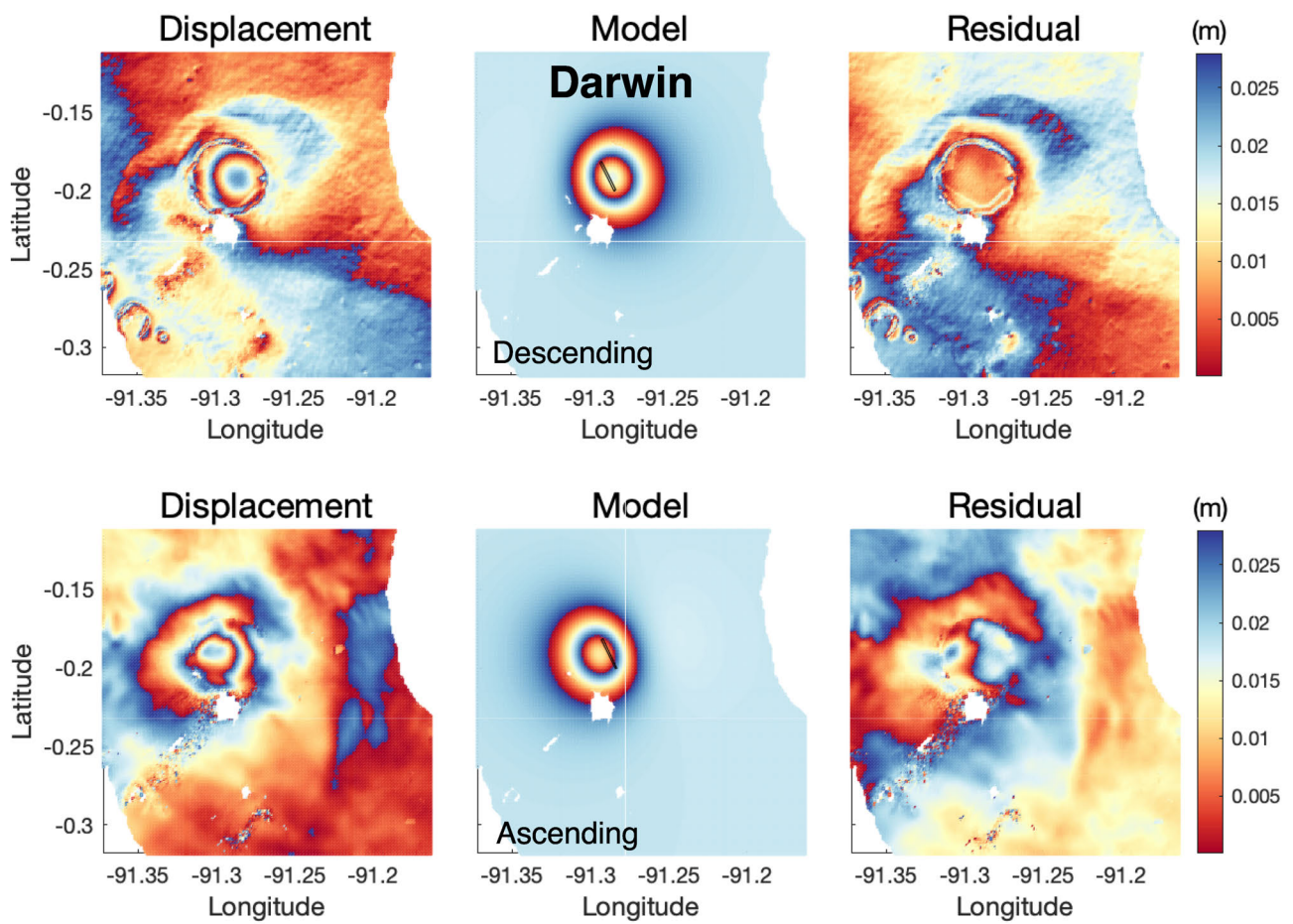


Figure A5: Results of geodetic source modelling for uplift at Darwin, using a sill geometry. The optimal source results are in [Table A9](#).

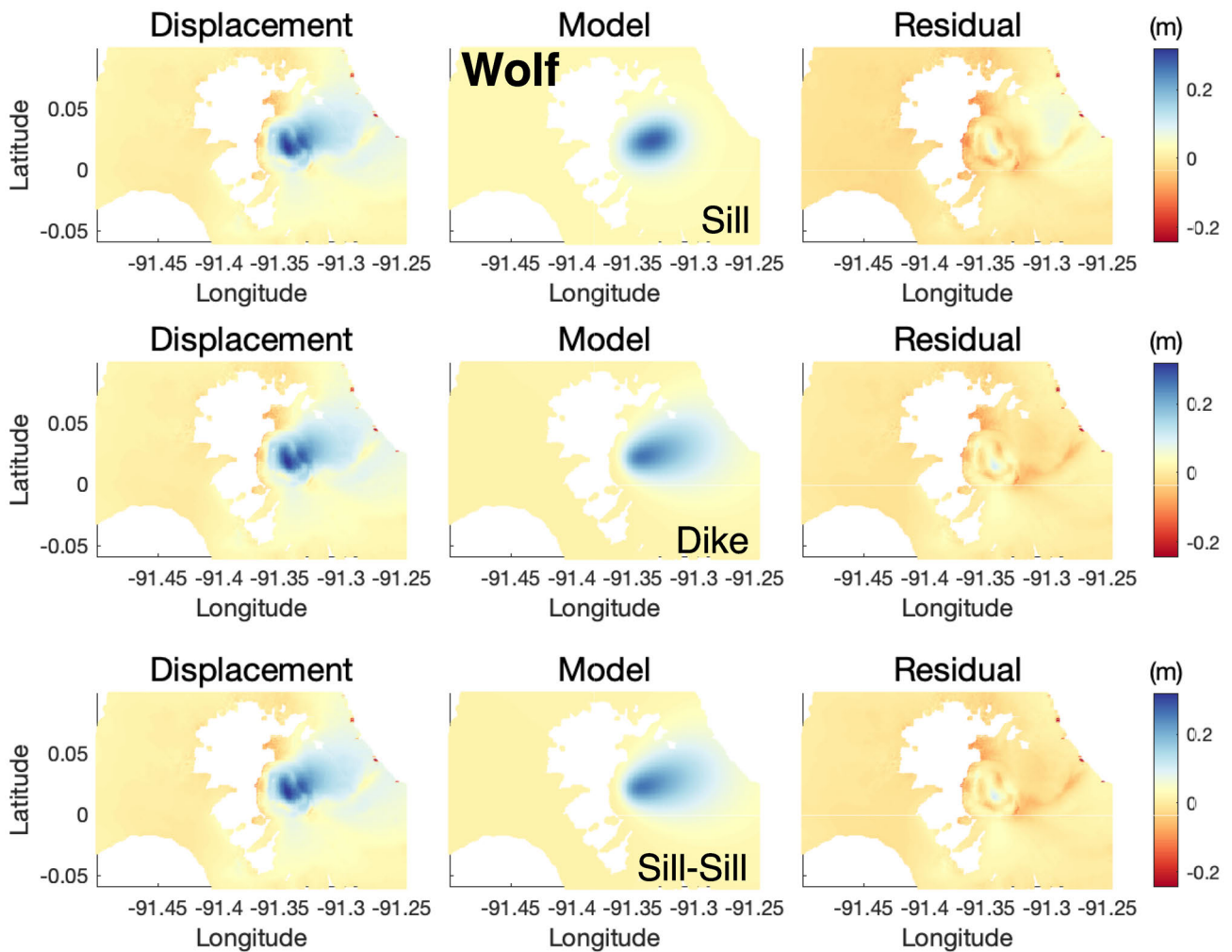


Figure A6: Unwrapped data, model, and residual for cumulative inflation at Wolf from 2015 to 2022, in the Descending track direction, as presented in [Figure 7](#).

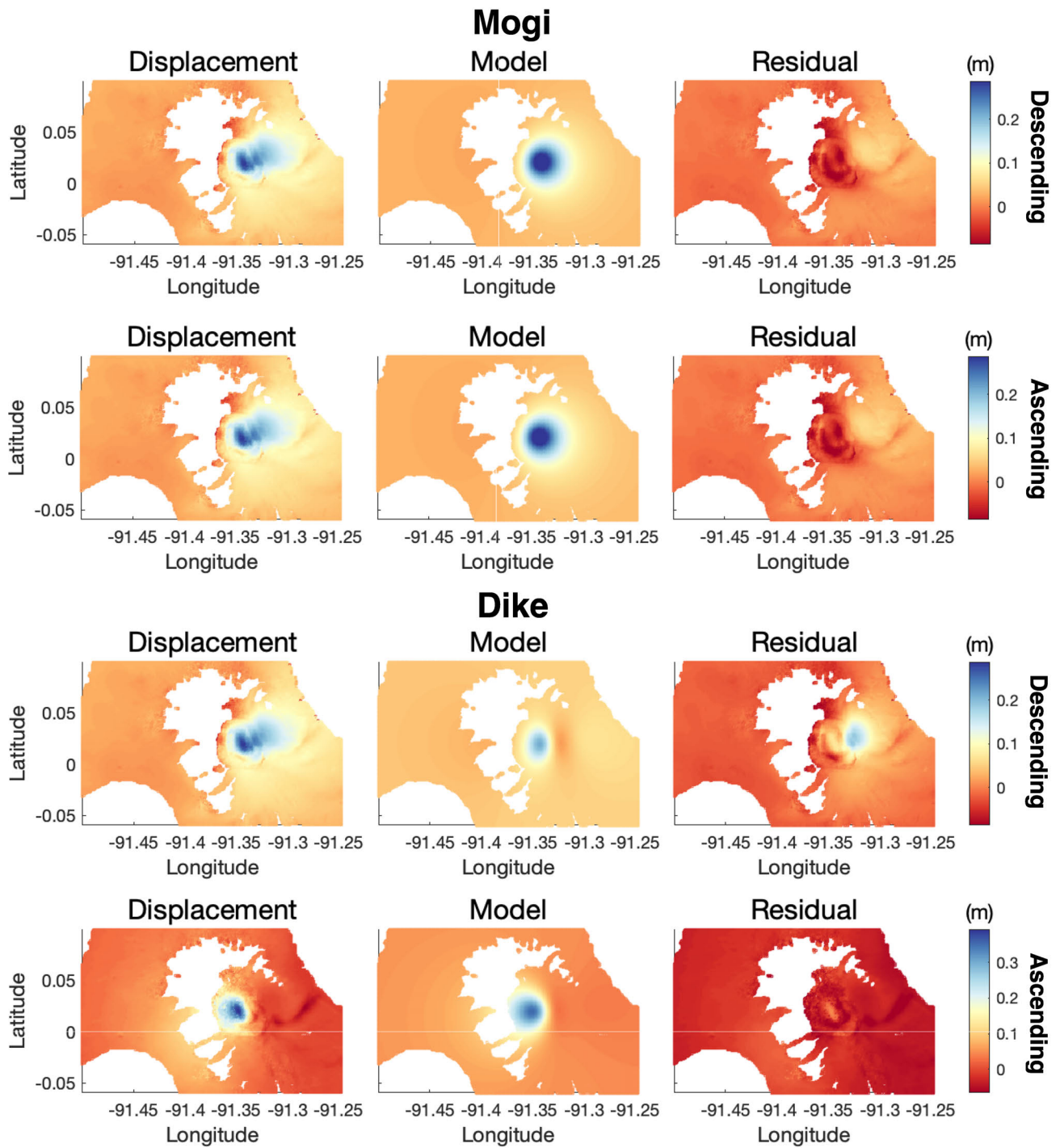


Figure A7: Unwrapped data, model, and residual for cumulative inflation at Wolf from 2017 to 2022, performed as a joint inversion, for Mogi and dike sources.

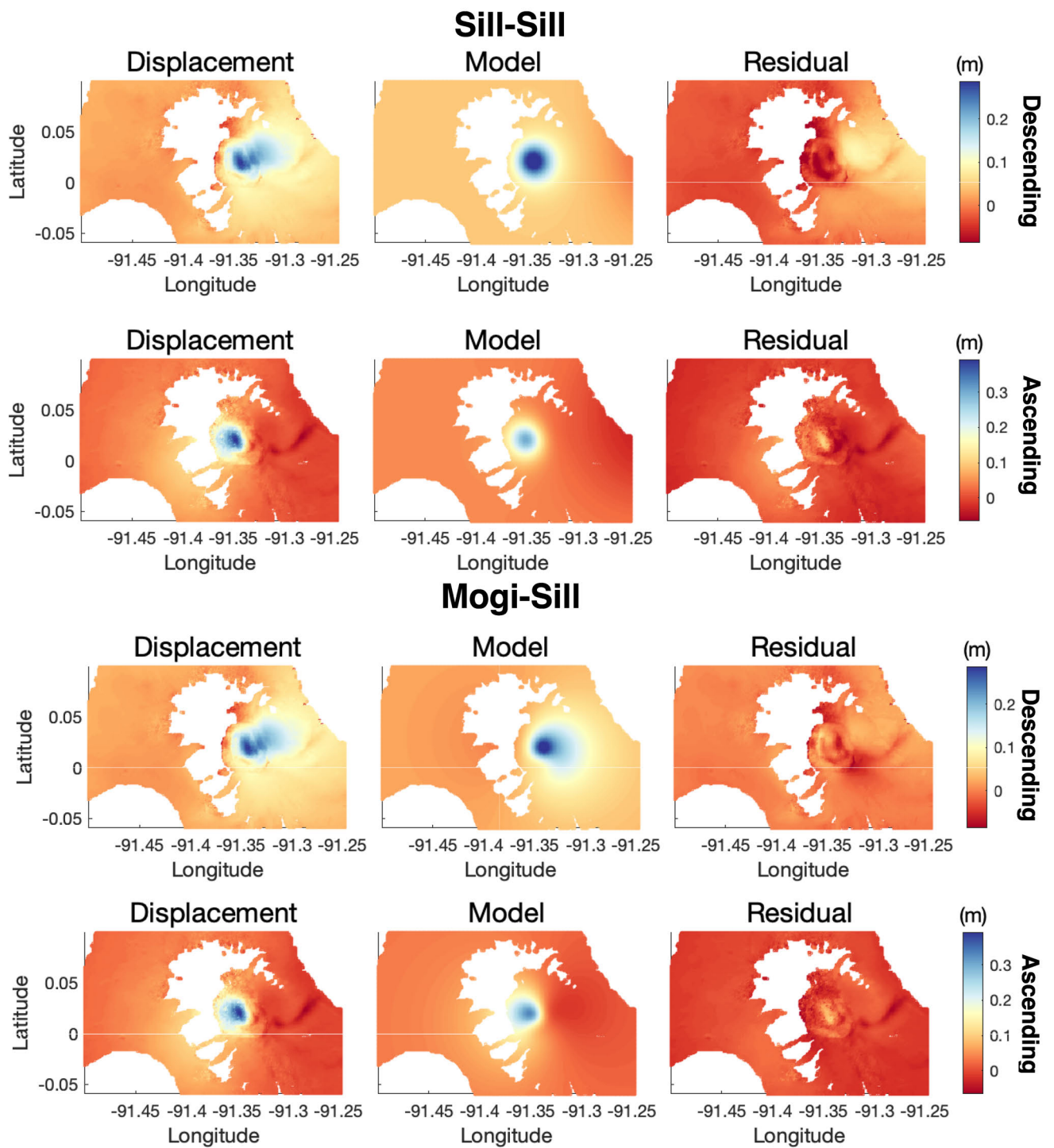


Figure A8: Unwrapped data, model, and residual for cumulative inflation at Wolf from 2017 to 2022, performed as a joint inversion, for sill-sill and Mogi-sill sources. The optimal results are presented in [Table A22](#).

Fernandina 2020: Pre-Eruptive Mogi

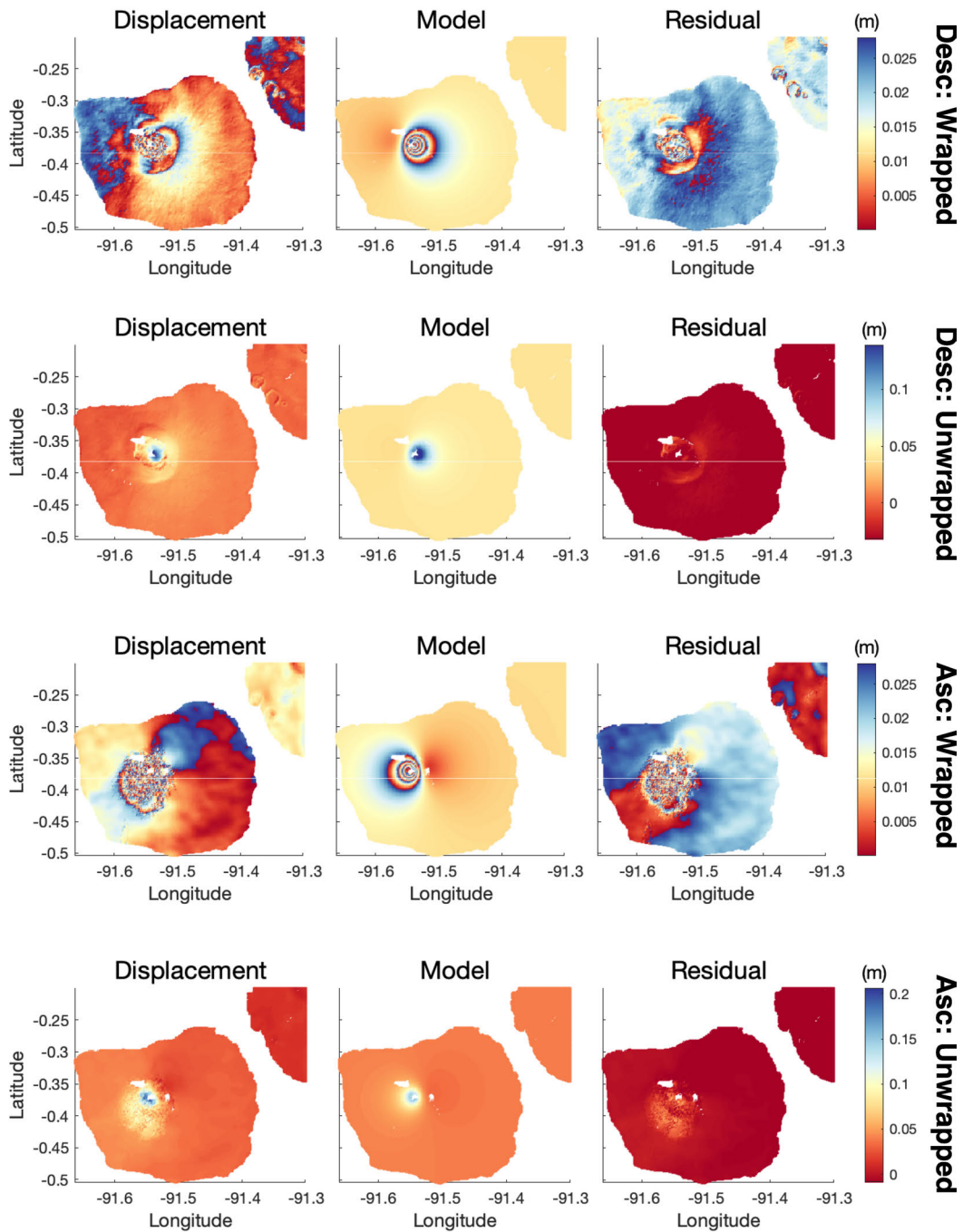


Figure A9: Unwrapped and wrapped, data, model, and residual for pre-eruptive inflation at Fernandina from 01/07/2019–10/11/2019 for a Mogi source, in both Descending and Ascending track directions. The optimal results are presented in [Table A12](#).

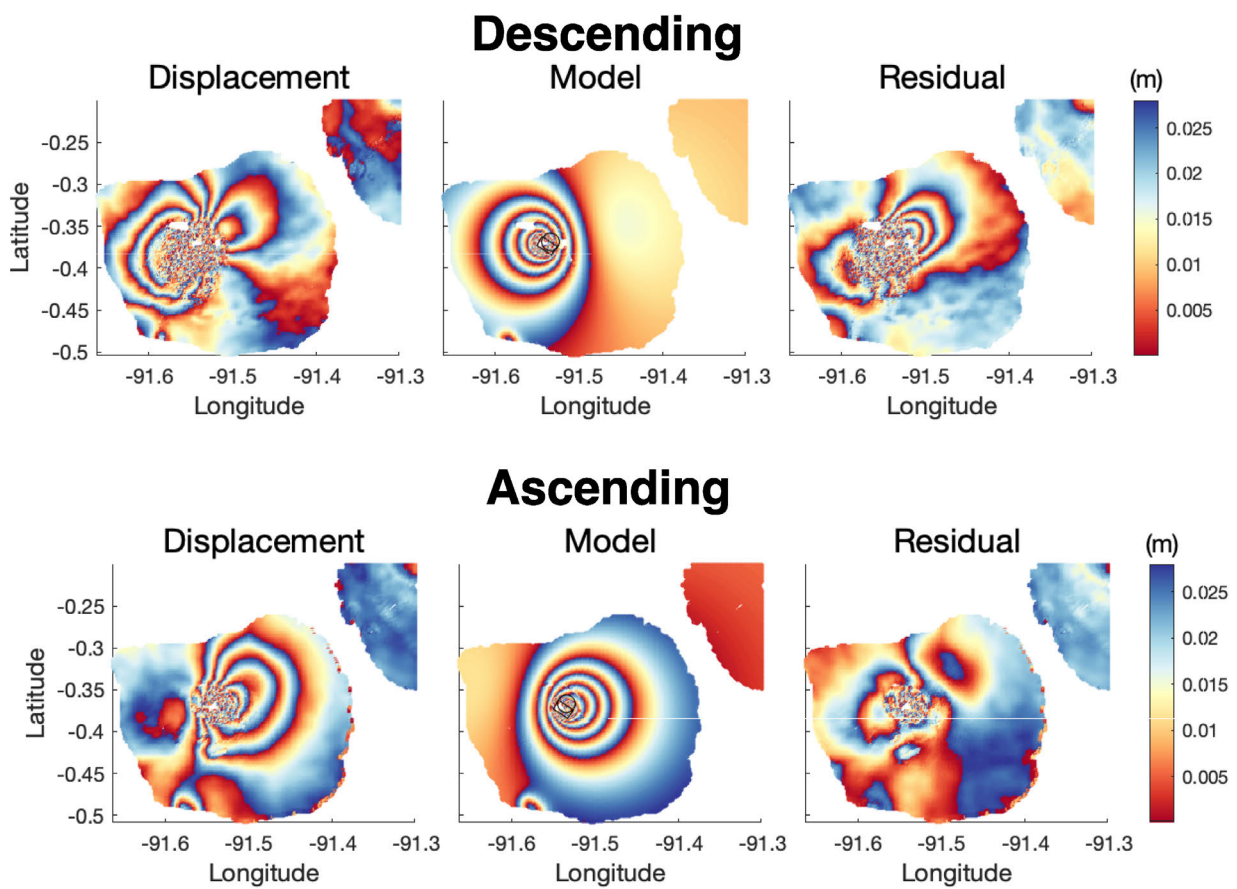


Figure A10: Combined wrapped post-eruptive deformation at Fernandina using both the sub-volcanic Mogi and Sill sources, and the offshore sill, for Period V.

Table A2: Details of previous source models of displacement at Cerro Azul volcano. Multiple sources are inferred during almost all of the unrest periods. Lines separate periods when there are multiple sources. Data from Guo et al. [2019] all span the co-unrest period, and are inverted from individual interferograms.

Reference	Depth (km)	Geometry	Duration	ΔV (m ³)	Location	Instrument
Amelung et al. [2000]	5	Mogi	1992–1997	N/A	Caldera	ERS-1/2
Baker [2012]	6.1	Mogi	1998	N/A	Caldera	ERS, Radarsat-1
Bagnardi [2014]	6.08	Mogi	1998	Radius: 0.2	Caldera	
Baker [2012]	6.2	Mogi	2008	N/A	Caldera	Envisat, ALOS-1
	3.2	Dislocation		4.6×10^7	SE. Flank	
	5.7	Mogi		N/A	Caldera	
	2.1	Dislocation		7.2×10^7	SE. Flank	
	6.4	Mogi		N/A	Caldera	
	1.3	Dislocation		3.1×10^7	SE. Flank	
Galletto et al. [2020]	4.9	Mogi	10/07–04/08	11×10^6	Caldera	ALOS-1
	3.3	RD Dike	04/08–09/08	N/A	SE. Flank	ALOS-1 ^a
	3.5	RD Dike	04/08–09/08	69.2×10^6	SE. Flank	ALOS-1 ^a
	5.2	RD Sill	04/08–09/08	-27.2×10^6	Caldera	ALOS-1 ^a
	5.2	RD Sill	04/08–09/08	-10.4×10^6	Caldera	ALOS-1 ^a
	3.3	RD Dike	04/08–05/08	9.9×10^6	SE. Flank	Envisat
	5.2	RD Sill	04/08–05/08	-11.5×10^6	Caldera	Envisat
	3	RD Dike	05/08–07/08	56.7×10^6	SE. Flank	Envisat
	5.2	RD Sill	05/08–07/08	-25.4×10^6	Caldera	Envisat
	3.3	RD Dike	04/08–09/08	N/A	SE. Flank	ALOS-1 ^b
	3.5	RD Dike	04/08–09/08	68.1×10^6	SE. Flank	ALOS-1 ^b
	5.2	RD Sill	04/08–09/08	-31.1×10^6	Caldera	ALOS-1 ^b
	3.8	RD Dike	04/08–09/08	23.9×10^6	SE. Flank	ALOS-1 ^b
Guo et al. [2019]	3.2	Mogi	07/03–19/03	-3.34×10^6	Caldera	Sentinel-1
	4.8	Sill	07/03–19/03	6.4×10^6	SE. Flank	
	5.95	Mogi	08/03–20/03	-3.58×10^7	Caldera	
	5.77	Sill	08/03–20/03	3.14×10^7	SE. Flank	
	5.97	Mogi	19/03–31/03	-4.37×10^7	Caldera	
	5.4	Sill	19/03–31/03	5.7×10^7	SE. Flank	
	4.45	Mogi	20/03–01/04	-1.92×10^7	Caldera	
	6.62	Sill	20/03–01/04	3.85×10^7	SE. Flank	
Bagnardi [2017]	6	Mogi	2017	N/A	Caldera	Sentinel-1
	5	Sill	2017	$2 - 4 \times 10^7$	SE. Flank	

^a Model 1: 2 dikes 2 sills

^b Model 2: 3 dikes 1 sill

Table A3: Details of previous source models of displacement at Darwin volcano. There are a handful of models here as Darwin has been the subject of only three studies where model geometries were retrieved.

Reference	Depth (km)	Geometry	Duration	ΔV (m ³)	Location	Instrument
Amelung et al. [2000]	3	Mogi	1992–1998	N/A	Caldera	ERS-1/2
Amelung et al. [2000] ^a	2.7			5.8×10^6		
Manconi et al. [2007]	3.25 ^b	Mogi	1992–1998	4.93×10^6	Caldera	ERS-1/2
	4.25 ^c			7.74×10^6		
Bagnardi [2014]	3.1	Mogi	1992–2000	10×10^6	Caldera	ERS-1/2

^a in Manconi et al. [2007].

^b Upper Bounds

^c Lower Bounds

Table A4: Table of known deformation sources at Fernandina. Includes shallow, deeper, and radial sources for both eruptive and non-eruptive periods.

Reference	Depth (km)	Geometry	Duration	ΔV (m ³)	Location	Instrument
Amelung et al. [2000]	3	Mogi	1998–1999	N/A	Caldera	ERS-1/2
Jónsson et al. [1999]	0	Mogi	1995	7.5×10^6	SW. Flank	ERS-1/2
Bagnardi and Amelung [2012]	1.1	RD	01/07–07/07	1.1×10^6	Caldera	Envisat
	4.9	Spheroid	09/07–04/08	N/A	Caldera	
	4.5	Sill	08/07–09/07	19×10^6	SE. Flank	
Chadwick et al. [2011]	0.93	Sill	01/03–04/05	0.75×10^6	Caldera ^a	GPS/Envisat
	6.07	Mogi	01/03–04/05	5.07×10^6	Caldera ^a	
	1.18	Sill	08/05–11/06	1.36×10^6	Caldera ^a	
	3.92	Mogi	08/05–11/06	2.93×10^6	Caldera ^a	
	1.55	Mogi	01/03–04/05	1.6×10^6	Caldera ^b	
	10.5	Mogi	01/03–04/05	4.84×10^6	Caldera ^b	
	1.52	Mogi	08/05–11/06	2.5×10^6	Caldera ^b	
	10.1	Mogi	08/05–11/06	1.1×10^6	Caldera ^b	
	0	Dike	04/05–09/05	8.9×10^6	Flank ^c	
	1.06	Sill	04/05–09/05	-0.61×10^6	Caldera ^c	
	5	Mogi	04/05–09/05	-3.02×10^6	Caldera ^c	
	0	Dike	04/05–09/05	1.7×10^6	Flank ^d	
	0.67	Dike	04/05–09/05	6.45×10^6	Flank ^d	
	1.06	Sill	04/05–09/05	0.92×10^6	Caldera ^d	
	5	Mogi	04/05–09/05	-6.2×10^6	Caldera ^d	
	0	Dike	04/05–09/05	2.58×10^6	Flank ^e	
	0.79	Dike	04/05–09/05	5.3×10^6	Flank ^e	
0	Dike	04/05–09/05	1.89×10^6	Flank ^e		
1.06	Sill	04/05–09/05	0.83×10^6	Caldera ^e		
5	Mogi	04/05–09/05	-6.4×10^6	Caldera ^e		
Pepe et al. [2017]	2.1	Pipe	2012–2013	6.5×10^7	Caldera	COSMO-SkyMed
Bagnardi et al. [2013]	0.8	Sill	2009	7.29×10^6	Caldera	ERS-1/2, Envisat, JERS-1
	4.93	Penny	2009	N/A	Caldera	
	1.08	Sill	2009	-4.8×10^6	SW. Flank	
	0.65	Dike	2009	6.92×10^6	SW. Flank	
	0	Dike	2009	2.81×10^6	SW. Flank	
	0.64	Sill	1995	3.47×10^6	Caldera	
0	Dike	1995	6.09×10^6	SW. Flank		

^a Model 1; ^c Model 3^b Model 2; ^d Model 4

Table A5: Table of deformation source models at Sierra Negra. Deformation here is commonly modelled by volume change in a reservoir at approximately 2 km depth, with some contribution from faults.

Reference	Depth (km)	Geometry	Duration	ΔV (m ³)	Location	Instrument
Amelung et al. [2000]	2.2	Sill	1992–1997	N/A	Caldera	ERS-1/2
	1.9	Sill	1998–1999			
	2.3–2.9	Sill	1997–1998			
	0	Fault	1997–1998			
Jónsson et al. [2005]	2	Sill	1992–1999	$2-6 \times 10^8$	Caldera	ERS-1/2
Chadwick et al. [2006]	2.2	Sill	02/04–02/05	1.7×10^8 yr ⁻¹	Caldera	Envisat, cGPS
	0	Fault	04/2005	N/A		
Geist et al. [2006a]	2.3	Mogi	2000–2002	2.6×10^8	Caldera	GPS, Gravimeter
	2.1	Sill	2000–2002	4.1×10^8		
Yun et al. [2006]	1.9	Sill	1998–1999	6.7×10^8	Caldera	ERS
Jónsson [2009]	2.2	Sill	02/04–01/05	N/A	Caldera	Envisat, cGPS
	0	Fault	04/2005			
Bagnardi [2014]	2.27	Sill	1992–2010	N/A	Caldera	-
Gaddes et al. [2019]	2	Sill	12/14–07/18		Caldera	Sentinel-1

Table A6: Table of deformation sources at Wolf, both underneath the caldera and at the caldera rim. Deformation at Wolf can be modelled by stacked reservoirs, though may also be explained by the combination of a single deeper source, and ring faulting.

Reference	Depth (km)	Geometry	Duration	ΔV (m ³)	Location	Instrument
Amelung et al. [2000]	2	Mogi	1992–1997	N/A	Caldera	ERS-1/2
Bagnardi [2014]	1.43	RD	1992–2010	5×10^6	Caldera	
Xu et al. [2016]	5.2	Sill	05/2015	-1.54×10^7	Caldera	Sentinel-1, ALOS-2
	5	Sill	06/2015	-1.5×10^7	Caldera	
	5	Sill	05/15–07/15	-2.15×10^7	Caldera	
	1.3	Sill	05/2015	-1.7×10^6	Caldera	
	1.2	Sill	06/2015	-0.9×10^6	Caldera	
	1.3	Sill	05/15–07/15	-2.8×10^6	Caldera	
	0	Dike	05/2015	0.5×10^6	Rim	
	0	Dike	05/15–06/15	0×10^6 ^a	Rim	
	0	Dike	06/2015	N/A	Rim	
	0	Dike	05/15–07/15	1×10^6	Rim	
	N/A	Dike	05/2015	N/A	Caldera	
	N/A	Dike	05/15–06/15	N/A	Caldera	
	0	Dike	06/2015	0.3×10^6	Caldera	
	0	Dike	05/15–07/15	0.4×10^6	Caldera	
De Novellis et al. [2017]	1.5	Sill	2004–2010	1×10^6	Caldera	Sentinel-1
	1.4	Spheroid	2004–2010	N/A	Caldera	
	1.5	Sill	05/2015	-1.8×10^6	Caldera	
	0.1	Dike	05/2015	6×10^6	Rim	
	1.5	Sill	06/15–07/15	-1.75×10^6	Caldera	
Xu et al. [2023]	5	Sill	2022 Eruption	-1.9×10^7	Caldera	Multi- Platforms
	1			-1.6×10^6		
Liu et al. [2019]	4	Sill	-	2.6×10^6	Caldera	-

^a $< 1 \times 10^{-5}$ m³

Table A7: Alcedo best-fit parameters (from 06/01/2017–30/09/2021).

Model parameter	Optimal	Mean	Median	2.5 %	97.5 %
Sill length (m)	3328.7	3097.69	3232.96	1466.51	3770.22
Sill width (m)	4794.14	4658.87	4676.6	4010.34	5185.77
Sill depth (m)	1934.25	2219.55	2152.05	1665.99	3137.51
Sill strike (°)	207.155	209.051	208.784	198.998	220.828
Sill x (m from local. ref)	−13 220.4	−13 172.2	−13 186.2	−13 455.3	−12 808.8
Sill y (m from local. ref)	−4321.31	−4272.33	−4278.05	−4648.59	−3864.57
Sill opening (m)	−0.125	−0.173	−0.141	−0.423	−0.105
InSAR const. (m)	0.018	0.0184	0.018	0.0137	0.0231
InSAR const. (m)	−0.031	−0.030	−0.030	−0.0342	−0.027

Table A8: Cerro Azul best-fit parameters (from 05/07/2017–04/10/2022).

Model parameter	Optimal	Mean	Median	2.5 %	97.5 %
Sill length (m)	9540.71	9536.53	9536.79	9348.25	9720.94
Sill width (m)	124.815	254.65	264.204	129.529	335.946
Sill depth (m)	6308.62	6303.04	6302.51	6228.65	6379.66
Sill strike (°)	229.38	229.416	229.422	228.392	230.42
Sill x (m from local. ref)	−4510.74	−4549	−4550.18	−4603.09	−4490.1
Sill y (m from local. ref)	−18 012.9	−17 970.8	−17 969.4	−18 034.2	−17 915.7
Sill opening (m)	24.0124	12.481	11.2677	8.939 92	22.9933
InSAR const. (m)	1.44	0.0001	0.0001	−0.001	0.001
InSAR const. (m)	−0.0175	−0.0173	−0.017	−0.0184	−0.016

Table A9: Darwin best-fit sill parameters (from 23/10/2019–15/06/2021).

Model parameter	Optimal	Mean	Median	2.5 %	97.5 %
Sill length (m)	143.676	350.223	313.766	126.645	742.109
Sill width (m)	2273.56	2213.53	2231.92	1676.91	2680.65
Sill depth (m)	3342.57	3350.31	3348.04	3218.95	3490.9
Sill strike (°)	243.848	243.709	243.875	232.734	254.468
Sill x (m from local. ref)	3027.43	3034.46	3035.42	2821.63	3248.02
Sill y (m from local. ref)	12 796.5	12 761.1	12 766	12 494.9	13 013.4
Sill opening (m)	4.913 55	2.522 84	2.378 83	0.931 934	5.621 99
InSAR const. (m)	0.018	0.0181	0.018	0.017	0.019
InSAR const. (m)	−0.002	−0.002	−0.002	−0.003	−0.002

Table A10: Darwin best-fit Mogi parameters (from 23/10/2019–15/06/2021).

Model parameter	Optimal	Mean	Median	2.5 %	97.5 %
Mogi x (m from local. ref)	3359.36	3358.17	3358.28	3314.38	3401.09
Mogi y (m from local. ref)	11 868.7	11 865.9	11 865.7	11 816.5	11 916.4
Mogi depth (m)	2564.91	2565.58	2564.51	2484.15	2653.88
Mogi ΔV ($\times 10^6$ m ³)	1.7867	1.784 99	1.7838	1.688 25	1.891 22
InSAR const. (m)	0.016 833 2	0.016 85	0.016 847 6	0.015 810 8	0.017 889 8
InSAR const. (m)	−0.004 191 9	−0.004 181 27	−0.004 176 78	−0.004 733 57	−0.003 655 9

Table A11: Fernandina pre-eruptive (Descending: 02/07/2019–05/11/2019, Ascending: 01/07/2019–10/11/2019) best-fit parameters.

Model parameter	Optimal	Mean	Median	2.5 %	97.5 %
Sill length (m)	1626.04	1624.03	1625.69	1444.53	1765.66
Sill width (m)	57.1699	100.965	73.4386	50.0182	244.593
Sill depth (m)	2177.02	2173.44	2173.03	2124.87	2223.74
Sill strike (°)	132.06	132.588	132.59	128.215	136.987
Sill x (m from local. ref)	-15 029	-15 040.7	-15 034.8	-15 091.9	-15 010.2
Sill y (m from local. ref)	9083.18	9067.53	9073.74	9012.79	9100.41
Sill opening (m)	17.8241	12.9637	14.1185	4.223 41	19.8783
InSAR const. (m)	0.041 087 4	0.041 077 1	0.041 074	0.039 935 9	0.042 229
InSAR const. (m)	0.008 771	0.008 785 79	0.008 785 95	0.008 346 1	0.009 231 5

Table A12: Fernandina best-fit Mogi parameters (from 01/07/2019–10/11/2021)

Model parameter	Optimal	Mean	Median	2.5 %	97.5 %
Mogi x (m from local. ref)	-15 037.8	-15 039.2	-15 039.2	-15 057.7	-15 020.9
Mogi y (m from local. ref)	9135.29	9137.07	9137.17	9118.26	9155.4
Mogi depth (m)	1659.63	1662.5	1662.45	1633.1	1691.39
Mogi ΔV ($\times 10^6$ m ³)	1.778 89	1.783 51	1.783 59	1.731 32	1.8358
InSAR const. (m)	0.039 331 6	0.039 353 9	0.039 354	0.038 212 2	0.040 494 4
InSAR const. (m)	0.006 664 61	0.006 624 32	0.006 623 71	0.006 169 23	0.007 083 95

Table A13: Fernandina pre-eruptive (Ascending: 10/11/2019–09/01/2020) best-fit parameters (^a Depth lower limit at 5 km).

Model parameter	Optimal	Mean	Median	2.5 %	97.5 %
Sill length (m)	5537.1	5556.08	5556.42	5074.43	6044.65
Sill width (m)	10 322.2	8693.67	8908.24	5932.7	10 348.2
Sill depth ^a (m)	2590.3	2720.04	2702.21	2338.54	3201.37
Sill strike (°)	95.1886	96.105	95.8427	88.0753	107.206
Sill x (m from local. ref)	-22 060.5	-22 020	-21 964.4	-23 244.7	-21 254.4
Sill y (m from local. ref)	-9951.75	-8326.94	-8523.62	-9918.98	-5672.84
Sill opening (m)	0.100 164	0.105 278	0.104 305	0.091 130 6	0.124 777
InSAR const. (m)	-0.013 646 3	-0.014 250 7	-0.014 185 2	-0.017 502 9	-0.011 315 3

Table A14: Fernandina post-eruptive (Descending: 16/01/2020–22/01/2020, Ascending: 15/01/2020–21/01/2020) best-fit parameters.

Model parameter	Optimal	Mean	Median	2.5 %	97.5 %
Mogi x (m from local. ref)	-15 127.2	-15 163.6	-15 166.1	-15 193.3	-15 116.5
Mogi y (m from local. ref)	9021.05	8964.86	8960.82	8888.83	9046.04
Mogi depth (m)	2262.41	2257.11	2257.62	2229.99	2282.04
Mogi ΔV ($\times 10^7$ m ³)	2.885 47	2.812 53	2.8104	2.713 05	2.914 48
Sill length (m)	1650.08	1819.46	1806.72	1662.05	2021.46
Sill width (m)	1347.74	1623.39	1611.38	1352.9	1900.27
Sill depth (m)	2575.88	2501.54	2499.66	2415.54	2581.48
Sill strike (°)	84.4448	77.1589	76.4371	69.6594	90.5214
Sill x (m from local. ref)	-15 074	-14 993.5	-14 987.7	-15 140.1	-14 896
Sill y (m from local. ref)	8431.95	8263.41	8268.12	8087.62	8437.12
Sill opening (m)	-8.594 83	-6.291 33	-6.291 89	-8.514 26	-4.474 29
InSAR const. (m)	-0.054 791 7	-0.054 991	-0.054 990 7	-0.056 820 5	-0.053 174 9
InSAR const. (m)	-0.012 926 3	-0.012 895 3	-0.012 895 2	-0.014 183 5	-0.011 593 1

Table A15: Fernandina post-eruptive (Descending: 22/01/2020–28/01/2020, Ascending: 21/01/2020–27/01/2020) best-fit parameters.

Model parameter	Optimal	Mean	Median	2.5 %	97.5 %
Mogi x (m from local. ref)	-14 972	-14 973.3	-14 973	-15 006.4	-14 939.5
Mogi y (m from local. ref)	8847.18	8842.16	8842.33	8801.1	8882.16
Mogi depth (m)	3154.19	3162.11	3162.18	3096.74	3230.07
Mogi ΔV ($\times 10^6$ m ³)	6.520 52	6.552 85	6.550 28	6.266 49	6.856 57
InSAR const. (m)	0.016 479 6	0.016 377 5	0.016 378 8	0.015 289	0.017 461 5
InSAR const. (m)	-0.052 836 2	-0.052 883 7	-0.052 888 3	-0.054 139 9	-0.051 624

Table A16: Fernandina post-eruptive (Descending: 28/01/2020–02/06/2020, Ascending: 27/01/2020–01/06/2020) best-fit parameters.

Model parameter	Optimal	Mean	Median	2.5 %	97.5 %
Mogi x (m from local. ref)	-14 306.2	-14 276.6	-14 298.6	-14 340.4	-14 095.9
Mogi y (m from local. ref)	9444.53	9481.28	9462.11	9411.1	9659.21
Mogi depth (m)	5438.96	5641.75	5463.43	5268.77	6953.38
Mogi ΔV ($\times 10^7$ m ³)	-1.8065	-1.903 75	-1.815 64	-2.553 17	-1.7229
Sill length (m)	1392.68	1268.42	1376.84	415.581	1426.38
Sill width (m)	2364.29	2318.97	2358.77	2006.99	2393.16
Sill depth (m)	742.623	815.227	752.192	705.918	1269.05
Sill strike (°)	213.054	213.913	213.38	211.708	219.16
Sill x (m from local. ref)	-15 797.4	-15 758.3	-15 788.7	-15 815.4	-15 526.3
Sill y (m from local. ref)	9450.06	9442.33	9445.59	9390.97	9472.76
Sill opening (m)	-0.338 323	-0.487 198	-0.342 755	-1.780 24	-0.321 735
InSAR const. (m)	0.035 377 1	0.036 070 9	0.035 418 9	0.034 436	0.041 026 4
InSAR const. (m)	0.009 052 92	0.009 860 17	0.009 174 4	0.008 222 18	0.015 095 3

Table A17: Fernandina post-eruptive (Descending: 28/01/2020–02/06/2020, Ascending: 27/01/2020–01/06/2020) best-fit parameters for SW coast.

Model parameter	Optimal	Mean	Median	2.5 %	97.5 %
Sill length (m)	3480.18	3677.59	3654.58	3157.48	4287.55
Sill width (m)	1309.01	900.469	946.658	86.0892	1624.66
Sill depth (m)	1472.73	1573.15	1574.79	1359.85	1784.3
Sill strike (°)	316.608	318.525	318.44	310.984	326.592
Sill x (m from local. ref)	-18 465.4	-18 563.5	-18 552.7	-18 883.7	-18 308.8
Sill y (m from local. ref)	-4022.42	-4262.93	-4251.47	-4741.99	-3834.26
Sill opening (m)	-0.091 177 6	-0.257 217	-0.131 543	-1.495 84	-0.072 127 5
InSAR const. (m)	0.018 578	0.018 548 5	0.018 554 8	0.017 602 5	0.019 487 7
InSAR const. (m)	0.001 016 15	0.000 947 441	0.000 946 579	0.000 334 314	0.001 550 5

Table A18: Fernandina post-eruptive (Descending: 28/01/2020–02/06/2020, Ascending: 27/01/2020–01/06/2020) best-fit parameters for residual ascending data.

Model parameter	Optimal	Mean	Median	2.5 %	97.5 %
Mogi x (m from local. ref)	-9698.96	-9694.63	-9695.07	-9839.84	-9547.25
Mogi y (m from local. ref)	11 206.2	11 203.4	11 202.5	11 103.6	11 305.8
Mogi depth (m)	4393.45	4399.39	4399.33	4244.31	4555.39
Mogi ΔV ($\times 10^6$ m ³)	-9.36	-9.38	-9.38	-9.96	-8.82
InSAR const. (m)	0.014 182	0.014 191 7	0.014 193 1	0.013 328 2	0.015 066 6

Table A19: Wolf sill (14/11/2015–24/12/2021) best-fit parameters.

Model parameter	Optimal	Mean	Median	2.5 %	97.5 %
Sill length (m)	170.457	240.661	225.946	160.353	389.486
Sill width (m)	4171.77	4163.99	4164.42	4096.86	4230.22
Sill depth (m)	2608.71	2602.87	2602.9	2578.05	2627.14
Sill strike (°)	164.115	164.111	164.112	163.286	164.951
Sill x (m from local. ref)	14 995.2	14 997.8	14 997.8	14 971.9	15 024
Sill y (m from local. ref)	-8518.5	-8516.62	-8516.56	-8544.58	-8488.18
Sill opening (m)	8.790 95	6.592 41	6.619 58	3.845 14	9.345 61
InSAR const. (m)	0.027 344 9	0.027 378 4	0.027 378 5	0.026 893 1	0.027 858

Table A20: Wolf dike (14/11/2015–24/12/2021) best-fit parameters.

Model parameter	Optimal	Mean	Median	2.5 %	97.5 %
Dike length (m)	1454.27	1441.36	1444.97	1312.79	1544.54
Dike width (m)	7748.71	7735.3	7735.44	7553.47	7913.9
Dike depth (m)	1482.75	1483.07	1482.59	1456.92	1510.75
Dike dip (°)	-34.3384	-34.3373	-34.3424	-35.0192	-33.6374
Dike strike (°)	162.236	162.141	162.138	161.481	162.831
Dike x (m from local. ref)	14 764.2	14 768.8	14 769	14 741.8	14 794.3
Dike y (m from local. ref)	-8556.14	-8558.99	-8559.24	-8585.96	-8532.27
Dike opening (m)	0.947 789	0.957 385	0.952 969	0.883 719	1.061 98
InSAR const. (m)	0.015 799 8	0.015 947 4	0.015 945 7	0.015 384 4	0.016 541 4

Table A21: Wolf sill–sill (14/11/2015–24/12/2021) best-fit parameters.

Model parameter	Optimal	Mean	Median	2.5 %	97.5 %
Sill length (m)	3508.4	3498.9	3498.83	3449.24	3546.94
Sill width (m)	2189.81	2193.31	2192.21	2144.36	2246.23
Sill depth (m)	1545.32	1544.16	1544.27	1509.51	1579.67
Sill strike (°)	284.425	284.812	284.825	283.149	286.36
Sill x (m from local. ref)	16 630.6	16 631.8	16 631.5	16 608.4	16 655.4
Sill y (m from local. ref)	−7091.35	−7093.66	−7094.34	−7129.28	−7055.5
Sill opening (m)	0.428 466	0.428 237	0.428 08	0.412 842	0.444 602
Sill length (m)	250.568	477.078	446.19	203.871	1133.9
Sill width (m)	4432.56	4448.66	4449.94	3923.8	4941.9
Sill depth (m)	5295.31	5272.95	5271.06	5093.87	5468.74
Sill strike (°)	158.272	158.079	157.98	153.782	162.795
Sill x (m from local. ref)	17 889.1	17 878.1	17 874.5	17 618.8	18 153.5
Sill y (m from local. ref)	−7303.52	−7314.57	−7317.48	−7501.93	−7119.37
Sill opening (m)	8.3342	5.539 13	4.565 39	1.784 35	9.797 95
InSAR const. (m)	0.014 657 1	0.014 607 2	0.014 611 4	0.013 831 9	0.015 335 3

Table A22: best-fit parameters for inversions presented in Figures A7 and A8.

Source	Depth	x (m)	y (m)	ΔV (m ³)	Opening (m)	Length (m)	Width (m)	Strike (°)	Dip (°)
Mogi	2235.7	16 097.9	−8236.32	7.2×10^6	-	-	-	-	-
Dike	3244.5	16 977.7	−8299.41	-	9.99	776.2	1213.07	175	60
Sill	7831.1	24 999.8	−5679.75	-	−0.156	14 990.9	14 993.9	176.7	-
Sill	2727.4	16 568.5	−8638.34	-	9.99	421.7	1274.9	36.8	-
Mogi	2047.3	16 461.1	−8651.24	1.7×10^7	-	-	-	-	-
Sill	2569.6	16 421.1	−8824.42	-	−14.8934	1818.4	378.6	206.6	-

Table A23: Lava volume estimates for recent Galápagos eruptions. Volumes that could not be found in literature are estimated using the areas presented in Figure 2, and previous measurements of lava thickness. ¹Rowland et al. [2003] estimate average thicknesses of 4.5 m for the 1998 eruption of Cerro Azul, ²average thickness for the 2017 and 2005 circumferential eruptions at Fernandina was 2 m [Vasconez et al. 2018].

Volcano	Year	Fissure Type	Volume (m ³)	Volume reference	Area reference
Wolf ^a	2015	Circumferential	8.7×10^6	Bernard et al. [2019]	Xu et al. [2016]
Wolf ^b	2022	Radial	2.3×10^7	S. Aguaiza (pers. comm.)	IGEPN [2022c]
Fernandina ^c	1995	Radial	5.5×10^7	Vasconez et al. [2018]	Rowland et al. [2003]
Fernandina ^d	2005	Circumferential	1.8×10^7	Vasconez et al. [2018]	Bagnardi et al. [2013]
Fernandina ^e	2009	Radial	5.7×10^7	Vasconez et al. [2018]	Bagnardi et al. [2013]
Fernandina ^f	2017	Circumferential	$13 \pm 6.5 \times 10^6$	Vasconez et al. [2018]	IGEPN [2020]
Fernandina ^g	2018	Radial	$7.92 \pm 4 \times 10^6$	Vasconez et al. [2018]	IGEPN [2020]
Fernandina ^h	2020	Circumferential	6×10^6	Estimated here ²	IGEPN [2020]
Cerro Azul ⁱ	1998	Radial	5.4×10^7	Rowland et al. [2003]	Rowland et al. [2003]
Cerro Azul ^j	2008	Radial	4.7×10^7	Estimated here ¹	Galetto et al. [2020]
Sierra Negra ^k	2005	Rim	1.5×10^8	Vasconez et al. [2018]	Geist et al. [2008]
Sierra Negra ^l	2018	Rim and Distal	$1.9 \pm 0.94 \times 10^8$	Vasconez et al. [2018]	Vasconez et al. [2018]